NONINVASIVE ARFI ULTRASOUND FOR DIFFERENTIATING CAROTID PLAQUE WITH HIGH STROKE RISK

Gabriela Torres Garate

A dissertation submitted to the faculty at the University of North Carolina at Chapel Hill in partial fulfillment of the requirements for the degree of Doctor of Philosophy in the Department of Biomedical Engineering in the School of Medicine.

Chapel Hill
2021

Approved by:

Caterina M. Gallippi

Gianmarco Pinton

Xiaoning Jiang

Mark A. Farber

Jonathon W. Homeister

ABSTRACT

Gabriela Torres Garate: Noninvasive ARFI Ultrasound for Differentiating Carotid Plaque with High Stroke Risk
(Under the direction of Caterina M. Gallippi)

Stroke is the leading cause of death worldwide. Fortunately, incidence and mortality rates are declining due to the successes of pharmaceutical therapies and revascularization procedures such as carotid endarterectomy (CEA). While CEA has high efficacy for preventing stroke in patients with severe (>70%) carotid stenosis, its usefulness decreases as stroke risk declines in patients without symptoms and less severe stenosis. Clinical studies show that 13 out of 14 symptomatic patients with 50-69% stenosis, and 21 out of 22 asymptomatic patients with severe stenosis undergo CEA unnecessarily [1, 2]. There is an unmet need to identify vulnerable carotid plaque and indicate stroke risk.

Improving the assessment of carotid plaque vulnerability could be met by analyzing plaque structure and composition. Post-mortem studies have shown that the presence of thin or ruptured fibrous caps (TRFC), lipid-rich necrotic cores (LRNC), and intraplaque hemorrhage (IPH) is associated with high stroke risk [3]. Further, MRI studies have shown association between the presence of TRFC and IPH with previous stroke or transient ischemic attack (TIA), with increased risk of stroke conferred by TRFC, LRNC, and IPH, in human carotid plaques. While features that convey vulnerability to rupture are well known, there is currently no established low-cost, noninvasive imaging method that consistently characterizes plaque structure and composition.

The project proposed herein aims to develop and evaluate Acoustic Radiation Force Impulse (ARFI)-based ultrasound techniques for delineating the structure and composition of carotid plaque in humans. First, novel ARFI imaging methods are evaluated in terms of sensitivity and specificity for detecting of calcium, collagen, lipid-rich necrotic core, and intraplaque hemorrhage in human atherosclerotic plaques *in vivo*. Second, an automatic classification framework is developed and compared to a human reader-based ARFI image assessment. Third, the automatic classifier perfor-

mance is improved by including additional data acquisitions in the cardiac cycle, and using high frequency and harmonic tracking. Overall, this project demonstrates the efficacy of ARFI ultrasound, evaluating log(VoA) and with a machine learning-based automatic classifier, to delineate vulnerable plaque components in human carotid plaques *in vivo*. These findings have the potential to improve the current state of the art in clinical diagnosis and management of atherosclerosis.

To my parents, Alberto and Francy.

ACKNOWLEDGEMENTS

First, I would like to thank my advisor, Dr. Caterina Gallippi. You have been a role model for me since joining the lab, and I am thankful for your advice, guidance and motivation throughout my graduate education. You helped me build confidence about my research, and about myself, and for that, I will always be grateful. To my dissertation committee, Drs. Gianmarco Pinton, Xiaoning Jiang, Jonathon Homeister, and Mark Farber, I would like to thank each of you for your support, time and feedback.

There are a number of people who assisted in this project, and were instrumental for its success. First, I would like to thank Dr. Melissa Caughey, who served as the research sonographer and biostatistician. You made every early morning call fun and rewarding. Second, I would like to thank Melrose Fisher, clinical nurse coordinator, who made this research possible by recruiting and enrolling patients. Thank you to the surgeons, residents, and staff of UNC Vascular Surgery, whose expertise in extracting carotid specimens made this study, not just possible, but successful. Thank you Carolyn Suitt of the UNC Center for Gastrointestinal Biology and Disease (CGIBD) Histology Core, and Ashley Ezzell, Kara Clissold, and Curtis Connor of the UNC Research Histology Core, for spending countless hours embedding, sometimes re-embedding, sectioning and staining carotid specimens. Your assistance was key to this research, and allowed having reliable histological gold standard images. Thank you to Jon Frank and his team at the UNC Biomedical Research Imaging Center for extracted specimen imaging. Thank you Drs. Benjamin Huang, Carlos Zamora, Alex Hung, and Ellie Lee of UNC Radiology, and Elizabeth Merricks of UNC Blood Research Center for your patience and help annotating tricky ultrasound images with promptness and detail.

I would also like to thank past and present Gallippi lab members, Chris, Murad, Keerthi, Keita, Joey, Anna, for making my days in lab enriching and enjoyable. Thank you for the daily laughs, discussions, weekly lab journal club, and the occasionally late-night lab dinners. All of you helped me not feel alone and supported during the pandemic, and I will forever be grateful. Special thanks to Keerthi Anand, for collecting early morning patient data for this project while I was doing my

internship in Issaquah. Special thanks to Dr. Tomek Czernuszewicz, whose work in the lab showed the potential of applying ARFI imaging in carotids, and made the current research possible, and to Drs. Chris Moore and Murad Hossain, who taught me so much about elastography, and about life in general. Lastly, I would like to acknowledge my funding sources including the 2020 UNC SOM Biomedical Research Core Program Intramural Grant, and the NIH.

Finally, I would like to thank my parents and Elsa, for all your support and motivation to follow my dreams since early age. Mom, you showed me how fun math could be and how my solution paths didn't have to be the same as others, and dad, you taught me to never give up, even when challenges seem impossible. I truly could have not done this without you, and I am very excited to see what the future holds for me.

TABLE OF CONTENTS

LIST OF TABLES

LIST OF FIGURES

LIST OF ABBREVIATIONS

ARFI Acoustic Radiation Force Impulse.

CAL Calcium.

CEA Carotid Endarderectomy.

CME Combined Masson's Elastin.

CNR Contrast–to–Noise Ratio.

COL Collagen.

CRLB Cramer-Rao Lower Bound.

CV Coefficient of Variation.

ECG Electrocardiogram.

H&E Hematoxylin and Eosin.

IMT Intima-Media Thickness.

IPH Intraplaque Hemorrhage.

IRB Institutional Review Board.

IVUS Intravascular Ultrasound.

LRNC Lipid-rich Necrotic Core.

MAD Median Absolute Deviation.

MRA Magnetic Resonance Angiography.

MRI Magnetic Resonance Imaging.

NCC Normalized Cross-Correlation.

OCT Optical Coherence Tomography.

PD Peak Displacement.

RF Radiofrequency.

RPC Reproducibility Coefficient.

SDUV Shear Wave Dispersion Ultrasound Vibrometry.

SNR Signal-to-Noise Ratio.

SWEI Shear Wave Elasticity Imaging.

TRFC Thin or Ruptured Fibrous Cap.

UNC The University of North Carolina at Chapel Hill.

VisR Viscoelastic Response.

VK Von Kossa.

CHAPTER 1

INTRODUCTION

1.1 Purpose

Carotid Endarderectomy (CEA) is one of the most common peripheral vascular procedures performed in the United States, and the most frequent surgical procedure to prevent stroke. Approximately 93,000 CEA procedures were performed in the United States in 2009 [9]. Currently, the main factor for clinicians to indicate CEA is the degree of carotid stenosis. However, previous studies have shown that as many as 13 out of 14 symptomatic patients with 50-69% stenosis, and 21 out of 22 asymptomatic patients with 70-99% stenosis undergo CEA unnecessarily [1, 2, 10]. These data show that degree of stenosis is insufficient as a primary biomarker for stroke risk, and there is still a need for more accurate CEA indication.

Studies have shown that Thin or Ruptured Fibrous Cap (TRFC), Lipid-rich Necrotic Core (LRNC), and Intraplaque Hemorrhage (IPH) are hallmarks of ruptured plaques [11, 12]. These components allow understanding how plaques can progress from clinically benign fibrous cap atheromata to fatal lesions. Additionally, studies have demonstrated that MRI-derived plaque composition is correlated to current and future cerebrovascular events [13, 14, 15]. These data support the clinical relevance of characterizing plaque components to assess stroke risk.

In spite of the high sensitivity achieved by Magnetic Resonance Imaging (MRI) *in vivo*, this imaging methodology presents the following limitations: First, it requires long data acquisition times that cause susceptibility to motion artifacts; additionally, in order to achieve adequate special resolution for carotid imaging, it requires specialized phase-array surface coils [16]. Other limitations of MRI include its cost and lack of portability [13]. An alternative to MRI for assessing carotid plaque composition is CT radiodensity measurement. This modality, however, only allows identification of calcifications and achieves low to moderate accuracy when delineating TRFC, LRNC, and IPH [17, 18]. Additional limitations of CT include its ionizing characteristic, cost and lack of portability

[19]. Studies of ultrasound grayscale echolucency have been shown to correlate with LRNC and IPH, and echogenicity with fibrosis and calcification [20]. However, studies report a wide range of sensitivities and specificities for grayscale-derived composition compared to histology [21]. Another technique is Virtual Histology (VH) ultrasound, which allows classification between fibrous, fibro-fatty, necrotic core and calcium through the interrogation of both the backscatter amplitude and the spectral characteristics of raw radio frequency data [22, 23]. This technique is applied intravascularly, and data have shown efficacy of identifying vulnerable plaque features and elucidated the highly dynamic nature of coronary atherosclerosis [24]. One main limitation of this modality is its invasive nature. Similarly, while Optical Coherence Tomography (OCT) [25] and photoacoustic (PA) [26] imaging have been demonstrated for differentiating plaque features, penetration challenges have limited these modalities to intravascular application, although PA methods exploiting interstitial illumination are in development [27]. A noninvasive, low-cost, portable imaging modality that reliably delineates carotid plaque structure and composition is still a major challenge for improving stroke risk assessment.

The purpose of this dissertation is to develop a method for noninvasively characterizing independent plaque components to assess structure and composition of carotid plaques using ARFI ultrasound. Unlike conventional ARFI imaging, the methodologies developed in this work interrogate the both mechanical and echogenic properties of tissues with the purpose of developing automatic classification algorithms. Therefore, the work presented herein proposes a new atherosclerotic plaque imaging methodology that has the potential to improve clinical ultrasonic plaque characterization, with potential to enhance stroke-risk stratification.

1.2 Hypothesis

The hypothesis of this study is that enhanced noninvasive ARFI ultrasound methods improve discrimination of Calcium (CAL), Collagen (COL), TRFC, LRNC, and IPH in human carotid atherosclerotic plaques *in vivo*, relative to ARFI PD; the following three specific aims were pursued in this work:

Aim 1: Determine which enhanced ARFI-derived imaging method best enables separation of CAL, COL, LRNC, and IPH. Imaging will be performed *in vivo* on 50-99% stenotic plaques. Performance will be assessed by evaluating contrast, receiver operating characteristic, and Bland-Altman analysis, with histological validation, first using semi-automatic segmentation, and then, through a blinded

reader study.

Aim 2: Develop a fully automated, machine learning-based, plaque delineation framework to measure fibrous cap thickness and CAL, COL, LRNC and IPH size. Automatic delineation outcomes will be compared to human reader outcomes for assessing accuracy and precision through receiver operating characteristic and Bland-Altman analyses for measuring each plaque feature size, with histological validation in comparison to reader performance.

Aim 3: Enhance machine learning-based automatic classification of carotid plaque features by incorporating data acquisitions at systole and diastole, and by implementing high frequency and harmonic tracking. Combinations of data inputs will be compared to the outcomes achieved in Aim 2 in terms of accuracy and precision of plaque feature size measurement, with histological validation in comparison to reader performance.

1.3 Overview

Given the urgent yet unmet need for improved biomarkers that differentiate patients' risk of stroke, we have developed a non-invasive imaging methodology to characterize carotid atherosclerotic plaques using Acoustic Radiation Force Impulse (ARFI) ultrasound. Our group conducted a preliminary study in pigs, followed by an initial translation to humans in a pilot clinical study. The outcomes demonstrated that ARFI ultrasound could separate soft and stiff carotid plaque regions. However, this separation was still insufficient: plaque components have different effects over plaque's vulnerability to rupture.

To differentiate plaque components independently, the present project developed advanced ARFI ultrasound techniques to improve plaque characterization. A new ARFI-based biomarker was developed based on the concept that high ARFI-induced displacement variance, which arises in tissue regions with high decorrelation and or low acoustic reflectivity, can be exploited to differentiate tissue types. In this manner, we assessed the temporal variance in ARFI-induced displacement, accentuated by a second time derivative, or 'acceleration'. Thus, this parameter was termed variance of acceleration (VoA). We have demonstrated that VoA is statistically significantly different in regions of IPH, LRNC, COL, and CAL, in a pilot clinical study of 20 human carotid atherosclerotic plaques with histological validation, and further in a follow-on pilot clinical study of 20 human carotid atherosclerotic plaques with histological validation through a blinded-reader study with radiologists using log(VoA) for plaque component delineation.

In the first pilot clinical study, Institutional Review Board (IRB) approval was first obtained (UNC IRB 17-2700), and all patients approved a written consent. Images were acquired the day of surgery prior to patient sedation by a registered sonographer. ARFI imaging was performed on 25 patients (16 M, 9 F; UNC Hospital patients) with clinical indication for CEA. Plaque specimens that were damaged or fractured during surgery were excluded. 20 plaques were retained for analysis after exclusion criteria. Following surgery, the extracted CEA specimens were fixated, and volumetric microtomography (μCT) imaging was performed to match the orientation from ultrasound images. In this way, the location of the ultrasound imaging plane was used to guide histological sectioning. After μCT imaging, samples were sectioned and stained with Hematoxylin and Eosin (H&E), and a combined Masson's elastin stain. Plaque components were delineated in histology by a pathologist. Across all examined plaques, VoA values were statistically significantly different between histologically confirmed plaque components regions of IPH, LRNC, COL, and CAL.

To further increase performance in delineating plaque components, a machine learning framework for automatic classification was developed. ARFI data were used as inputs to a support vector machines (SVM) algorithm to identify four output classes: IPH, LRNC, COL, and CAL. The algorithm was trained by data with spatially-matched histology, and tested by five-fold cross-validation. For all plaques, SVM-output maps achieved higher contrast than independent ARFI parameters and allowed fully automated plaque feature detection. This framework removes user dependence and bias, achieving better accuracy and precision for component delineation.

In the follow-on pilot clinical study, the same protocols for plaque imaging and collection were followed as in [8]. Additionally, performance of the plaque characterization framework was improved by assessing new clinical data from CEA patients at diastole and systole, and applying harmonic imaging. A blinded-reader study was implemented to assess log(VoA) as an imaging marker for differentiating plaque components. Results showed that radiologists achieved higher AUCs than in previous studies evaluating ARFI PD, on average: CAL (0.770), COL (0.760), LRNC (0.790), and IPH (0.820). Additionally, results also suggested that harmonic ARFI and acquisition at multiple points of the cardiac cycle also improve performance for automatic plaque feature delineation by an ML classifier. Specifically, augmented classification models incorporated high frequency and harmonic tracking, achieved the following averaged AUCs: CAL (0.921), COL (0.909), LRNC (0.943), and IPH (941). The work presented in this dissertation represents a substantial improvement towards

noninvasive characterization and identification of vulnerable carotid plaques.

CHAPTER 2

CLINICAL BACKGROUND

2.1 Introduction

Atherosclerosis is a lipid-driven chronic inflammatory disease of arteries, and is the underlying pathology of the majority of cardiovascular-related deaths. Its sequelae, such as stroke and myocardial infarction, have been historically challenging to prevent and characterize, and are the leading cause of death worldwide.

While the origin of atherosclerosis development is still an area under investigation, understanding of its hallmarks and metabolic pathways has improved over the last decades. This chapter will begin with an introduction of the pathological changes occurring due to atherosclerosis, followed by the current clinical system for plaque classification . Next, carotid plaque vulnerability will be assessed and discussed. Finally, therapeutic options for atherosclerosis will be highlighted.

2.2 Atherosclerosis: Current Pathogenesis

Healthy human arteries are composed by three layers. The inner layer, or tunica intima, includes endothelial cells grouped in a single sub-layer, supported by endothelial connective tissue and smooth muscle cells. Next, the middle layer, or tunica media, contains smooth muscle cells embedded in a complex extracellular matrix. Finally, the outer layer, or adventitia, contains mast cells, micro-vessels and nerve endings.

In the beginning of atherosclerosis development, the inner layer is the first affected by adhesion of blood leukocytes to the endothelial region [28]. In particular, studies have shown endothelial cell activation and dysfunction, displaying a pro-inflammatory, pro-thrombotic phenotype with a reduced barrier function [29]. These modification of cellular reactivity and metabolism have been shown to be capable of also affecting lipid metabolism and further influence smooth muscle activity. After the recruitment of inflammatory cells to the intima, newly recruited monocytes express receptors that allow the uptake of modified low-density lipoprotein (LDL) particles, like

oxidized LDL. These particles trigger further inflammatory responses. In addition, risk factors such as hypertension, diabetes and smoking help exacerbate processes that help magnify and sustain inflammation in the arterial wall. Monocytes go on to differentiate into macrophages and attempt to scavenge oxidized-LDL, however they are incapable of clearing the cholesterol-laden proteins and become trapped in the intima. While the foam cells remained trapped, they continue to produce inflammatory cytokines, and also cause more lipoprotein movement into the intima by increasing transcription of LDL-receptor gene. As inflammation propagates, lipoprotein trafficking and oxidation and inflammation can be maintained in the artery for decades, leading into the development of an atherosclerosis lesion.

Atheroma formation also typically involves the activation and migration of vascular SMCs from the medial layer. These cells down-regulate expression of differentiation marker genes, and switch to a remodeling phenotype that includes: migration, proliferation, and an increase in the production of extracellular matrix. This increase leads to the general stiffening of arteries for which atherosclerosis derives its name, and is responsible for the formation of a fibrous cap which covers the growing lesion. Over time, a substantial number of foam cells die forming a cohesive region of extracellular lipids and debris known as a lipid rich pool or necrotic core.

In addition to the formation of a necrotic core, there is the possibility of development of intimal calcification. Calcification tends to occur in one of two forms, either as diffuse microcalcifications, or as large, focal punctate fragments or sheets. Diffuse microcalcifications tend to localize in areas of fibrosis, including the fibrous cap, whereas the larger fragments are typically found in the necrotic core where microcalcifications are able to coalesce. Precipitation of calcium occurs when the local ionic concentration increases over the salt solubility product in the local microenvironment of the plaque. This is known as the passive hypothesis for atherosclerotic calcification. Apoptotic macrophages in particular have been shown to release high concentrations of mitochondrial phosphate and phosphatidylserine-containing molecules that may tip the ionic balance and lead to precipitation. Another hypothesis, driven as an active process, indicates that arterial cells in the atheroma can differentiate into osteoblast-like phenotypes and express potent osteogenic factors. This suggests that calcification may occur in a manner similar to conventional bone formation.

Finally, the most significant complication that can occur during late atherosclerosis is the development of an intraluminal blood clot called a thrombus. Thrombosis arises when plaque

material is exposed to the blood components. This scenario occurs most frequently when the fibrous cap ruptures or fissures uncovering the thrombogenic lipid/necrotic core; an event known as plaque rupture. In many cases, plaque rupture and thrombosis can be a clinically silent event and the body is able to dissolve the thrombus and heal the site of rupture. Indeed, plaques may undergo a number of rupture and healing cycles prior to the event that causes sudden death, and recent studies have shown that a unique constellation of prothrombotic processes (e.g. systemic suppression of fibrinolytic pathways, or increase inflammatory activity) may be necessary to facilitate the final catastrophic occlusion event.

2.3 Atherosclerosis Classification System

The American Heart Association has developed a classification system for atherosclerotic plaques using a numerical value based on the plaque histology [4]. The criteria proposed established six categories of plaque progression, including a starting point of foam cell presence, up to a ruptured plaque with hemorrhage. The categories are detailed in Table 2.1 and will be summarized in this section.

Nomenclature	Histological Characteristics
I	Initial - Isolated macrophage foam cells
II	Fatty streak - Mainly intracellular lipid accumulation
III	Intermediate - Type II changes and small extracellular lipid pools
IV	Atheroma - Type II changes and core of extracellular lipid
V	Fibroatheroma - Lipid core and fibrotic layer, or multiple lipid cores and fibrotic layers, or mainly calcific, or mainly fibrotic
VI	Complicated - Surface defect, hematoma-hemorrhage, thrombus

Table 2.1: AHA-defined types of human atherosclerotic lesions. Adapted from [4].

Type I atherosclerotic lesions consist of the first chemically and microscopically detectable lipid deposits in the intima layer. These lesions are not conventionally visible to the unaided eye and most knowledge about early-stage mechanisms comes as a result from *in vitro* studies. Initial lesions are characterized by isolated and small groups of macrophages containing lipid droplets. Accumulation of macrophages and foam cells have also been correlated with hypercholesterolemia, which causes monocytes to adhere to the endothelium in regions prone to atherosclerosis located in the intima layer [30].

Type II lesions are composed of macrophage foam cells stratified in multiple layers, rather than being present as an isolated cell group like in Type I lesions. Additionally, smooth muscle cells located

in the intima layer now include lipid droplets. Due to the fatty streak characteristic of these lesions, they are visible to the unaided eye, and have been identified in children with infectious diseases and adults with high cholesterol. A present challenge in current studies conveys understanding the procession of type II lesions to vulnerable symptom-producing atherosclerotic plaques [31].

Type III lesions are labeled as pre-atheroma and are considered the intermediate phase between type II lesions and atheromas. Type III lesions are characterized by the presence of microscopically visible extracellular lipid droplets, forming lipid pools among smooth muscle cell layers. At this stage a massive, confluent, well-delineated accumulation of extracellular lipid, i.e., a lipid core, has not yet developed. Studies have shown that the formation of a lipid core, the characteristic component of most advanced lesions, is a consequence of the increase and confluence of the separate extracellular lipid pools in type III lesions [32].

Type IV lesions are composed of extracellular lipid regions occupying extensive and concise regions of the intima layer. The lipid accumulation is known as the lipid core, and causes severe structural disorganization in the intima. This lesion does not cause significant narrowing of the lumen, but can induce formation of fissures. The potential clinical significance of type IV lesions varies according to the location and structure, and may be vulnerable to rupture due to macrophage abundance.

Type V lesions are formed by lipid regions that include prominent fibrous connective tissue. These lesions can be classified into sub-categories depending on their structure and composition. A type V lesion with a lipid core associated with the new fibrous tissue is referred as a fibroatheroma or type Va lesion. A type V lesion with a lipid core and calcifications is referred as a type Vb lesion. Finally, a type V lesion without a defined lipid core and a sparse lipid presence is referred as a type Vc lesion. These lesions are clinically relevant as they may develop fissures, hematoma, and thrombus.

Type VI lesions are the most disruptive and mortal form of atherosclerosis. The lesion can include surface splitting, hematoma, hemorrhage and thrombotic deposits. These types of lesions can also be sub-classified according to the composition. Type VIa indicates surface disruption, type VIb indicates presence of hematoma or hemorrhage, and type VIc indicates thrombosis. These sub-categories can be combined to indicate multiple features, i.e., a type VIabc lesions indicates the presence of all three features.

In 2000, the AHA updated the classification to better characterize the sequence in the evolution of atherosclerotic lesions. The modifications were twofold: Type Vb and Vc lesions were renamed to Type VII and VIII lesions, respectively [33]. This classification is open to updates depending on new developmental sequences with improved resolution and novel scaffolding approaches.

2.4 Carotid Plaque Vulnerability

One of the most critical features of a carotid atherosclerotic plaque is the fast transition from a silent, non-obstructive lesion to one that becomes obstructive and symptomatic. Lesions that are at the highest risk for this behavior have been denominated vulnerable plaques [3]. The transformation is most commonly precipitated by atherothrombosis, a process characterized either by the rupture of the fibrous cap or erosion of the endothelial layer followed by an acute thrombus formation that can occlude the vessel or embolize and obstruct downstream vessels.

The concept of the vulnerable plaque, by and large, was derived from post-mortem histopathological studies done on ruptured coronary plaques [11, 34]. While erosion-prone plaques also fall under the definition of vulnerable, researchers have yet to identify features in precursor lesions that reliably predict erosion, representing a major limitation of the vulnerable plaque paradigm (it is thought that 30-35% of SCD is caused by erosion, compared to 55-60% by rupture) [34]. Therefore, the following discussion on vulnerable plaque characteristics will be limited to the hallmarks of rupture-prone plaques, which include: (1) thin or ruptured fibrous cap, (2) increased inflammation, (3) lipid-rich necrotic core, (4) vascular remodeling, (5) vasa vasorum neovascularization, and (6) intraplaque hemorrhage.

2.4.1 Thin or Ruptured Fibrous Cap

Fibrous cap thickness was one of the first plaque features to be associated with rupture potential. The fibrous cap is a layer of stiff collagenous tissue that protects the soft underlying necrotic core. In the coronary arteries, autopsy studies in men who died suddenly from SCD showed that 95% of plaques with ruptured caps (and consequently, atherothrombosis) had a thickness of <65 μm [35]. In the carotid arteries, the critical value is substantially higher, and has been reported as <200 μm (minimum thickness) and <500 μm (average thickness) [12]. Numerous finite element method (FEM) studies have shown that as the fibrous cap thickness decreases, the circumferential stress experienced by the plaque increases exponentially, which can lead to rupture if the ultimate stress (i.e. maximum stress at failure) is exceeded [36, 37].

In addition to thickness, there are a number of additional factors that can weaken the fibrous cap and make it susceptible to rupture. First, in caps with substantial inflammation, macrophage apoptosis can result in the continuous release of MMPs that can degrade collagen in the cap [38, 39]. Second, loss of SMCs, which produce collagen, can lead to the thinning of the fibrous cap. Finally, high resolution μCT and 3D FEM studies have demonstrated that microcalcifications in the fibrous cap can act as local stress concentrators and cause rupture either through cavitation or interfacial debonding [40].

2.4.2 Increased Inflammation

This condition is characterized by an abundance of T-cells and macrophages in plaques with high vulnerability to rupture. Macrophages increase the vulnerability of the plaque by producing proteolytic enzymes that are capable of degrading extracellular matrix and weakening/thinning the fibrous cap.

In coronary atherectomy specimens from patients with unstable coronary disease, macrophages occupied approximately 14% of the atherectomized culprit lesion [3], whilst macrophages only occupied around 1% in carotid endarterectomy specimens from symptomatic patients. These inflammatory infiltrates are not diffusely spread throughout the plaque, but cluster around the lipid-rich core and in the fibrous cap.

Whilst plaque rupture is always accompanied by local inflammation of the cap, inflammation of morphologically stable plaque types is also a frequent finding. Therefore, inflammation alone is not enough to make a plaque rupture prone; a necrotic core and a thin cap are also required.

2.4.3 Lipid-rich Necrotic Core

The necrotic core is one of the main destabilizing features of the atherosclerotic plaque. It is characterized by a lack of supporting collagen and cells, as well as the accumulation of free/esterified cholesterol. Following plaque rupture, the necrotic core is the most thrombogenic component of an atherosclerotic plaque, estimated to be six-fold greater than collagen due to the high concentration of tissue factor [41].

Initial pathology studies identified a wide range of necrotic core areas that were associated with vulnerability; on the low end, necrotic core areas of 24% and 34% were considered vulnerable [42, 43], while on the high end the values were above 50% [3]. Subsequent FEM modelling studies demonstrated that necrotic core thickness is a better indicator of plaque vulnerability compared to

necrotic core area, and that no single value can reliably confer vulnerability without considering the thickness of the fibrous cap as well [44].

2.4.4 Vascular Remodeling

The majority of advanced plaques do not cause significant luminal narrowing, because the arterial wall expands as a response to plaque development, known as expansive or positive remodelling. Plaques that are not detectable on angiography are often observed in the proximal portions of the coronary arteries with intravascular ultrasound.

Expansive remodelling is common and makes stenotic plaques relatively rare compared with nonstenotic plaques. Ruptured plaques in particular are associated with expansive remodelling and, consequently, most rupture-prone plaques are asymptomatic and nonstenotic at angiographic examination.

2.4.5 Intraplaque Hemorrhage

The phenomenon involving the presence of neovessels tending to be leaky and extravasate erythrocytes into the plaque, is commonly referred to as intraplaque hemorrhage. The release of red blood cells into the sub-intimal space triggers the recruitment of additional macrophages for the purpose of erythrophagocytosis. This can activate pathways leading to macrophage production of matrix metalloproteinases that can disrupt protective fibrosis through collagenolysis [45, 46]. Furthermore, hemoglobin, which is released from lysing red blood cells, can act as a potent inflammatory agent [47, 48].

2.5 Atherosclerosis: Therapeutic Options

The development of a cure for atherosclerosis is still a challenge. Treatment can include a combination of pharmaceutical therapies and lifestyle changes that are intended to reduce risk factors and slow the buildup of plaque. Numerous surgical techniques also exist including procedures to widen/bypass occluded arteries, or procedures to remove plaque that may precipitate a fatal ischemic event. In the following section, these techniques and their efficacy will be described [49].

2.5.1 Pharmaceutical Therapies

Current pharmaceutical therapies for atherosclerosis are targeted to control major risk factors such as hyperlipidemia and hypertension, or controlling hemostasis to prevent thrombosis. Some of the main pharmaceutical therapies are lipid-lowering therapy, anti-platelet therapy, and anti-hypertensive

therapy.

2.5.2 Surgical Procedures

Surgeries vary depending on the location and condition of the target. For coronary arteries, percutaneous coronary interventions are minimally invasive procedures that involve the use of a catheter to treat the arteries. The most common coronary intervention is balloon angioplasty and stent deployment. Coronary artery bypass grafting is an invasive procedure, alternative to a percutaneous coronary intervention. This surgery is open-heart and a healthy artery or vein is connected to the blocked coronary artery forming a bypass for blood to flow around the obstruction.

For carotid arteries, the most common procedure is a CEA, where atherosclerotic plaque is removed from the carotid arteries in order to prevent stroke. The procedure starts with an incision along the front neck to expose the carotid, then it is clamped on either side of the stenosis to remove the inner lining of the artery. The plaque is removed as a block, and most of the medial layer is stripped away. Finally, a patch is sutured to the damaged portion of the artery to avoid re-stenosis, and the artery is closed. While CEA is still utilized in patients with high-grade asymptomatic stenosis, there has been a trend away from surgical management to medical management alone. Current studies suggest that only 5% of patients with asymptomatic carotid stenosis benefit from CEA. Therefore, there is a great need for an improved method of predicting which patients are at high risk for stroke to enhance the benefit and cost-efficacy of surgery or treatment.

2.6 Summary

Atherosclerosis is a silent, dynamic inflammatory disease that is influenced by many factors, including genetics, diet, and lifestyle. If undiagnosed, atherosclerosis can have severe consequences, and potential death. In the last decades, research has allowed better understanding of this disease, with novel procedures and treatments to improve patient's quality of life. Unfortunately, despite great advances, cardiovascular disease remains the leading cause of death in the world. The improvement of therapeutic strategies, early detection, and diagnostic technologies, remain relevant for further reducing this disease mortality. Specifically, medical imaging technologies are needed to both diagnose the presence of vulnerable plaque and also provide a better disease characterization for improving the treatment decision-making process. In the next chapter, the state of the art of atherosclerosis imaging will be reviewed, and current challenges will be discussed.

CHAPTER 3

IMAGING ATHEROSCLEROSIS

3.1 Introduction

Advances in atherosclerosis imaging technology and research have provided a range of diagnostic tools to characterize high-risk plaque *in vivo*. These advances in vascular imaging methods additionally promise great scientific and translational applications beyond this disease. When combined with conventional anatomic- and hemodynamic-based assessments of disease severity, cross-sectional multimodal imaging, and other novel noninvasive techniques can add detailed interrogation of plaque composition, activity, and overall disease burden.

This chapter will begin with an introduction of the general atherosclerosis imaging pipeline. The following sections are organized by imaging type, with detail to different imaging modalities per category.

3.2 Imaging Pipeline

Atherosclerosis imaging encompasses an combination of established and experimental radiological methods and modalities. Broadly, these techniques can be used to detect anatomic and physiological consequences of long-standing atherosclerosis, to provide detail on plaque composition and molecular activity, and to estimate biomechanical stresses acting within the arterial system. Together, these methods provide measures of disease severity, which are indispensable to everyday clinical practice and cardiovascular research.

3.3 Anatomic Imaging

Contrast angiography is the main clinically-used technique for imaging anatomical properties of atherosclerosis. This invasive methodology is most often perform for diagnosing coronary artery disease, where intubation of the coronary is performed with a preshaped catheter introduced through the peripheral arterial sheath, and it is used to inject contrast under x-ray fluoroscopy.

Invasive angiography has a spatial resolution on the range between 0.1 and 0.2 mm with a

temporal resolution of approximately 10 ms. These characteristics allow high diagnostic accuracy for determining severity of coronary luminal obstruction and for guiding clinical management in revascularization. However, the generally low diagnostic yield of coronary angiography, which remains elective, supports initial noninvasive testing. Noninvasive angiography techniques that are standards of practice include computed tomographic angiography and Magnetic Resonance Angiography (MRA), combined with ECG-gating to account for cardiac movement. Currently, computed tomography is preferred over MRA for evaluating coronary imaging in adults. However, MRA is preferred when evaluating carotid arteries and large vessels in general such as the aorta or peripheral arteries.

3.3.1 Duplex Ultrasonography

Ultrasound imaging, specifically duplex ultrasonography (DU), is globally accepted as the first-line diagnosis of stenosis in peripheral vessels. In DU, a combined-imaging mode, conventional B-mode ultrasound is used to visualize the anatomy of the vessel and Doppler imaging is used to measure both systolic and diastolic flow velocities in the artery. Velocity values are then used to derive stenosis percentages, with higher velocities indicating more severe stenosis.

Another common ultrasound metric used to diagnose atherosclerosis is carotid Intima-Media Thickness (IMT), which are typically done in the common carotid artery, and have been used for many years as a biomarker to indicate overall patient plaque burden and cardiovascular risk.

While the mobility and speed of ultrasound are some of its greatest strengths, these features are also a limitation in terms of inter-operator variability. As opposed to MR or CT systems, where a patient lies in an immobile bore, the majority of clinical ultrasound images are produced dynamically by a hand-held transducer that is manipulated into position by a skilled technician. Error in probe placement, or incorrect angle measurement for Doppler studies can result in statistically-variable performance of the technique. Studies have recommended to avoid DU for general population screening with asymptomatic carotid stenosis of 60-99% because the specificity (approximately 92%) results in too many false positives.

3.3.2 Computed Tomographic Angiography

Computed tomographic angiography (CTA) a commonly used first-line diagnostic test for appropriately selected patients with symptoms of angina and a low-to-moderate pretest probability of coronary artery disease. Studies have shown that this technique has an excellent negative predictive

value, providing a reliable means to exclude coronary artery disease when the clinical diagnosis is negative. Computed tomographic angiography is often performed in conjunction with coronary artery calcification imaging, a risk stratification tool that gives an overall estimate of disease burden and risk of future events.

Clinical indications for anatomic CTA assessment have the main objective to improve early clinical decision making for patients with acute chest pain in the emergency department, as an adjunct to invasive angiography when planning complex percutaneous intervention. Additionally, CTA is also used for detection of in-stent restenosis to check patency of coronary artery bypass grafts. Finally, CTA is used to exclude CAD as a cause of left ventricular dysfunction or before cardiac valve surgery, and to understand the 3D anatomic relationship of an anomalous coronary artery to its surrounding structures.

3.3.3 Magnetic Resonance Angiography

Although 2D-Doppler ultrasound is typically the most accessible first-line test to assess for carotid artery disease in patients with recent stroke or transient ischemic attack, MRA is also used routinely for this purpose. Compared with CT, MRI has superior soft-tissue characterization and lacks ionizing radiation.

Obtaining good-quality MRA images is challenging because of motion artefacts arising during prolonged acquisition time and difficulties achieving satisfactory contrast-to-noise ratio, spatial resolution, and volumetric coverage. It is, therefore, not currently recommended for routine clinical use. Recent technological improvements are allowing to provide reliable imaging of the proximal and midvessels. These advances include free-breathing 3D wholeheart acquisition with ECG-gating and navigator respiratory motion correction, high-field magnetic resonance (MR), 32-channel coils with high parallel imaging to accelerate acquisition, T1/T2 spin preparations, and different pulsed sequences to increase signal/contrast-to-noise ratios.

At 1.5 T, MRA can identify coronary stenoses $>50\%$ and identify left main stem and three-vessel CAD. Moreover, improved diagnostic accuracy has been reported with 3T contrast-enhanced whole-heart MRA when compared with x-ray angiography. Absence of significant stenosis on coronary MRA has also been associated with a low risk of subsequent cardiac events when monitored over 2 years.

3.4 Functional Imaging

For patients with more advanced-disease prognosis, a diagnostic strategy that incorporates functional testing over anatomic assessment alone results in overall better symptom control and less invasive procedures. This is in part due to the fact that percentage luminal stenosis does not reliably correlate with hemodynamic obstruction or ischemic burden.

Hemodynamically significant CAD can be determined noninvasively with stress imaging or by pressure-wire assessment during invasive angiography, although these tests are often underused before elective PCI. For functional assessment, exercise is either performed before imaging or simulated pharmacologically with adenosine or another stress-inducing agent. Noninvasive functional imaging modalities include stress echocardiography, cardiac MR with stress perfusion, and nuclear myocardial perfusion scanning with single photon energy computed tomography (SPECT) or positron emission tomography (PET). Fractional flow reserve (FFR) is the most popular invasive functional method, which provides a reliable pressure-based marker of relative coronary flow reserve obtained during maximum pharmacological hyperemia, which is comparable with absolute myocardial blood flow measured by quantitative PET. CT perfusion is another emerging technique, which if combined with coronary CTA has comparable accuracy when evaluated against SPECT, FFR, and MR perfusion.

3.5 Imaging Plaque Morphology and Composition

Beyond conventional anatomic and hemodynamic assessments of disease severity, detailed plaque characterization can be obtained when imaging the vessel wall and inflamed area. Data from autopsy studies performed in patients with carotid artery disease who died suddenly provide the histopathologic basis for high-risk plaque identification and have paved the way for the development of imaging techniques focused on vulnerable plaque imaging [34, 42].

From previous work, the most common underlying plaque morphology leading to myocardial infarction and stroke comprises a thin ruptured fibrous cap with heavy macrophage infiltration and few smooth muscle cells, large necrotic core and overlying intraluminal thrombosis. Intimal neovascularization is a source of intraplaque hemorrhage, which contributes to increased risk of plaque rupture. These features are among the list of recognized high-risk plaque features detectable *in vivo*, however, the role of high-risk plaque imaging in routine clinical practice for risk stratification improvement has yet to be determined [50].

3.5.1 Computed Tomography (CT)

In addition to defining coronary anatomy and luminal stenosis severity, CCTA can provide information on plaque morphology and composition. Although the spatial resolution of CCTA is insufficient to allow measurement of cap thickness, necrotic cores of fibrous caps are typically large enough for detection by CT. Plaques can be readily classified as calcified, partially calcified (<50%), or noncalcified plaques using CCTA. When assessing plaque volume, CCTA tends to underestimate the size of noncalcified plaques and overestimate calcified plaque because of blooming artifact. The sensitivity of CCTA to detect noncalcific plaques with >1 mm intimal thickness on IVUS is approximately 90% [18].

Using absolute CT attenuation values to determine plaque composition is challenging because of the influence of various factors, including size of necrotic core, wall thickness, measurement point, density of intraluminal contrast, slice thickness, and reconstruction filter. Contrast-adjusted attenuation ranges have been proposed to improve accuracy of CCTA plaque component analysis [17].

3.5.2 Magnetic Resonance Imaging (MRI)

MRI is another methodology used for coronary plaque analysis and wall thickness measurement, especially in proximal vessels. Using black-blood MRI, positive remodeling and increased coronary wall thickness has been shown in asymptomatic patients with cardiovascular risk factors. Visualization of wall edema relating to culprit ACS lesions using T2-weighted short inversion recovery sequence MRI has also been reported [51, 52]. Furthermore, hyperintense coronary signal on T1-weighed MRI might serve as a marker of high-risk plaque, which has been linked to clinical angina severity and increased cardiovascular risk [53].

T1 and T2 sequences on multicontrast weighted MRI distinguish plaque components, which exhibit differing relaxation properties and signal intensity. Using this technique, carotid wall thickness can be accurately measured without intravenous contrast on a standard 1.5-T scanner, although better image quality due to improved signal- and contrast-to-noise ratios is seen with higher-field strength 3.0-T MRI. Fibrous tissue displays low signal on T1 and high-signal on T2-weighted MRI, whereas calcium is hypodense on both. Intraplaque hemorrhage causing high-intensity T1-signal and cap rupture has been shown in relation to recently symptomatic carotid plaques.

3.5.3 Intravascular Ultrasound Imaging

Intravascular Ultrasound (IVUS) can provide detailed information about coronary plaque composition in patients with atherosclerosis. An IVUS catheter, constructed from either an electronic phased array or single-element design, generates sound waves in the frequency range from 20 to 60 MHz because of the high-speed oscillatory movement of a piezoelectronic transducer. Gray-scale IVUS has limited ability to differentiate individual plaque components, but added spectral information the backscattered signal, using virtual histology (VH)-IVUS, can be used to detect necrotic core, dense calcium, fibrous, and fibrofatty plaque with sensitivities an specificities ranging from 72% to 99% [54]. However, because of increased noise and artifacts, image interpretation can be difficult, in addition to limitations due to low spatial resolution to reliably and reproducibly detect thin fibrous cap [55].

3.5.4 Ultrasound Elasticity Imaging

The fundamental basis for elasticity imaging of atherosclerosis is that different plaque components have different mechanical properties and, therefore, exhibit distinguishable responses to mechanical excitation.

Noninvasive Vascular Elastography (NIVE) [56] has been demonstrated for differentiating LRNC, with sensitivity ranging from 77-100% and specificity ranging from 57-79%, in a clinical trial, with interesting applications to HIV patients [57] and early vascular change detection in overweight and obese children [58], however, it has not been shown to delineate independent plaque features [59]. Pulse wave imaging (PWI) has recently been implemented in human carotid arteries but presents limitations due to turbulence, flow reversal and reflected waves around the plaque [60]. Supersonic Imaging (SSI)-derived Young's modulus values have been shown to be statistically lower in the carotid plaques of patients with neurological symptoms versus those of asymptomatic patients. Similarly, in patients undergoing CEA, mean SSI Young's modulus was significantly lower in carotid plaques that had "unstable" plaque characteristics (large LRNC and/or IPH) as compared to "stable" plaques [61]. However, the quantitative values of modulus that are reported in the studies are unreliable because they were not derived from the guided wave models. Amassed, these studies strongly support that interrogating the mechanical properties of carotid plaque is a viable approach to differentiating clinically relevant plaque features, and further development of ultrasound-based elasticity imaging could fill the gap in improving stroke risk stratification.

An alternative ultrasound-based approach to noninvasively exploiting the mechanical properties of carotid plaque, has been developed by using Acoustic Radiation Force Impulse (ARFI) ultrasound. In ARFI imaging, a short-duration ($<$100 μs), relative high-energy acoustic pulse generates near the position of the imaging focus impulsive acoustic radiation force. The mechanical excitation is sufficient in magnitude to displace tissue on the order of micrometers. The induced displacements are tracked using conventional ultrasonic methods and used to discriminate tissues with different mechanical properties. For example, stiffer tissues displace less than softer tissues in response to the same ARFI magnitude. Importantly, ARFI imaging is safe for carotid plaque imaging. Previous ARFI imaging studies conducted have shown that atherosclerotic plaque characterization by ARFI is feasible. More specifically, previous ex vivo and in vivo studies involving spatially matched histological validation of ARFI imaging results, demonstrated that high-risk plaque components can be differentiated with average area under the receiver operating curve of 0.86.

3.6 Summary

This chapter described a number of vascular imaging techniques, and assessed their efficacy for imaging atherosclerosis. Currently, the clinical standard is based on angiographic-type modalities. However, novel MRI and IVUS-based methodologies have been proven efficient for predicting patient risk. The improvements in atherosclerosis imaging have also led to an increase in the anatomical and functional understanding of atherosclerosis pathology, which allows further development of novel treatment and clinical management procedures. Unfortunately, many of the plaque characterization modalities have significant drawbacks in terms of cost (for MRI) and patient safety (for IVUS and CT), which may preclude them for being applied as routine screening tools. Advances to noninvasive ultrasound using elastography, as will be described in the next chapter, have the potential to lead to further advances in diagnosis and treatment of atherosclerosis, as well as allowing an easier access for patients to be screened for plaque characterization.

CHAPTER 4

ULTRASOUND ELASTICITY IMAGING

4.1 Introduction

Ultrasound elasticity imaging or elastography is an imaging technology sensitive to tissue stiffness, and it was first proposed in 1995 [62]. For the past few decades, this technology has been further developed and optimized to enable clinically-applied qualitative and quantitative assessments of tissue stiffness. Elastography methods take advantage of the changed elasticity of soft tissues resulting from specific pathological or physiological processes, i.e., many solid tumors are known to differ mechanically from surrounding healthy tissues.

In this chapter, a brief background on ultrasound imaging is given first, followed by a brief overview on ARF and different ARF-based imaging methods that are used for arterial imaging. Finally, acoustic radiation force impulse (ARFI) imaging, a qualitative technique, is discussed, which is the technological foundation for this dissertation.

4.2 Overview of Ultrasound Imaging

Ultrasound imaging, or sonography, is a non-ionizing technique that uses high frequency acoustic waves (typically 3 MHz - 15 MHz) to make tomographic images of tissue structures. As ultrasound waves travel through the body, they encounter interfaces between tissues and are partially reflected back toward the ultrasound transducer. The proportion of the wave that is reflected versus transmitted across the interface is related to the tissues acoustic impedance, which is given by the product of the tissue density, and speed of sound.

As the sound waves propagate, they are attenuated, scattered, and reflected, producing echoes from the various interfaces. The transducer receives the returned echoes, which are digitalized and sent to the receive beamformer. Then, images are made by recording the ultrasonic echoes and assigning grayscale values to their intensities. This mode of imaging is known as pulse/echo ultrasound, and results in a one dimensional tomographic data set (amplitude vs. depth) referred to

as a Radiofrequency (RF) line. RF data is then envelope-detected and log compressed to form an amplitude line (A-line), which encodes the intensity of the echo at a given depth position.

To create two-dimensional images, successive A-lines are taken at various positions across the tissue of interest and compounded together to create a brightness mode (B-mode) image. A-lines can also be fired sequentially in the same location in a technique known as motion mode (M-mode), which is used to track motion such as blood flow. Variations on M-mode sequencing underlie the flow mapping techniques of pulsed, color, and power Doppler that are utilized to perform non-contrast angiography-style imaging with ultrasound.

4.3 Ultrasound Elasticity Imaging

Unlike conventional B-mode ultrasound imaging that differentiates features with dissimilar acoustic properties, elasticity imaging methods differentiate features with different mechanical properties. Because malignancies and pathologies will exhibit different mechanical properties than the surrounding tissue, elasticity imaging methods are being developed to examine tissue health and monitor disease progression. To do this, these techniques have two phases: first, tissue is excited, and second, the deformation response is monitored. The source of the excitation used to produce the tissue deformation can be extrinsic, as in compressive elastography, or intrinsic, by using radiation force.

4.3.1 Compression Elastography

In this technique, a handheld ultrasound probe is used to compress tissue while performing real time imaging to measure the deformation. Displacements are monitored with speckle-tracking algorithms by comparing pre-compression and post-compression images, and are used to determine the strain field. By assuming the applied stress is uniform and the material is elastic, differences in the measured strain are attributed to differences in the elasticity of the tissue.

Compression elastography has demonstrated promising clinical applications for evaluating thyroid, breast, liver, and prostate lesions. This technique can be performed in real-time clinically. Unfortunately, tissue compression causes signal decorrelation, limiting the accuracy of displacement estimates and the strain estimates formed from them. Elastography is also limited because the deformation field decreases with depth, making it difficult to make measurements in deep tissue. Furthermore, the applied pressure is caused by a free-hand technique making the measurements operator dependent, which impacts reproducibility.

4.3.2 Acoustic Radiation Force (ARF)

Radiation force is a phenomenon in wave motion where part of the energy of the travelling wave is converted into momentum after experiencing absorption, scattering, or reflection. In 1902, radiation force was found to be associated with acoustic waves by Lord Rayleigh [63]. Decades later, in 1990, acoustic radiation force (ARF) was proposed to be utilized as an extrinsic excitation source for elasticity-based medical imaging techniques [64].

Acoustic radiation force (ARF) is defined as a unidirectional body force generated from the transfer of momentum from an acoustic wave to the propagating medium [65]. The transfer of momentum occurs with energy-loss mechanisms such as absorption, scattering, and reflection, therefore the derivation of acoustic radiation force cannot be directly obtained from the purely elastic stress-strain relationships. Using the Navier-Stokes equation, ARF is approached using the balance of linear momentum equation. In order to simplify the magnitude of ARF at an specific spatial location, soft tissues can be approximated as linear, isotropic, elastic solids with the following balance of linear momentum equation (adapted from [65]), defined as 4.1,

$$\nabla\sigma + f = \rho a \tag{4.1}$$

where ∇ is the divergence operator, σ is the Cauchy stress tensor, f represents an external steady-state force, ρ is the material density, and a is an external force. When the perturbative expansion of equation is used, the radiation force can be related to the change in momentum, so that the second-order balance of linear momentum can be expressed as 4.2,

$$F = \nabla p_2 - \mu_f \nabla^2 v_2 \tag{4.2}$$

$$F = \rho\langle v_1 \nabla \cdot v_1 + v_1 \nabla v_1 \rangle \tag{4.3}$$

where $\langle\rangle$ is the time-average quantity, p_2 is the second order pressure term, and v_1 and v_2 are the first and second order terms in the expansion of particle velocity. For the case of a plane wave, 4.3 can be reduced to 4.4 as,

$$F = 2\rho\langle v\nabla v\rangle \tag{4.4}$$

Further, taking into consideration that the solution for the attenuating wave equation, i.e., an expression of the output particle velocities derived in [65] can be simplified to,

$$v(x,t) = j\omega A_0 e^{-\alpha x + j(\omega t - kx)} \tag{4.5}$$

where v is the particle velocity, x and t refer to the particle's position and time, ω is the angular frequency, A_0 is the initial wave amplitude, α is the frequency-dependent attenuation coefficient of the material, and k is the wave number. Substituting 4.5 into 4.4, the magnitude of the presented acoustic radiation force can be expressed as,

$$|F| = A_0^2 e^{-2\alpha x}\rho\alpha. \tag{4.6}$$

Finally, the magnitude of the acoustic radiation force for any spatial location can be calculated as,

$$|F| = \frac{2\alpha I}{c} \tag{4.7}$$

where F is the force per unit volume, c is the sound speed in ms^{-1}, α is the absorption coefficient of the tissue in $Np\ m^{-1}$, and I is the temporal average intensity in Wcm^{-2}at that spatial location.

The main limitation from the approximation in 4.7 is the underestimation from the true radiation force magnitude in tissue due to the second order approximation. Specifically in tissue, an acoustic wave with high amplitude and short duration experiences significant nonlinear distortion, which results in the formation of harmonics and consequently, an increase in absorption. Additional studies have modified the ARF equation approximation to include higher order terms [66, 67].

In conventional ultrasound imaging, the magnitude of the acoustic radiation force is relatively small, producing negligible displacements in tissue (< 1 μm). To generate measurable displacements, ARF methods use longer and/or higher intensity acoustic pulses than what is used for B-Mode imaging. In practice, acoustic radiation force magnitudes on the order of dynes can produce displacements in the range of 1-10 μm. The amount the tissue displaces and the time needed for the

subsequent recovery are dependent upon the mechanical properties of the tissue, which is exploited in the imaging techniques described in later sections. Peak ARF magnitudes *in vivo* are approximately in the range from 1 to 10 μm. These magnitudes are within the FDA-regulated diagnostic ultrasound limits for mechanical index (MI), thermal index (TI), and spatial peak temporal average intensity (I_{SPTA}). Studies using finite element method (FEM) models and experimental validation have shown that ARF-based method heat tissue less than 1°C, below the FDA limit of 6°C [68, 69].

ARF-based imaging has been shown to be clinically useful in a variety of applications including breast, gastrointestinal tract, liver, kidney, and prostate. Nightingale et al. developed the first implementation of ARFI *in vivo* in the human abdomen, bicep, thyroid, and breast [70]. Specifically, their results supported the clinical feasibility of a radiation remote palpation imaging system.

4.4 Vascular ARF-Based Imaging

One of the main benefits of using ARF-based imaging is the highly programmable focus and spatial precision that non-ARF imaging techniques can't achieve. Specifically for vascular applications, resolution and precision are essential to properly characterizing artery wall composition and structure. The primary ARF-based imaging techniques that have been developed for vascular imaging include vibroacoustography, shear wave elasticity imaging, shear/lamb wave dispersion vibrometry, and acoustic radiation force impulse imaging.

4.4.1 Vibroacoustography (VA)

Vibroacoustography is an ultrasound-based method to detect vascular calcifications [71].This technique uses ARF produced by 2 intersecting ultrasound beams at slightly different frequencies to induce a vibration (in the kHz range) of the tissue from a distance. A 2D image is generated from the vibration-induced acoustic emission signal. This signal depends on the tissue stiffness and its acoustic properties [72].

This technique was first implemented in a water bath, and achieved successful detection of calcium deposits excised in *ex vivo* tissue, with X-ray validation [73]. Further, this technique was also applied *in vivo* in porcine femoral arteries, producing high-resolution and speckle-free images. Results from this study indicated that vibroacoustography-based measured calcium areas were comparable *in vivo* and *in vitro*, and measurement of the artery's diameter was also comparable between vibroacoustography and conventional ultrasound [5]. Overall, sensitivity and specificity for calcium detection was 100% and 86%, respectively [5], demonstrating potential for clinical

implementations. Figure 4.1, adapted from [5], shows an example of a calcified arterial plaque (A) photographed and imaged *in vivo* with (B) vibroacoustography and (C) X-ray.

The main advantages of this methodology are the lack of speckle present that allows better contrast when identifying calcium, with similar contrast as X-ray but without any ionizing radiation. Additionally, this technique was implemented in a clinical ultrasound scanner (GE HealthCare Ultrasound Cardiology, Horton, Norway) for translation to a clinical setting [74]. A main limitation of this technology is scan duration. When using a confocal transducer, the scanning duration was 7-8 minutes, whereas when using a linear array transducer, the duration was one minute. Additionally, standing wave artifacts are another limitation, due to long ultrasound transmissions and acoustic reverberation. A complete plaque characterization, specifically identifying other plaque components different than calcium, is still an area for future work in refining the approach for estimating viscoelastic properties of tissue [75].

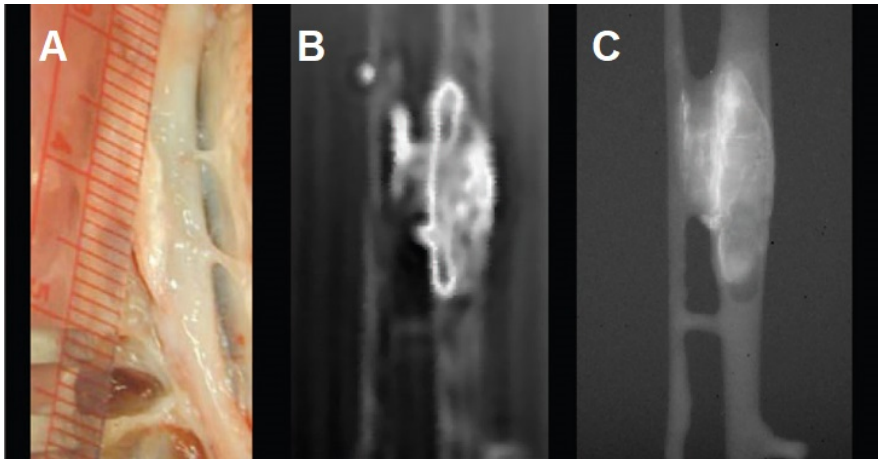

Figure 4.1: Femoral calcified arterial calcified plaque. (A) photograph of the artery showing the plaque calcification. (B) Vibroacoustographic, and (C) X-ray images of the excised specimen. Reprinted from [5] (Copyright © 2008 Wolters Kluwer Health Inc.)

4.4.2 Shear Wave Elasticity Imaging (SWEI)

Shear Wave Elasticity Imaging (SWEI) is a quantitative methodology where an ARF push is applied to induce a shear wave [76]. As the shear wave propagates through the medium, it can be tracked through time. The velocity by which it propagates is directly related to the medium elasticity, and can be quantified to obtain its Young's modulus [77]. The motivation for applying this methodology to plaque imaging is SWEI's capability to differentiate fatty from fibrotic tissue with

high performance [78, 6]. A commercialized extension of SWEI based on using multiple ARF bursts at different axial depths is supersonic shear imaging (SSI). This approach creates a constructively interfering planar shear wave that propagates in a Mach-cone, and is tracked using plane wave beamforming and coherent compounding to achieve framerates between 3 kHz and 5 kHz. Other methods to produce shear waves have been developed to include an axial focus of two ultrasound beams or spatially modulating ultrasound to produce shear waves [79, 80]. SWEI technology has been implemented commercially by multiple ultrasound companies such as Siemens, Philips and GE. SSI has been commercially implemented by Hologic Supersonic Imagine.

SWEI has been assessed in multiple clinical studies to characterize carotid plaque in patients, having cohorts from 22 [81] to 199 [82]. SWEI has been assessed for understanding plaque vulnerability with multiple ultrasound machines using different configurations, both *in vivo* and *ex vivo* [50]. Some studies have compared SWEI to echogenicity, as a reference standard, to assess plaque rupture vulnerability [82, 83, 61]. However, a limitation of this assessment is that echogenicity has been proven to be insufficient for a complete plaque characterization and is not a gold standard [84]. Additionally, studies have reported the feasibility of using SWEI in carotid arteries and found statistically significant differences in elasticity in both the arterial wall and plaques. In carotid artery plaques, stiffness values have been reported to be lower in plaques from symptomatic patients compared to asymptomatic plaques [6]. Figure 4.2, adapted from [6], shows an example of a carotid plaque SWEI elastogram with labels 1-4 indicating wall and labels P1 and P2 indicating plaque. Overall, SWEI-derived elasticity values widely vary among studies, with additional variability on each study, depending on the plaque characteristics. SWEI has also been applied in phantoms and in a healthy volunteer [85], and has been shown to identify vulnerable plaques.

The main advantages of this methodology are quantitative elasticity measurements from the previously cited studies correlate with computed tomography angiography and pulse wave velocity, clinically. Aditionally, SWEI reproducibility was achieved with less operator dependence than conventional ultrasound [83]. The main limitations of this methodology are that SWEI results are affected by dispersion, specifically by viscosity changes through the plaque. Additionally, shear waves generated have approximately 1-10 mm wavelength, therefore, internal reflections between plaque components strongly affect shear wave propagation, affecting the overall elasticity results. This problem is reduced with higher frequencies; however, higher frequencies also have higher attenuation.

Finally, despite *in vivo* SWEI resolution being reported in the range between 0.3 - 1 mm^2, studies use regions of interests that encompass the whole plaque, without assessing plaque components independently.

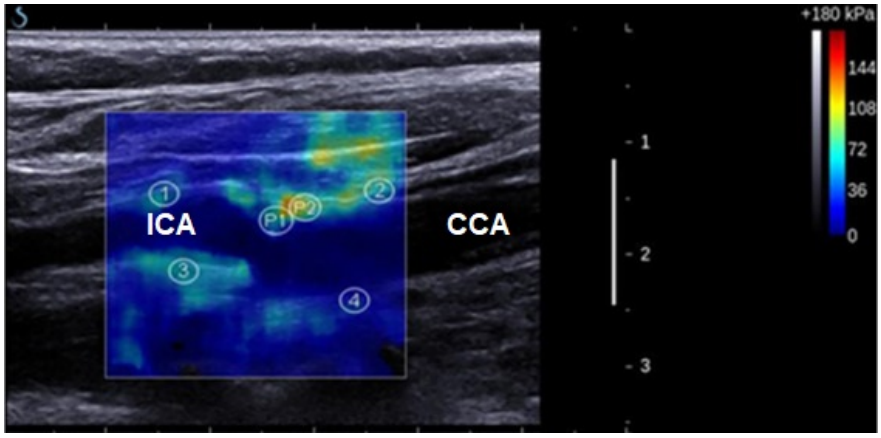

Figure 4.2: Example carotid artery in a patient with 30%-40% stenosis. The elastogram of the internal carotid artery (ICA) and commom carotid artery (CCA) is shown. Six 2-mm circular regions are shown, in the anterior (1) and posterior (3) ICA, anterior (2) and posterior (4) CCA, and inside the plaque (P1 and P2). Reprinted from [6] (Copyright © 2014 Springer Nature)

4.4.3 Shear/Lamb Wave Dispersion Vibrometry and Spectroscopy

Shear Wave Dispersion Ultrasound Vibrometry (SDUV) [86] and Lamb Wave Dispersion Vibrometry (LDUV) [87] are ARF-based imaging approaches that measure mechanical wave propagation to obtain viscoelastic tissue properties. SDUV generates multi-frequency wide-band harmonic shearwaves using both an ARF push and external mechanical vibration to obtain a shear wave speed dispersion curve, and further estimate tissue elasticity and viscosity. Different configurations of SDUV are developed using combinations of ARF and external vibration sources [88].

SDUV's methodology is based on using amplitude modulated ultrasound to generate a monochromatic shear wave and measure its phase velocity using a phase gradient method. With multiple measurements, shear wave speed can be measured at multiple locations along the propagation path, and a linear regression can be performed to robustly calculate the phase velocity. Using several modulation frequencies, this technique was first implemented in phantoms using a bandwidth of 200 to 800 Hz [88]. An alternative to multiple measurements has been proposed through one acquisition with significant energy in multiple frequency components in a single sequence [86]. For vascular applications, SDUV has shown potential for characterizing viscoelasticity in walls of excised arteries,

specifically indirectly measuring attenuation via characterizing the ratio between the decay rate and frequency for an artery [89]. Additionally, SDUV was applied for measuring the Young's modulus of *ex vivo* porcine carotid arteries and customized tube phantoms with compressive mechanical testing validation [7].

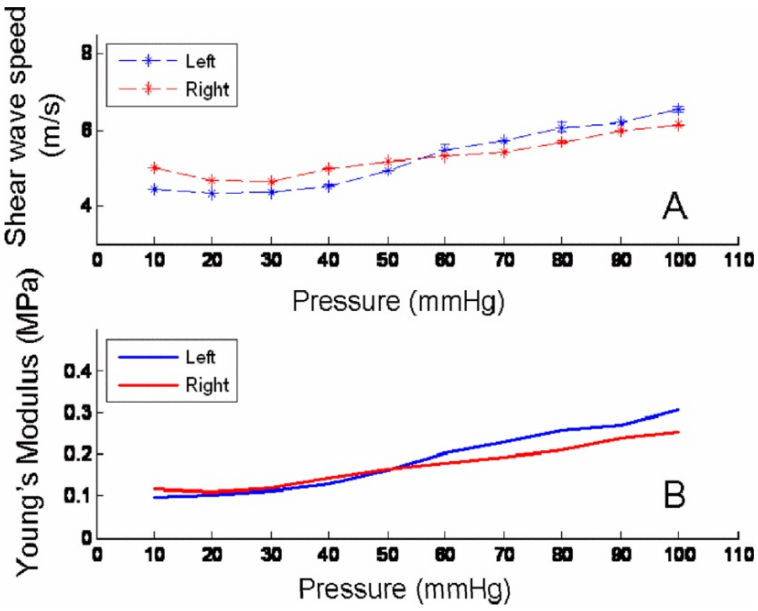

Figure 4.3: Example left and right excised porcine carotid arteries. (A) SDUV-generated shear wave speed of the arteries from an initial pressure of 10 mmHg until 100 mmHg. (B) Yound's moduli of the arteries as a function of increased pressurization. Reprinted from [7] (Copyright © 2009 IEEE)

The main advantages of this methodology are they provide estimation of both elastic and viscoelastic properties, which has been reported to have potential for characterizing arteries clinically [90]. The main disadvantages of this methodology are that multiple measurements are required while varying the modulation frequency, in addition to the limited spatial and temporal resolution for characterizing plaque composition and structure.

4.4.4 Acoustic Radiation Force Impulse (ARFI) Imaging

ARFI imaging is an imaging approach that employs an ARF push to qualitatively assess tissue properties on the same axis where the push was delivered. In this approach, one-dimensional axial displacements induced in the location of force application are considered to reflect relative tissue mechanical properties. ARF-induced displacement profiles are conventionally calculated using correlation-based time delay estimators [91]. Unbiased estimators, such as normalized cross-correlation, Loupas [92] or Kasai [93] methods, are fundamentally limited by the Cramer-Rao Lower

Bound (CRLB) and biased estimators, such as the Bayesian speckle traking approach can surpass the CRLB [94]. Parameters derived from displacement profiles have been used for characterizing tissue property, these include the magnitude of displacement at a given time, Peak Displacement (PD) magnitude, time to peak displacement, and the time to a specific percentage recovery from peak displacement.

Initial applications of ARFI imaging for arterial plaque characterization include studies performed *ex vivo* in human femoral and popliteal arteries [95]. These initial results and further *in vivo* porcine model [96, 97] results showed that lipid necrotic areas had higher displacement than areas with fibrosis and calcification. ARFI imaging was further assessed in terms of performace through a blinded reader study for identifying *ex vivo* plaque components [98]. Results from this study indicated ARFI peak displacement's performance for identifying calcium (sensitivity: 96%, specificity: 85%), lipid core (sensitivity: 80%, specificity: 86%), and fibrous cap (sensitivity: 86%, specificity: 82%). ARFI imaging was then implemented in humans *in vivo* [99], and subsequently implemented in patients undergoing carotid endarderectomy with matched histology [100] and carotid magnetic resonance imaging [90].

In addition to previous studies, a blinded-reader clinical feasibility study for identifying plaque components and measuring fibrous cap thickness assessed ARFI imaging in 25 patients (16 M, 9 F; 0 children; all caucasian) with clinical indication for CEA using a Sonoline Antares and VF7-3 transducer. Images were acquired the day of surgery prior to patient sedation by a registered sonographer trained in ARFI and peripheral vascular imaging. The carotid bifurcation and internal carotid artery (ICA) were imaged longitudinally, using electrocardiogram (ECG) gating to diastole. The ARFI imaging focal depth was chosen based on the location of the plaque. From the acquired raw RF data, parametric images of ARFI-induced peak displacement were rendered with color scaling to [median $\pm$ 2 x median absolute difference], as described in [98].

After surgery, the extracted CEA specimens were labeled (proximal/distal relative to the heart) by the surgeon, photographed, and then transferred to 10% neutral-buffered formalin. After fixation, volumetric *ex vivo* μCT imaging was performed on the samples at 20-μm isotropic voxel resolution. In the μCT, plaque volumes were segmented into two tissue types, calcifications and soft tissue. Then, the μCT volume was rotated to match the internal/external carotid artery orientation from *in vivo* transverse B-Mode images captured at the time of ARFI imaging. In this way, the location

of the ultrasound imaging plane was located and used to guide histological sectioning. After *ex vivo* imaging, samples were decalcified, and marked with tissue marking dye to indicate sample orientation.

Then, the tissue was embedded in paraffin, sectioned, and stained with H&E and a combined Masson's elastin (CME) stain for collagen and elastin. Figure 4.4 shows an example of this processing of the carotid B-Mode and ARFI peak displacement images with matching μCT and histologic sections. Histology images were graded by a pathologist with experience in atherosclerosis using a custom GUI. Similarly, the spatially-matched ARFI PD images were graded by six trained, blinded readers (two neuroradiologists, an abdominal radiologist, a sonographer, an interventional cardiologist, and a pathologist who did not read the histology images) using a custom GUI. The median AUCs for each feature were as follows: lipid-rich necrotic core, 0.809; dense collagen, 0.696; intraplaque hemorrhage, 0.639; calcium, 0.612. The median AUC for the combined metrics were 0.859 for collagen/calcium and 0.887 for necrotic core/intraplaque hemorrhage. Performance was dependent on reader specialization, with radiologists achieving the highest AUCs for detecting combinations of collagen/calcium and necrotic core/intraplaque hemorrhage, *in vivo* in human carotid plaques. Specifically, the results revealed that while PD effectively detected soft (median AUROC = 0.887) and stiff (median AUROC = 0.859) plaque features, PD was not as successful at distinguishing between different plaque components that exhibited similar PDs (median AUROCs < 0.65).

Additionally, readers were able to measure average FC thickness down to 0.49 mm with close agreement to histologically measured thickness. Specifically, the reader with the closest agreement with histology for FC thickness measurement achieved a coefficient of determination (R2) value of 0.64. Radiologists on average had a statistically significant positive bias (0.12 ± 0.30 mm; P = 0.037). These encouraging preliminary results support that ARFI is relevant to delineating human carotid plaque features *in vivo* but suggest that further technology development is needed to improve discrimination.

The main advantages of this methodology include higher spatial resolution compared to SWEI and SDUV for characterizing plaque composition, with studies demonstrating *in vivo* feasibility for differentiating grouped stiff from grouped soft carotid plaque components, in addition to real-time implementation capabilities. The main limitations of this methodology are that ARFI imaging is a qualitative measurement in comparison to SWEI and SDUV, which provide quantitative outputs.

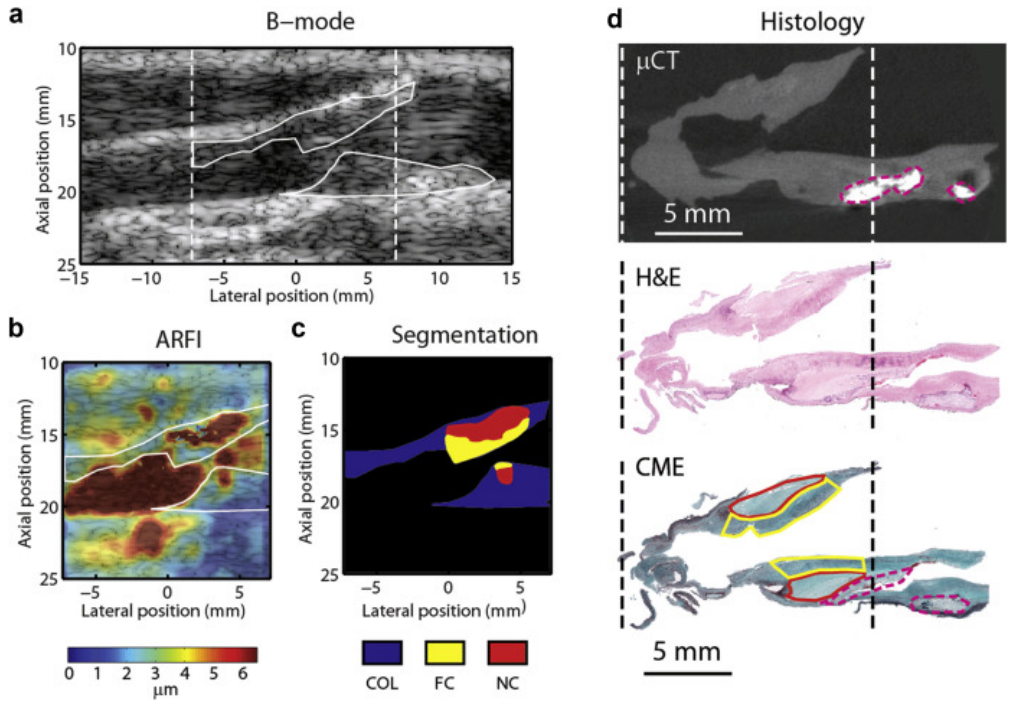

Figure 4.4: Example internal carotid artery from a symptomatic patient. (a) B-Mode image, (b) ARFI peak displacement image, and (c) ARFI-based segmentation is showed with (d) matching microcomputed tomography and histologic sections. Reprinted from [8] (Copyright © 2017 ScienceDirect)

Additionally, similarly to SWEI and SDUV, clutter artifacts, caused by scattering from off-axis tissue inhomogeneities, sound reverberation between tissue layers, and random acoustic noise, cause displacement error and contrast reduction between different plaque components in ARFI-derived images.

4.5 Summary

The fundamental basis for the application of elastography to characterize atherosclerosis is that different plaque components have different mechanical properties and, therefore, exhibit distinguishable responses to mechanical excitation. Unlike compression elastography, ARFI ultrasound uses an acoustic radiation impulse to displace small tissue volumes at a precise focal position. This technique does not rely on the characteristics of propagating shear waves but only on displacements achieved in the region of excitation. Previous ARFI clinical plaque characterization studies have shown that trained radiologists achieved AUCs of 0.86 and 0.89 for detecting grouped collagen/calcium and grouped necrotic core/intraplaque hemorrhage, respectively, *in vivo* in ARFI images of human carotid plaques [8]. These encouraging preliminary results showed that ARFI PD allows differentiation of

soft from stiff plaque areas and highlighted ARFI potential for delineating human carotid plaque features *in vivo*. From these encouraging results, further ARFI imaging development to improve differentiation between individual plaque components will be presented in the next chapters. In summary, previous studies demonstrate the relevance of interrogating the mechanical properties of carotid plaque as an approach to differentiating plaque features, and further development of ultrasound-based elasticity imaging could improve stroke risk assessment.

CHAPTER 5

ARFI DISPLACEMENT VARIANCE

5.1 Introduction

Given the background presented in the previous chapter, the lack of a low-cost, noninvasive imaging method that reliably delineates carotid plaque structure and composition and is suitable for widespread diagnostic application represents a major gap in improving stroke risk stratification. ARFI ultrasound presented successful results for delineating stiff and soft areas of carotid atherosclerotic plaques and motivated further advancement of ARFI technology to enhance carotid plaque imaging. However, inability to distinguish between soft LRNC and IPH features impairs ARFI's clinical relevance to atherosclerosis imaging because LRNC has a lower hazard ratio (3.00) than IPH (4.59) in regard to predicting subsequent stroke/transient ischemic attack. Thus, differentiating IPH from LRNC could improve identification of patients in need of invasive interventions, such as a CEA, to prevent stroke versus those that could safely be managed pharmaceutically [101]. Similarly, inability to distinguish between stiff COL and CAL diminishes ARFI's utility for atherosclerosis imaging because diffuse COL deposition is generally considered stabilizing to plaques, while CAL deposits may be stabilizing or destabilizing depending on their size and location. Thus, knowledge that a stiff region in a carotid plaque is COL as opposed to CAL could improve stroke risk assessment and facilitate medical management.

This chapter [1] presents a derivation and evaluation of ARF-based outcome parameters to differentiate plaque components as an alternative to using ARFI PD. These parameters exploit signal correlation and signal-to-noise ratio (SNR), which vary between plaque components according

[1] *© 2019 IEEE. Portions reprinted with permision, from Torres, G., Czernuszewicz, T.J., Homeister, J.W., Caughey, M.C., Huang, B.Y., Lee, E.R., Zamora, C.A., Farber, M.A., Marston, W.A., Huang, D.Y., Nichols, T.C., and Gallippi G.M., "Delineation of human carotid plaque features in vivo by exploiting displacement variance," IEEE transactions on ultrasonics, ferroelectrics, and frequency control, 66(3), pp.481-492.*

to displacement and echogenicity, respectively. Thus, relative to evaluating PD alone, evaluating signal correlation could improve discrimination of plaque features by mechanical property. Further, evaluating SNR enables discrimination of plaque features by echogenic property. In addition to outright signal correlation and SNR, we evaluate if displacement estimation variance, which is a function of both correlation and SNR, improves discrimination of plaque features. We hypothesize that signal correlation and SNR can be exploited, outright or via displacement variance, to improve discrimination of carotid plaque features relative to PD in transcutaneous ARFI imaging. This evaluation is performed by deriving correlation, SNR, and displacement variance parameters from the same ARFI data previously acquired *in vivo* from the carotid plaques of 25 patients undergoing clinically indicated carotid endarterectomy [8].

5.2 Methods

As described above, all analyses were applied to previously collected *in vivo* human carotid plaque data, the acquisition and nature of which have been described in detail previously [8] in Chapter 4.4.4. Briefly, 25 patients undergoing clinically-indicated CEA were recruited from The University of North Carolina at Chapel Hill (UNC) Hospitals. The UNC IRB approved all procedures in this study. Informed consent was given from each study participant (ClinicalTrials.gov No. NCT01581385). From the 25 patients, 5 plaques met the exclusion criteria outlined in [8] and were not considered.

The examined plaques were imaged *in vivo* prior to surgery using a Siemens Acuson Antares (Siemens Healthineers, Ultrasound Division, Issaquah, WA) and a VF7-3 linear array with Electrocardiogram (ECG) gating to diastole, and the CEA specimens were collected following surgery for histological validation of imaging results. The extracted plaque specimens were imaged with volumetric micro-CT. Micro-CT volumes were segmented into calcium and soft tissue and were aligned with morphology on the B-Mode frame (acquired simultaneously with ARFI data) to identify the proper sectioning plane to achieve spatial alignment of ARFI and histology data. Sections were stained with hematoxylin and eosin (H&E), Von Kossa (VK) for calcium, and Combined Masson's Elastin (CME) for collagen. Figure 5.1 provides a flow chart of this procedure from an example carotid plaque in a 71-year-old symptomatic male. The histology images were read by a pathologist experienced in atherosclerosis, who marked regions of COL, CAL, LRNC, and IPH. The reader is referred to our prior publication for more detailed descriptions of the study population, ultrasound data acquisition, and histological processing methods.

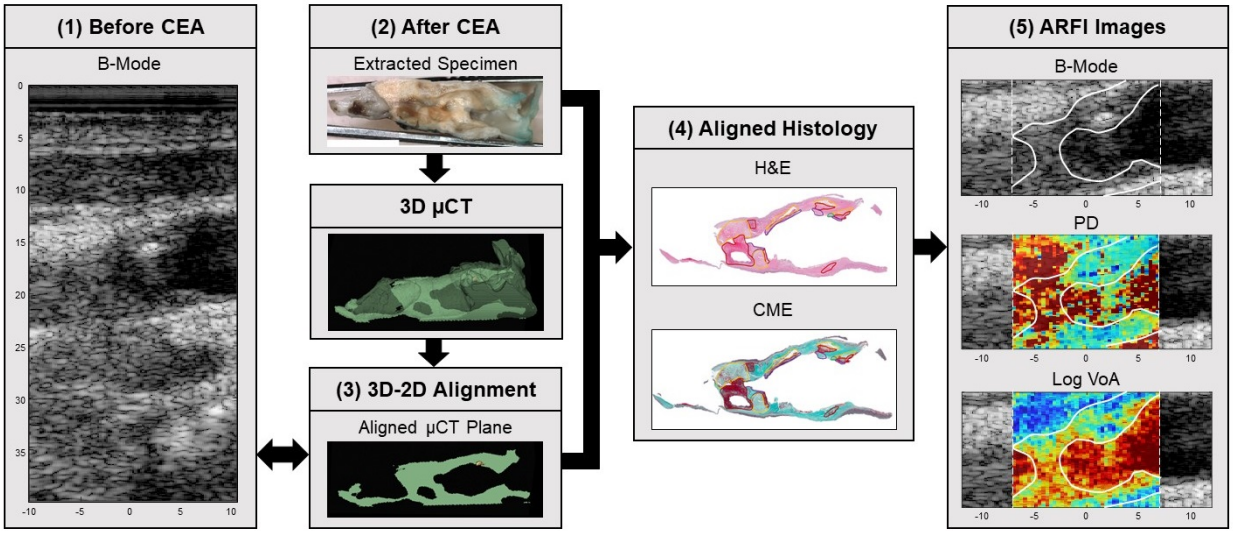

Figure 5.1: Procedure for aligning histology and ARFI images. (1) Before CEA, *in vivo* B-Mode (and matched ARFI) data are recorded from the plaque. (2) After CEA, a μCT volume of the extracted specimen is rendered. (3) Using anatomy and morphology in the B-Mode image, an aligned plane is located along the μCT volume. (4) This aligned μCT is used to identify the plane for sectioning the specimen during histological processing such that the histology and ultrasound imaging planes are aligned. (5) Finally, features identified by the pathologist on the spatially-aligned histology slides are used as validation for parametric ultrasound image analysis. The depicted carotid plaque example is from a 71-year-old symptomatic male.

5.2.1 Outcome Parameter Estimation

Outcome parameters were systematically generated, as indicated in Figure 5.2, for three input data sources: 1) ARFI-induced displacement, 2) cross-correlation coefficient (CC), and 3) radio frequency SNR. All three data sources were evaluated over ensemble time. ARFI-induced displacement and CC were calculated using one-dimensional axial Normalized Cross-Correlation (NCC) with a kernel length of 1.5λ [91]. Note that the selection of this kernel length is based on a previous study [37] that evaluated the tradeoff between bias in plaque feature size estimates with large kernel sizes and noise in displacement estimates with small kernel sizes. Radio frequency Signal-to-Noise Ratio (SNR) was calculated as μ/σ, where μ represents the signal amplitude in each independent pixel per frame, and σ represents the noise component, which was calculated as the average signal amplitude in a 3x3 mm anechoic region inside the lumen of each carotid artery. The size of the noise region was selected as the size of the largest anechoic region consistently recognizable in all of the carotid images. The three sources of input data were each evaluated in terms of the nth time derivate (with n = 0, 1, 2, and 3), the decadic logarithm of the nth time derivate, the temporal variance of the nth

time derivate, and the decadic logarithm of the temporal variance of the nth time derivate.

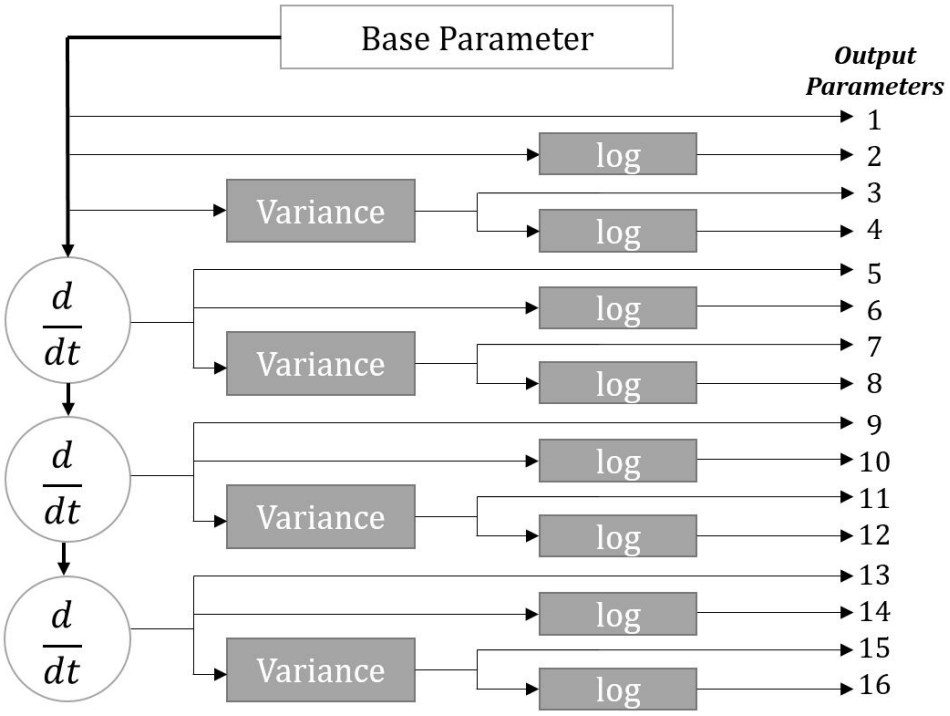

Figure 5.2: Flow chart of the systematic parameter evaluation, where there is a base data set (ARFI displacement, RF SNR, or CC) as an input, and 16 output parameters per base data set.

To understand the motivation for taking the time derivative, consider that this operation is a high pass filter that accentuates variance in the input data source. When the input data source is displacement, variance in the estimate, also known as "jitter", is predicted using the Cramer-Rao lower bound [102] as,

$$\sigma \geq \sqrt{\frac{3}{2f^3\pi^2T(B^3+12B)}\left[\frac{1}{CC^2}\left(1+\frac{1}{SNR^2}\right)^2-1\right]} \tag{5.1}$$

where f the center frequency, T is the tracking kernel size, and B is the bandwidth. If these three parameters are maintained constant, jitter magnitude is primarily a function of CC and SNR. Thus, by evaluating the time derivative(s) of displacement, signal components with different degrees of decorrelation and/or SNR level may be differentiated. On the contrary, considering CC or SNR alone differentiates signal components on the basis of only the single corresponding parameter. For

all three input data sources, temporal (unbiased) variance was calculated as,

$$V_p(x,y,t_i) = \frac{1}{k-1}\sum_{j=1}^{i+(k-1)}\left|p(x,y,t_j) - \frac{1}{k}\sum_{l=i}^{i+(k-1)} p(x,y,t_l)\right|^2 \tag{5.2}$$

where p is the input data source, x and y are the axial and lateral coordinates, respectively, and t is time. The window length for the variance calculation, k, was five time samples (corresponding to 0.5 ms for the employed pulse repetition frequency of 10 kHz). Using these operations, a total of 16 output parameters were generated for each input data source, for a total of 16 output parameters per input data source x 3 input data sources = 48 output parameters.

5.2.2 Image Rendering and Performance Analysis

For the *in vivo* human carotid plaque examples, parametric images of the 48 outcome parameters were rendered by displaying the median parameter value over the last two milliseconds of ensemble time for each pixel. For display and analysis purposes, all parametric images were normalized to the median value within the plaque +/− two Median Absolute Deviation (MAD).

From the parametric images, plaque components (COL, CAL, LRNC and IPH) were segmented using a semi-automatic k-means clustering method [103]. First, aligned histology and parametric images were cropped to span the ultrasonically interrogated plaque region. Then, from the cropped histology image, the centroids of the plaque features identified by the pathologist were calculated. Next, by resizing the image using bicubic interpolation (MATLAB, Mathworks Inc, Natick, MA, USA) , the number of lateral and axial pixels in the cropped histology image was matched to the number of lateral and axial pixels in the cropped parametric image. Finally, the centroid positions after resizing were input to the k-means algorithm as the starting locations for k regions to be segmented in the parametric image, where k is the number of plaque component regions identified by the pathologist.

For the segmented plaque features across all plaques, the values of each outcome parameter were statistically compared between plaque features using pairwise Wilcoxon rank sum tests with significance levels of 0.01 and 0.05. In addition, feature Contrast–to–Noise Ratio (CNR) was computed as,

$$CNR = \frac{|\mu_f - \mu_b|}{\sqrt{\sigma_f^2 + \sigma_b^2}} \tag{5.3}$$

where μ and σ are the mean and standard deviation within the segmented region, and the subscripts f and b refer to the feature and background regions, respectively. For the purposes of this study, IPH was a "feature" evaluated relative to LRNC "background", CAL was a "feature" evaluated relative to COL "background", and grouped soft plaque elements (LRNC and IPH) were a "feature" evaluated relative to grouped "stiff" plaque elements (CAL and COL) as the "background". Additionally, CNR coefficient of variation (CV) was calculated as σ_{CNR}/μ_{CNR}.

5.3 Results

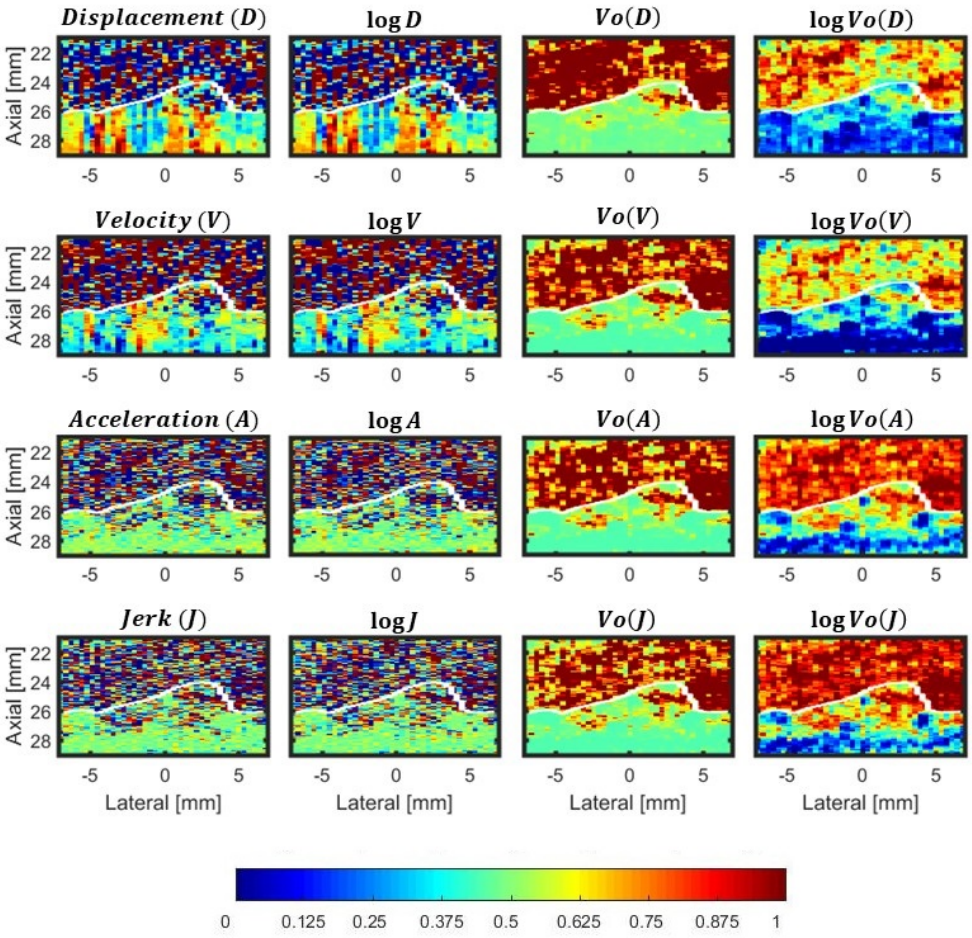

Figure 5.3: Parametric images of a carotid plaque from a 53-year-old symptomatic female. Base parameter: ARFI displacement. V_0 indicates variance calculation; log indicates decadic logarithm.

Figures 5.3, 5.4, and 5.5 show the 16 displacement-, SNR-, and CC-based parametric images, respectively, of an American Heart Association Type VI plaque [33] in the carotid artery of a

symptomatic 53-year-old female. In Figure 5.3, the time-derivative operation accentuates high-frequency jitter in the ARFI displacement profiles. Then, the accentuated jitter content is exploited using the variance calculation. The logarithmic representation of these results expands the dynamic range and improves contrast. Note that the first time-derivative of displacement is referred to as 'velocity', the second time-derivative as 'acceleration', and the third time-derivative as 'jerk'. The variance of the parameter is denoted 'Vo', and the decadic log is denoted 'log', such that log(VoA) is the decadic log of the variance of the second time-derivative of displacement.

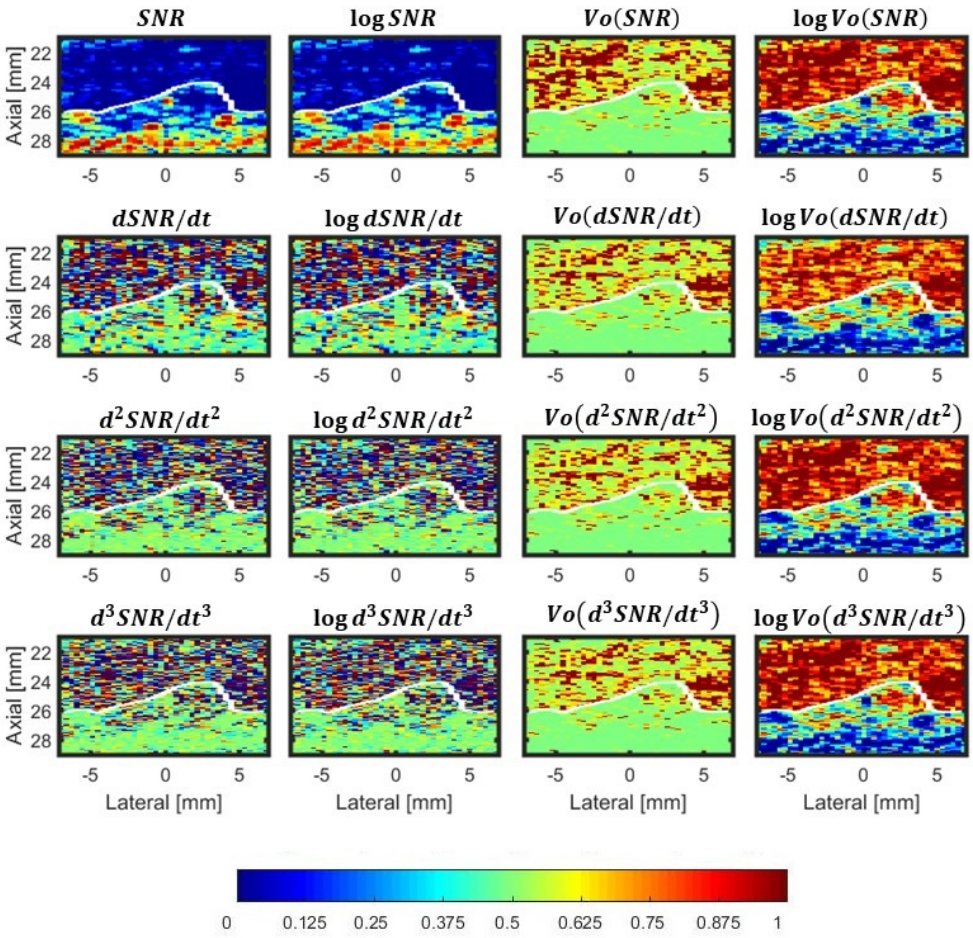

Figure 5.4: Parametric images of a carotid plaque from a 53-year-old symptomatic female. Base parameter: SNR. d^nSNR/dt^n indicates the n-th time derivative; V_0 indicates variance calculation; log indicates decadic logarithm.

Figures 5.6, 5.7, and 5.8 show distributions of outcome parameter values by plaque feature for all examined carotid plaques, as derived from ARFI displacement, SNR, and CC, respectively. Features

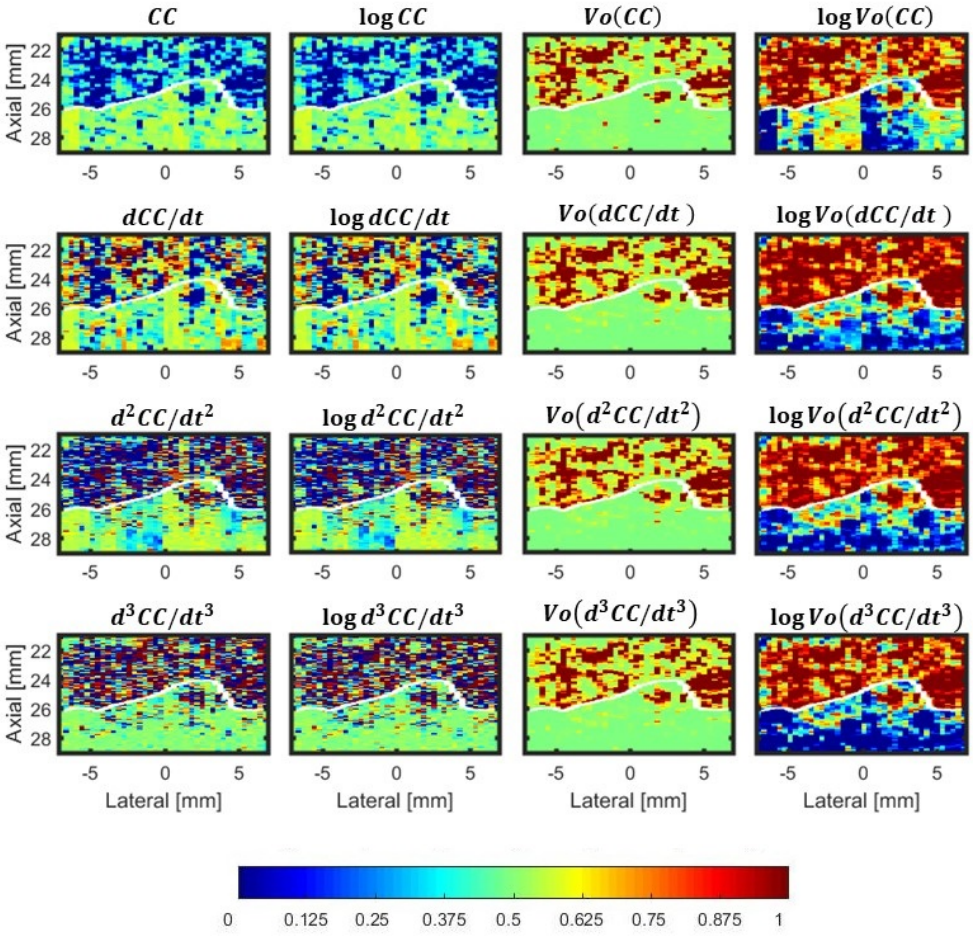

Figure 5.5: Parametric images of a carotid plaque from a 53-year-old symptomatic female. Base parameter: CC. d^nCC/dt^n indicates the n-th time derivative; V_0 indicates variance calculation; log indicates decadic logarithm.

with parameter distributions that statistically differ from each other ($p < 0.01$ or $p < 0.05$) are indicated by a black bar and asterisk or blue bar and circle, respectively, below the graph. From this analysis, the only parameter with statistically different distributions between CAL and COL, between COL and LRNC, and between LRNC and IPH was log(VoA). This parameter achieved the following normalized ranges for each component, expressed as median [Q1 Q3], where Q1 and Q3 are the 25th and 75th percentile values, respectively: IPH: 0.87 [0.76 1.00], LRNC: 0.56 [0.49 0.63], COL: 0.31 [0.27 0.43], CAL: 0.06 [0.02 0.17].

Additionally, feature CNR by parameter is indicated in Tables 5.1, 5.2, and 5.3 for ARFI displacement, SNR, and CC, respectively. The highest CNR value for each input data source is

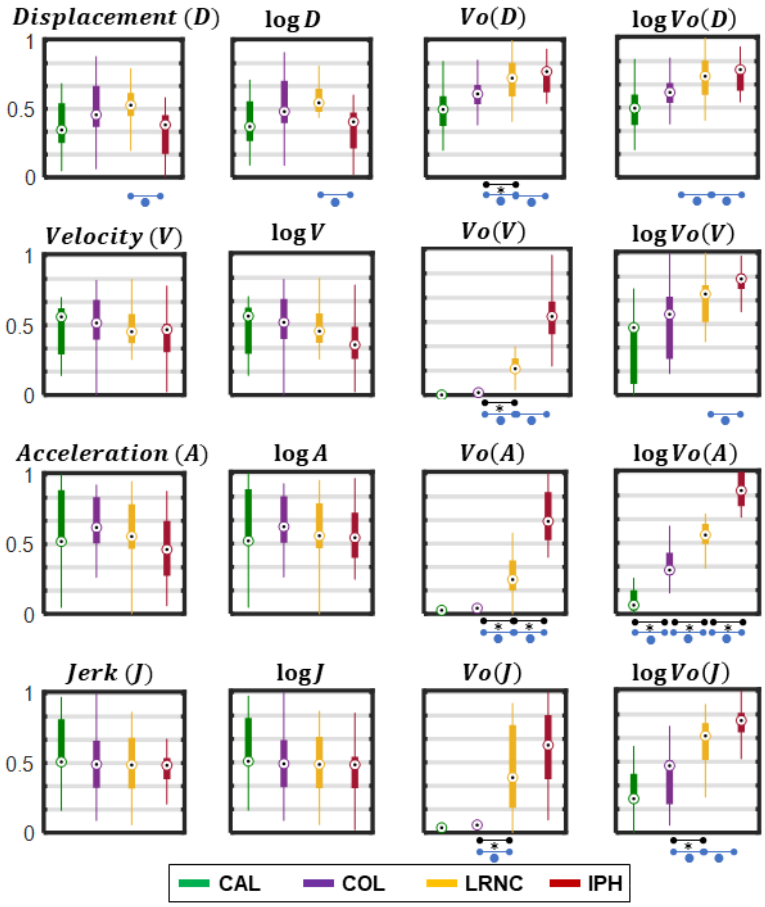

Figure 5.6: Normalized parameter value distributions by plaque feature for 20 carotid plaque examples. Distributions that are statistically different with $p < 0.01$ are indicated with a black asterisk, while distributions with $p < 0.05$ are indicated with a blue circle. Base parameter: ARFI displacement. V_0 indicates variance calculation; log indicates decadic logarithm.

shown in green, and the second highest is shown in yellow. CNR coefficient of variation is indicated parenthetically. The three best performing parameters were log(VoA), log(SNR), and Vo $\frac{dCC}{dt}$. The parameter log(VoA) yielded CNRs of 1.45 (0.61) for LRNC v. IPH, 2.30 (0.42) for COL v. CAL, 2.07 (0.49) for COL v. LRNC, and 3.09 (0.31) for soft v. stiff tissues. The parameter log(SNR) achieved CNRs of 0.71 (0.75) for LRNC v. IPH, 1.35 (0.62) for COL v. CAL, 0.79 (0.73) for COL v. LRNC, 1.52 (0.54) for soft v. stiff tissues. The parameter Vo $\frac{dCC}{dt}$ yielded CNRs of 1.40 (0.67) for LRNC v. IPH, 0.80 (0.89) for COL v. CAL, 0.73 (0.78) for COL v. LRNC, and 1.50 (0.61) for soft v. stiff tissues. For comparison purposes, CNR values from ARFI PD were also calculated: 0.40 (0.78) for LRNC v. IPH, 0.77 (1.04) for COL v. CAL, 0.28 (0.89) for COL v. LRNC, and 1.92 (0.28) for soft v. stiff tissues. From these results, the highest CNR for all plaque features was achieved by

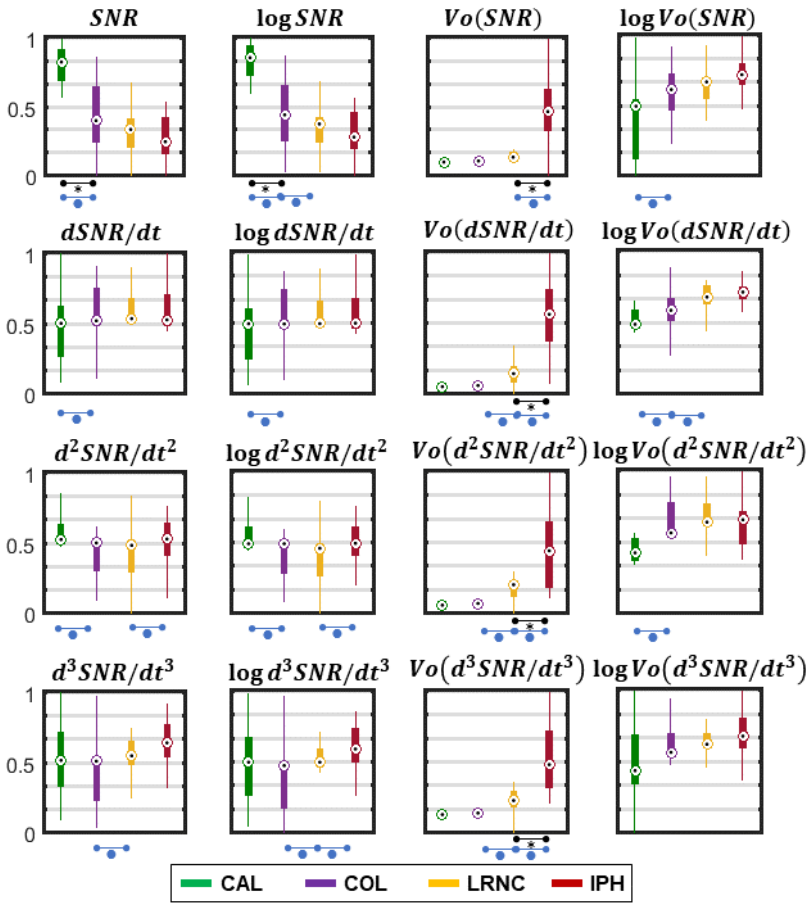

Figure 5.7: Normalized parameter value distributions by plaque feature for 20 carotid plaque examples. Distributions that are statistically different with p $<$ 0.01 are indicated with a black asterisk, while distributions with p $<$ 0.05 are indicated in blue. Base parameter: SNR. d^nSNR/dt^n indicates the n-th time derivative; V_0 indicates variance calculation; log indicates decadic logarithm.

log(VoA), followed by Vo $\frac{dCC}{dt}$ for LRNC v. IPH, and log(SNR) for COL v. CAL. ARFI PD yielded the second highest CNR for grouped soft v. stiff tissues.

Table 5.4 shows p-values for statistical comparisons between outcome parameter values in the specified plaque features. The outcome parameters are those with the highest overall CNR for each input data source, and PD is included for comparison purposes. The only parameter with statistically different (p $<$ 0.01) distributions between all the specified features is log(VoA). In contrast, ARFI PD values in regions of LRNC and IPH were not statistically different, and neither were ARFI PD values in regions of COL and CAL. The p-value describing the likelihood that grouped soft and grouped stiff plaque features had ARFI PD values that were the same was 0.02. Consistent with CNR results, log(SNR) values in regions of COL and CAL were statistically different (p $<$ 0.01),

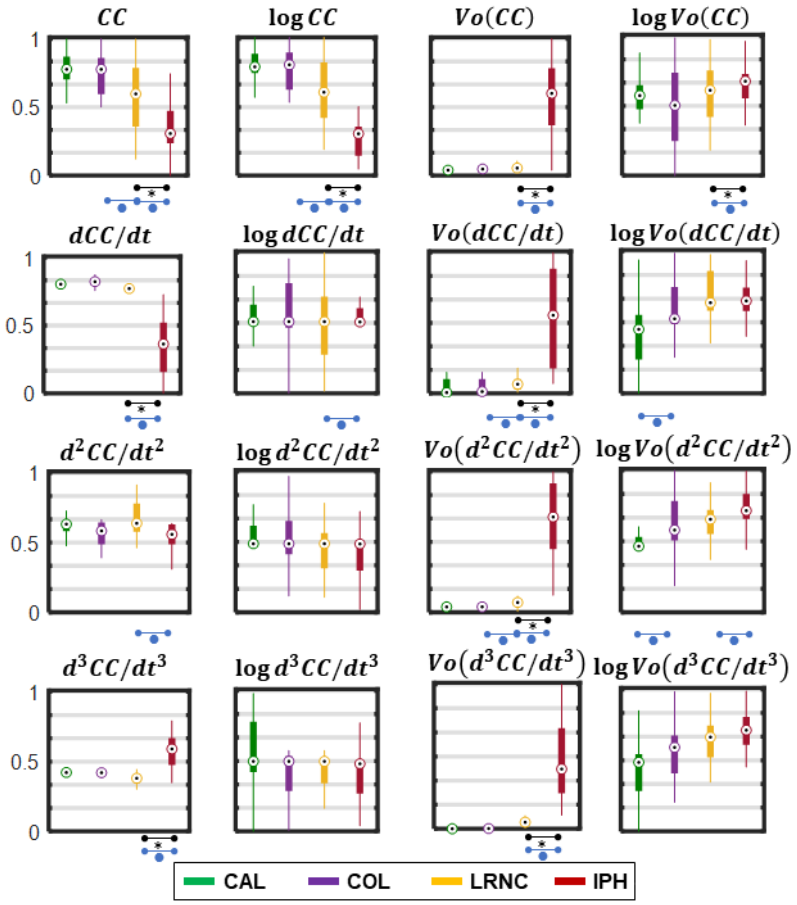

Figure 5.8: Normalized parameter value distributions by plaque feature for 20 carotid plaque examples. Distributions that are statistically different with $p < 0.01$ are indicated with a black asterisk, while distributions with $p < 0.05$ are indicated in blue. Base parameter: CC. d^nCC/dt^n indicates the n-th time derivative; V_0 indicates variance calculation; log indicates decadic logarithm.

and Vo $\frac{dCC}{dt}$ values statistically differed in regions of LRNC and IPH ($p < 0.01$).

For the same Type VI plaque of Figures 5.3 - 5.5, Figure 5.9 illustrates B-Mode, PD, and log(VoA) images. The images are shown with and without segmented plaque components to illustrate both the raw imaging results and segmentation outputs. Histology is also shown, spatially-matched to the ARFI imaging plane and stained with combined Masson's elastin (CME), Haemotoxylin and Eosin (H&E), and von Kossa (VK). Pathologist markings on the histology images indicate regions of COL, CAL, LRNC and IPH. In the PD image, CAL deposits (which are readily apparent as hyperechoic regions in the B-Mode image) exhibit similar PD as regions of COL. Further, PD achieved in small regions of LRNC are not distinguishable from those measured in the surrounding COL. Additionally, PDs in the region of IPH are high relative to the other plaque regions, but it

Feature Differentiation	CNR															
	Displacement (D)		logD		Vo(D)		logVo(D)		Velocity (V)		logV		Vo(V)		logVo(V)	
LRNC v. IPH	0.90	(0.89)	0.91	(0.88)	1.12	(0.74)	0.88	(0.85)	0.77	(0.84)	0.82	(0.93)	1.13	(0.81)	1.14	(0.73)
COL v. CAL	0.76	(0.79)	0.77	(0.80)	1.54	(0.64)	0.74	(0.94)	0.88	(0.55)	0.88	(0.55)	2.12	(0.46)	0.93	(0.42)
COL v. LRNC	0.62	(1.14)	0.62	(1.16)	1.54	(0.63)	0.82	(0.92)	0.82	(0.56)	0.82	(0.56)	1.44	(0.65)	1.25	(0.49)
Soft v. Stiff	0.85	(0.84)	0.85	(0.84)	2.61	(0.37)	1.18	(0.40)	0.86	(0.62)	0.79	(0.80)	3.02	(0.32)	2.27	(0.35)
	Acceleration (A)		logA		Vo(A)		logVo(A)		Jerk (J)		logJ		Vo(J)		logVo(J)	
LRNC v. IPH	0.69	(0.91)	0.89	(0.80)	0.75	(0.70)	1.45	(0.61)	0.71	(1.15)	0.5	(1.22)	0.85	(0.71)	0.97	(0.85)
COL v. CAL	0.83	(0.87)	0.83	(0.87)	1.13	(0.55)	2.3	(0.42)	0.37	(1.57)	0.37	(1.57)	2.03	(0.48)	0.93	(0.74)
COL v. LRNC	0.91	(0.75)	0.91	(0.75)	0.85	(1.29)	2.07	(0.49)	0.61	(1.04)	0.61	(1.04)	1.25	(0.76)	1.03	(0.57)
Soft v. Stiff	0.80	(0.98)	0.69	(0.93)	1.75	(0.47)	3.09	(0.31)	0.79	(0.95)	0.78	(0.94)	2.24	(0.44)	2.28	(0.31)

Table 5.1: Plaque feature CNR for ARFI displacement-derived parameters. CNR coefficients of variation are indicated between parentheses. V_0 indicates variance calculation; log indicates decadic logarithm.

Feature Differentiation	CNR															
	Displacement (D)		logD		Vo(D)		logVo(D)		Velocity (V)		logV		Vo(V)		logVo(V)	
LRNC v. IPH	0.7	(0.81)	0.71	(0.75)	0.41	(2.18)	0.60	(1.19)	0.54	(1.71)	0.53	(1.74)	0.51	(1.71)	0.59	(1.34)
COL v. CAL	1.29	(0.66)	1.35	(0.62)	1.00	(0.98)	0.76	(0.91)	0.5	(1.21)	0.49	(1.28)	0.56	(1.66)	0.66	(0.92)
COL v. LRNC	0.79	(0.74)	0.79	(0.73)	0.08	(12.27)	0.75	(0.85)	0.72	(1.15)	0.71	(1.17)	0.62	(1.39)	0.71	(0.97)
Soft v. Stiff	1.5	(0.55)	1.52	(0.54)	0.7	(1.29)	0.94	(0.76)	0.72	(1.04)	0.71	(1.08)	1.07	(0.90)	1.01	(0.66)
	Acceleration (A)		logA		Vo(A)		logVo(A)		Jerk (J)		logJ		Vo(J)		logVo(J)	
LRNC v. IPH	0.65	(1.15)	0.63	(1.20)	0.61	(1.38)	0.65	(0.81)	0.71	(0.97)	0.68	(1.04)	0.53	(1.45)	0.55	(1.08)
COL v. CAL	0.69	(0.96)	0.67	(1.04)	0.74	(1.30)	0.76	(0.77)	0.8	(1.04)	0.77	(1.10)	0.42	(2.33)	0.48	(1.10)
COL v. LRNC	0.65	(1.17)	0.64	(1.24)	0.79	(1.11)	0.67	(0.99)	0.72	(1.35)	0.7	(1.39)	0.52	(1.61)	0.46	(1.67)
Soft v. Stiff	0.89	(0.97)	0.89	(0.98)	0.7	(1.39)	1.09	(0.61)	0.69	(1.20)	0.67	(1.30)	0.54	(1.76)	0.5	(1.42)

Table 5.2: Plaque feature CNR for SNR-derived parameters. CNR coefficients of variation are indicated between parentheses. $d^n SNR/dt^n$ indicates the n-th time derivative; V_0 indicates variance calculation; log indicates decadic logarithm.

is difficult to determine if these high PDs indicate IPH or LRNC, resulting in underestimation of IPH regions. In the log(VoA) images, CAL deposits have noticeably lower log(VoA) than any other plaque features. Further, LRNC exhibits higher log(VoA) than COL. Finally, the regions of IPH have the highest overall log(VoA). These results show that, by visual inspection, CAL is better distinguished from COL and IPH is better distinguished from LRNC using log(VoA) than PD.

To further demonstrate the effectiveness of log(VoA) for delineating carotid plaque components, Figures 5.10 and 5.11 show additional examples of B-Mode, PD, and log(VoA) images with spatially matched histology. In Figure 5.10(b), CAL and LRNC exhibit PDs that are similar to those of collagen, while IPH exhibits high PDs that could be mistaken for LRNC. In the log(VoA) image of panel (c), CAL and LRNC are distinguishable from COL, and log(VoA) values in regions of IPH are higher than those in LRNC. The segmented fibrous cap and IPH regions in the log(VoA) image

Feature Differentiation	CNR															
	Displacement (D)		logD		Vo(D)		logVo(D)		Velocity (V)		logV		Vo(V)		logVo(V)	
LRNC v. IPH	0.94	(0.73)	0.98	(0.87)	1.14	(0.83)	0.97	(0.55)	1.05	(0.91)	1.15	(0.55)	1.4	(0.67)	1.28	(0.57)
COL v. CAL	0.52	(1.02)	0.55	(0.91)	0.72	(1.09)	0.73	(1.03)	0.64	(1.08)	0.78	(0.97)	0.8	(0.89)	0.79	(1.02)
COL v. LRNC	0.64	(0.90)	0.64	(0.87)	0.58	(0.63)	0.66	(1.03)	0.7	(1.03)	0.51	(1.22)	0.73	(0.78)	0.72	(1.01)
Soft v. Stiff	1.14	(0.67)	1.14	(0.68)	1.06	(0.92)	0.89	(0.74)	1.1	(0.81)	1.15	(0.58)	1.5	(0.61)	0.91	(0.78)
	Acceleration (A)		logA		Vo(A)		logVo(A)		Jerk (J)		logJ		Vo(J)		logVo(J)	
LRNC v. IPH	1.01	(0.75)	1.04	(0.71)	1.03	(0.91)	1.07	(0.61)	0.62	(1.04)	0.7	(1.10)	0.78	(1.24)	0.54	(1.29)
COL v. CAL	0.77	(0.84)	0.52	(1.20)	0.76	(0.89)	0.74	(0.70)	0.61	(1.38)	0.67	(1.25)	0.58	(1.69)	0.63	(0.83)
COL v. LRNC	0.62	(0.90)	0.69	(1.07)	0.72	(0.81)	0.69	(1.06)	0.7	(1.25)	0.65	(1.14)	0.48	(2.03)	0.64	(1.06)
Soft v. Stiff	0.74	(1.00)	0.69	(1.26)	1.05	(0.92)	1	(0.76)	0.59	(0.97)	0.71	(1.09)	0.89	(1.09)	0.86	(0.98)

Table 5.3: Plaque feature CNR for SNR-derived parameters. CNR coefficients of variation are indicated between parentheses. d^nSNR/dt^n indicates the n-th time derivative; V_0 indicates variance calculation; log indicates decadic logarithm.

Feature Differentiation	CNR				N
	logVo(A)	PD	logSNR	Vo(dCC/dt)	
LRNC v. IPH	$<$**0.01**	0.58	0.62	$<$**0.01**	14
COL v. CAL	$<$**0.01**	0.19	$<$**0.01**	0.31	19
COL v. LRNC	$<$**0.01**	1.02	0.11	0.53	18
Soft v. Stiff	$<$**0.01**	0.02	0.05	0.03	20

Table 5.4: Statistical significance of the differences between LRNC and IPH, between COL and CAL, and between grouped soft (LRNC/IPH) and stiff (COL/CAL) features for log(VoA), PD, CC, and SNR derived optimal parameters. d^nSNR/dt^n indicates the n-th time derivative; V_0 indicates variance calculation; log indicates decadic logarithm.

more closely match the spatial distribution of these plaque components in the matched histology. In Figure 5.11(b), high PD values are associated with a large region of CAL (black arrows), which is inconsistent with the expected low displacement response of stiff CAL. These high PD values, which arise from displacement profile distortions caused by wave reflections [104], erroneously indicate a large, soft feature. While this large CAL region is mischaracterized as a soft feature in the PD image, it is appropriately indicated as a region of low log(VoA) in panel (c), consistent with the expected response of CAL. Other features, including regions of COL and LRNC are also delineated in the log(VoA) image.

5.4 Discussion

The results presented in this chapter demonstrate that the outcome metric calculated as the decadic logarithm of the variance of acceleration, or log(VoA), better discriminates carotid plaque features that confer risk for stroke than ARFI PD. Further, the results suggest that by incorporating

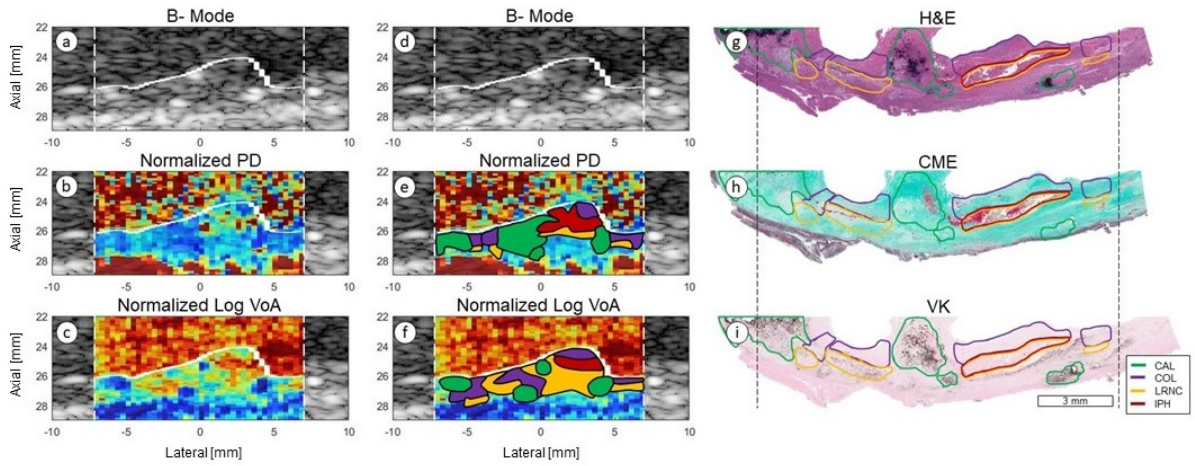

Figure 5.9: Carotid ARFI images with matched histology from a 53-year-old symptomatic female. First and second columns show: B-mode, normalized ARFI PD image, and normalized ARFI log(VoA) image, without (a, b, c) and with (d, e, f) component segmentations. Third columns show histological results of (g) H&E, (h) CME and (i) VK stains, confirming the presence of CAL, COL, LRNC, and IPH plaque features. Features are denoted by color as CAL (green), COL (purple), LRNC (yellow), and IPH (red)

both CC and SNR, which are respectively related to the displacement and echogenicity of plaque components, log(VoA) achieves improved delineation of plaque composition and structure over analysis of CC or SNR alone.

Variations in CC may be caused by mechanical property differences among plaque components that yield diverse viscoelastic recoveries after the ARFI excitation. For example, IPH scatterers may exhibit no or very slow elastic recovery after the ARFI excitation. Thus, IPH scatterers may remain in motion after scatterers in the other plaque components have recovered, resulting in less correlated signal from regions of IPH than from other plaque regions. In regard to SNR, more highly echogenic plaque features, such as CAL deposits, have lower jitter magnitude, and thereby lower log(VoA), than plaque components that are less echogenic.

Plaque feature delineation performance by log(VoA) and by parameters derived from CC alone and SNR alone is compared by analyzing CNR in Tables 5.1-5.3 and parametric value distributions in Figures 6-8. As expected, CC-derived values in IPH are generally lower than those in LRNC, but CC alone does not differentiate CAL from COL. Applying high-pass filtering by using the time-derivative operation and calculating the variance (as is performed for log(VoA) calculation) subtly improves separation of plaque features by COL, but LRNC and IPH are not differentiated by SNR alone.

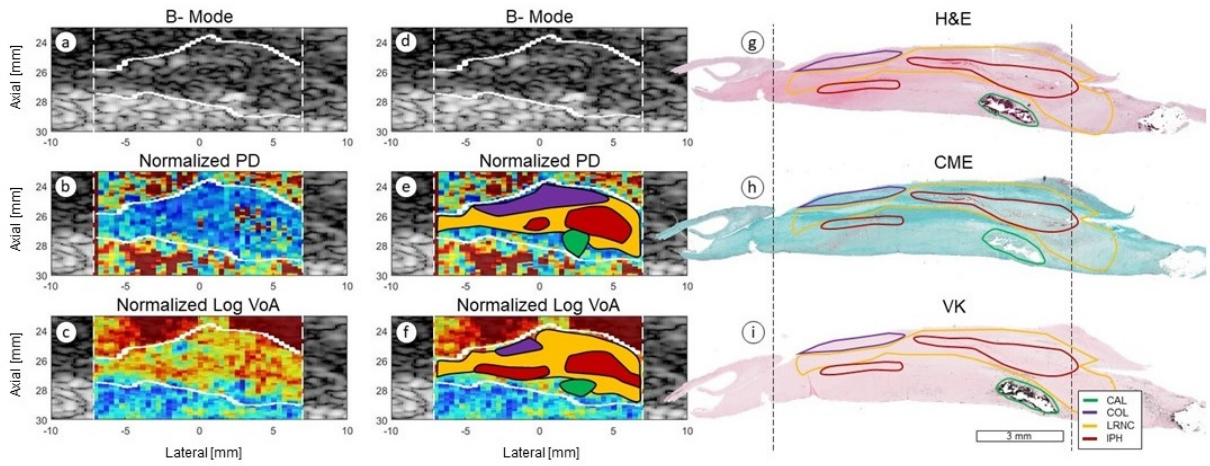

Figure 5.10: Carotid ARFI images with matched histology from a 59-year-old symptomatic male. First and second columns show: B-mode, normalized ARFI PD image, and normalized ARFI log(VoA) image, without (a, b, c) and with (d, e, f) component segmentations. Third columns show histological results of (g) H&E, (h) CME and (i) VK stains, confirming the presence of CAL, COL, LRNC, and IPH plaque features. Features are denoted by color as CAL (green), COL (purple), LRNC (yellow), and IPH (red)

The potential for visually discriminating LRNC from IPH and COL from CAL using optimized parameters derived by CC alone or SNR alone is explored in Figures 5.4 and 5.5. In Figure 5.4, regions of high SNR in the normalized image correspond to focal calcium deposits, and in Figure 5.5, a region of low CC in the normalized image corresponds to IPH. While IPH is indicated in the CC images, no other plaque features are readily discernible. Furthermore, while CAL deposits are obvious in the SNR images, no other plaque features are apparent. Taken together, by visual inspection and CNR comparison, the evaluated data suggest that by incorporating both CC and SNR into a single metric, log(VoA) achieves more complete separation of plaque components than either CC or SNR alone.

In this work, log(VoA) was calculated as the decadic log of the variance of the second time-derivative of ARFI-induced displacement to exploit jitter magnitude. We note that other approaches to isolating jitter in displacement estimates are also possible, including frequency-domain filtering and mathematical calculations. Such alternative approaches are currently under investigation.

Previous studies have shown that ARFI is safe for carotid plaque imaging [36, 105]. Doherty et al. [106] showed that the magnitude of von Mises stress associated with ARFI excitations in arterial plaques (< 1.2 kPa) is two orders of magnitude lower than the average arterial pressure

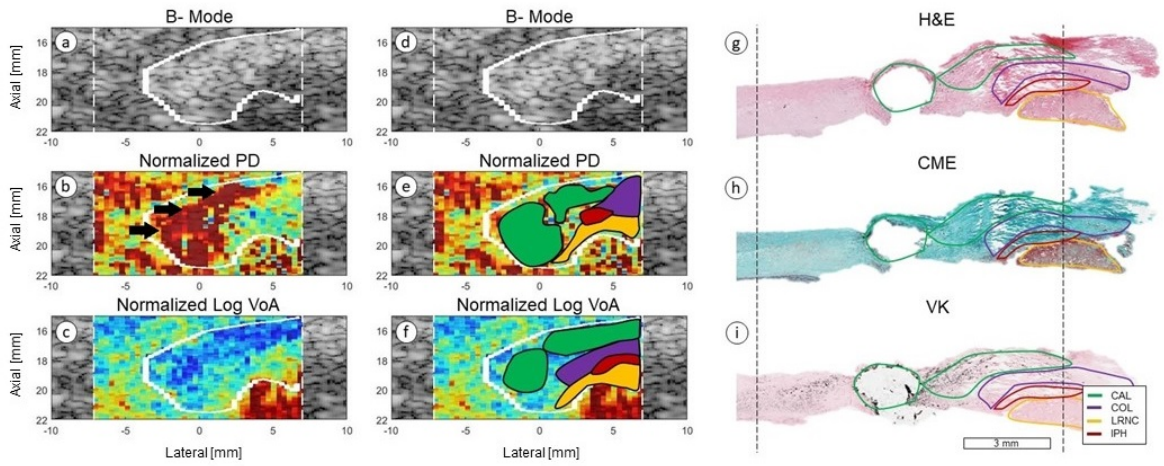

Figure 5.11: Carotid ARFI images with matched histology from a 57-year-old symptomatic male. First and second columns show: B-mode, normalized ARFI PD image, and normalized ARFI log(VoA) image, without (a, b, c) and with (d, e, f) component segmentations. Third columns show histological results of (g) H&E, (h) CME and (i) VK stains, confirming the presence of CAL, COL, LRNC, and IPH plaque features. Features are denoted by color as CAL (green), COL (purple), LRNC (yellow), and IPH (red). Black arrows show PD misrepresentation of CAL due to artifacts caused by plaque interaction with the proximal wall.

stresses associated with ruptured (545.3 kPa) and unruptured (192.5 kPa) arterial plaque [36, 105]. Additionally, results reported herein agree with other work that histologically validated *in vivo*, noninvasive human carotid plaque component delineation by mechanical property. Like log(VoA), CUSI detected lipid regions, which differentiated fibrous from (fibro)atheromatous plaques [107, 108].

A limitation in the presented study design is that the examined *in vivo* human carotid plaque data were originally acquired for the purpose of evaluating ARFI PD. As a result, all acquisitions were gated to diastole, and the tracking ensemble time was limited to 5 ms. Therefore, it was not possible to thoroughly evaluate the impact of different degrees of arterial pressure/distention on log(VoA), and times longer than 5 ms after the ARFI excitation could not be examined. Future work will explore these variables.

A second limitation was the unequal number of plaque component examples, as indicated in Table 5.4, which impacted the pairwise Wilcoxon rank sum tests by diminishing the statistical power as the number of components become more unequal. More instances of statistically significant differences in parameter value and/or CNR may have been observed if the number of plaque component examples was equal.

Another limitation of this study is the impact of sample deformations on the spatial correlation between histology and ARFI images. Even though the plaque specimens were removed en bloc and immediately transferred to formalin solution, distortions still occurred. The primary causes of distortion were surgical extraction, fixation, and lack of pressurization, the latter two of which caused changes in tissue size. Despite these limitations, using μCT volumes of the extracted specimens enabled alignment of histology and ARFI imaging planes. Finally, an important consideration is the possibility of calcium deposits acting as local stress concentrators, which could confound ARFI-derived results.

While this work suggests that opportunities for log(VoA) to improve stroke risk prediction by delineating the structure and composition of carotid plaques are great, a potential challenge to optimal clinical application could be spatial resolution. For example, Czernuszewicz and Gallippi previously demonstrated in silico that fibrous cap thickness resolution by ARFI PD is 0.2 mm [109]- the upper limit on the critical fibrous cap thickness for predicting rupture [110] - when a 12 MHz center frequency is used. While the contrast mechanisms in ARFI PD and log(VoA) images differ, the prior work supports that higher center frequencies could improve feature size resolution by log(VoA). However, increasing the center frequency will decrease jitter magnitude, which could degrade log(VoA) feature discrimination if CC and SNR are rendered less impactful on the overall jitter value. Increasing the center frequency will also reduce penetration depth. Czernuszewicz and Gallippi further demonstrated that decreasing the displacement tracking kernel length improves fibrous cap thickness resolution by ARFI PD. In log(VoA) estimation, decreasing the kernel length will increase jitter magnitude and, like increasing center frequency, could disrupt the influence of CC and SNR on the log(VoA) outcome parameter. Ultimately, identifying log(VoA) resolution limits and determining the ideal combination of imaging parameters for *in vivo* carotid plaque feature delineation will be important to realizing log(VoA)'s potential for improving stroke risk prediction clinically.

5.5 Conclusion

This chapter demonstrates the potential of the decadic logarithm of the variance of acceleration, or log(VoA), to improve *in vivo* carotid atherosclerotic plaque feature delineation relative to ARFI PD. Across all examined *in vivo* human carotid plaques, log(VoA) values were statistically significantly different between histologically confirmed regions of IPH and LRNC and between confirmed regions

of COL and CAL, but this was not true for PD. Moreover, log(VoA) achieved higher CNR between IPH and LRNC, between COL and CAL, and between COL and LRNC than PD. Finally, the presented results demonstrate that although log(VoA) is influenced by both CC and SNR, evaluating CC alone or SNR alone does not differentiate IPH, LRNC, COL, and CAL as well as log(VoA). Overall, these results support that log(VoA) is capable of describing the composition and structure of human carotid atherosclerotic plaque, *in vivo*, which is clinically useful for predicting stroke risk and facilitating medical management. In the following chapter, this analysis will be extended to the application of log(VoA) for fibrous cap thickness and component area measurement, through semi-automatic segmentation, blinded-readers, and automatic classification algorithms.

CHAPTER 6

ARFI DISPLACEMENT VARIANCE FOR FIBROUS CAP THICKNESS AND COMPONENT AREA MEASUREMENT

6.1 Introduction

In the previous chapter, ARFI log(VoA) was demonstrated for differentiating carotid plaque features with higher contrast performance than ARFI PD, cross-correlation coefficient, and SNR.

This chapter evaluates log(VoA) for measuring fibrous cap thickness and plaque component areas from 20 previously scanned samples using semi-automatic segmentation and histology as the gold standard. In [8], a likely cause of area measurement overestimation by ARFI PD assessment is improper delineation of the boundaries between different components, such as the lumen and the fibrous cap and between the fibrous cap and the underlying lipid-rich necrotic core (LRNC) or intraplaque hemorrhage (IPH). Therefore, a method for improving differentiation of fibrous cap boundaries could improve component area measurement to support more accurate carotid plaque risk assessment.

In this chapter [1], the hypothesis that, relative to ARFI PD, ARFI log(VoA) achieves better accuracy and precision of plaque component area and fibrous cap thickness measurement in human carotid plaque, *in vivo* is tested using semi-automatic segmentation of ARFI data previously acquired from patients undergoing clinically indicated carotid endarterectomy (CEA), with histological validation from [8]. Results indicate improved performance by both groups of readers when using log(VoA) for delineating CAL (AUC for PD: 0.631, VoA: 0.723), COL (AUC for PD: 0.581, VoA: 0.771), LRNC (AUC for PD: 0.715, VoA: 0.913), and IPH (AUC for PD: 0.589, VoA: 0.795), independently. Additionally, through a Bland-Altman plot, area measurements were improved when

[1]

using log(VoA) compared to PD for CAL (CV for PD: 110%, VoA: 55%), LRNC (CV for PD: 45%, VoA: 40%), and IPH (CV for PD: 120%, VoA: 36%), independently.

6.2 Methods

Patient recruitment and imaging protocol are described in detail on our prior work [8]. A total of 25 patients undergoing clinically indicated CEA were recruited from UNC Hospitals. Inclusion criteria included either asymptomatic carotid artery disease with >60% Doppler-indicated stenosis and unresponsive to medical management or symptomatic carotid artery disease with a stenosis suspected to be the source of emboli. All procedures were approved by the IRB, and informed written consent was given from each study participant.

A Siemens Acuson Antares research imaging system (Siemens Healthcare, Ultrasound Division) was used for *in vivo* imaging with a VF7-3 linear array transducer. After surgery, CEA specimens were harvested, μCT imaged (Scanco 40, Scanco Medical AG, Bassersdorf, Switzerland), and processed for spatially-matched histological validation. A more detailed description of the process for aligning ARFI and histology data is contained in Czernuszewicz et al [8].

The histology subsections were read by a pathologist with expertise in atherosclerosis, who hand-delineated fibrous caps using a custom graphical user interface (GUI) developed in Matlab (Mathworks Inc., Natick, MA, USA) for the previous blinded-reader study [8]. In the parametric ARFI image subsections, plaque components were segmented using a semiautomatic k-means clustering method [111, 103], detailed in the previous chapter. Centroids from each fibrous cap were calculated from the parametric images aligned with histology, and these centroids were input to the k-means algorithm for segmenting k regions, where k is the number of fibrous cap areas identified by the pathologist on each histology slide. [111].

Exclusion criteria were applied to the data collected from the 25 patients to ensure high-quality and well-matched histology and ARFI data. First, plaque specimens that were damaged or fractured during surgery were excluded. Second, plaques imaged with the lumen-plaque boundary outside the axial range of ARFI imaging (spanning $\pm$ 5 mm from the focal depth) were excluded. Third, carotid plaques without the presence of a fibrous cap in histology were excluded.

After data exclusions, 14 fibrous caps were retained for comparison of fibrous cap thickness measurement by ARFI PD and log(VoA) parameters. log(VoA) was calculated as the unbiased

variance of the second time derivative through the total ensemble time per pixel:

$$VoA(x,y,t_i) = \frac{1}{k-1} \sum_{j=1}^{i+(k-1)} \left| Acc(x,y,t_j) - \mu_{Acc}(x,y,t_i) \right|^2 \tag{6.1}$$

where x and y are axial and lateral pixel coordinates, respectively, t is ensemble time, k is the total number of ensemble time samples, Acc is acceleration, and μ_{Acc} is the mean of Acc.

ARFI PD and VoA outcomes were rendered into two-dimensional parametric images, with VoA depicted as its decadic logarithm, denoted log(VoA), to increase dynamic range. For display purposes, both PD and log(VoA) images were normalized to the mean value within the plaque ± two median absolute deviations (MAD). The linear relationship between histology-derived fibrous cap thickness measurements and imaging-derived thickness from PD and log(VoA) images were visually assessed in scatterplots and tested by Pearson correlation. Bland-Altman analysis was performed to evaluate the agreement between fibrous cap thicknesses derived from ARFI and histology. Finally, the concordance correlation coefficient (CCC), a measure of both the precision and accuracy of imaging-derived thickness compared to histology-derived thickness, was calculated for both ARFI PD and ARFI log(VoA), with the CCC closest to 1 considered to be the most accurate and precise measurement [112]. All statistical analyses were performed using Matlab (Mathworks Inc., Natick, MA, USA).

6.3 Results

For a representative plaque from a 53 year-old symptomatic female, B-Mode, ARFI PD, and ARFI log(VoA) images are shown in Figure 6.1, without (left column) and with (right column) the automatically segmented fibrous cap regions shown in white. The fibrous cap thicknesses derived from the segmented regions in PD and log(VoA) images were 0.93 and 0.90 mm, respectively, while the thickness of the fibrous cap hand-delineated by the pathologist was 0.84 mm. For reference, the plaque boundary hand-delineated from ARFI PD images by the best-performing reader in [8] is shown in black.

Figure 6.2 shows another carotid plaque example from a symptomatic 45-year-old female. Again, the automatically segmented fibrous caps are shown in white in the right column. These segmentations yielded fibrous cap thickness measures of 0.99 and 0.90 mm for ARFI PD and log(VoA), respectively, while the histology-derived thickness was 0.91 mm.

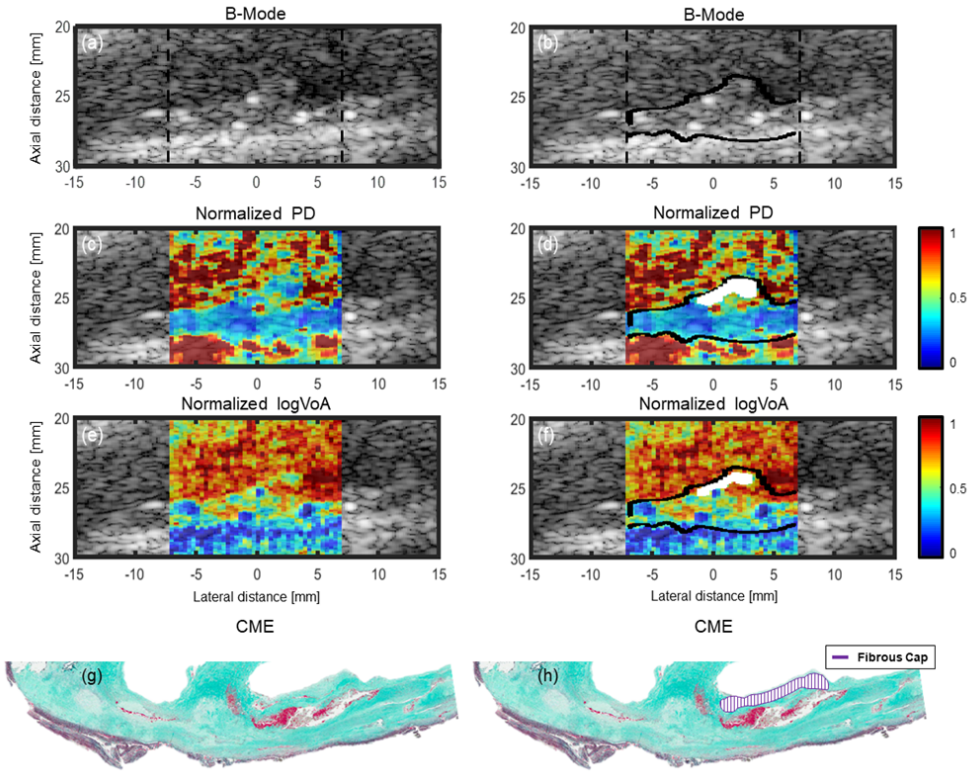

Figure 6.1: Carotid plaque ARFI images with matched histology in a symptomatic 53-year-old female. From top to bottom: B-mode (a, b), normalized ARFI PD image (c, d), and normalized ARFI log(VoA) image, (e, f), and CME stains (g, h). In (b), (d), and (f), the plaque boundary hand-delineated from ARFI PD images by the best performing reader in [25] is shown in black, and the fibrous caps automatically segmented from PD and log(VoA) images are shown in white. In (h), the fibrous cap outline hand-delineated by the pathologist is shown.

Figure 6.3 shows a third plaque example from a symptomatic 59-year-old male. In this case, the fibrous cap thicknesses derived from automatic segmentation of PD and log(VoA) images were 1.40 and 1.35 mm, respectively, while the fibrous cap thickness measured from the spatially matched histology was 1.26 mm.

Figure 6.4 illustrates median ARFI PD (a) and log(VoA) (b) fibrous cap thickness measurements plotted versus the histological validation standard for the evaluated plaques. It can be observed that median PD-derived fibrous cap thickness measurements correlated more weakly with the validation standard than corresponding log(VoA) measures. The (R2, sum squared error (SSE)) values were (0.79, 0.19) for PD and (0.97, 0.03) for log(VoA). The concordance correlation coefficient (CCC) was 0.62 for PD and 0.95 for log(VoA), which indicates more precision and agreement between log(VoA) and histology than PD and histology. Additionally, the correlation between histology with PD was

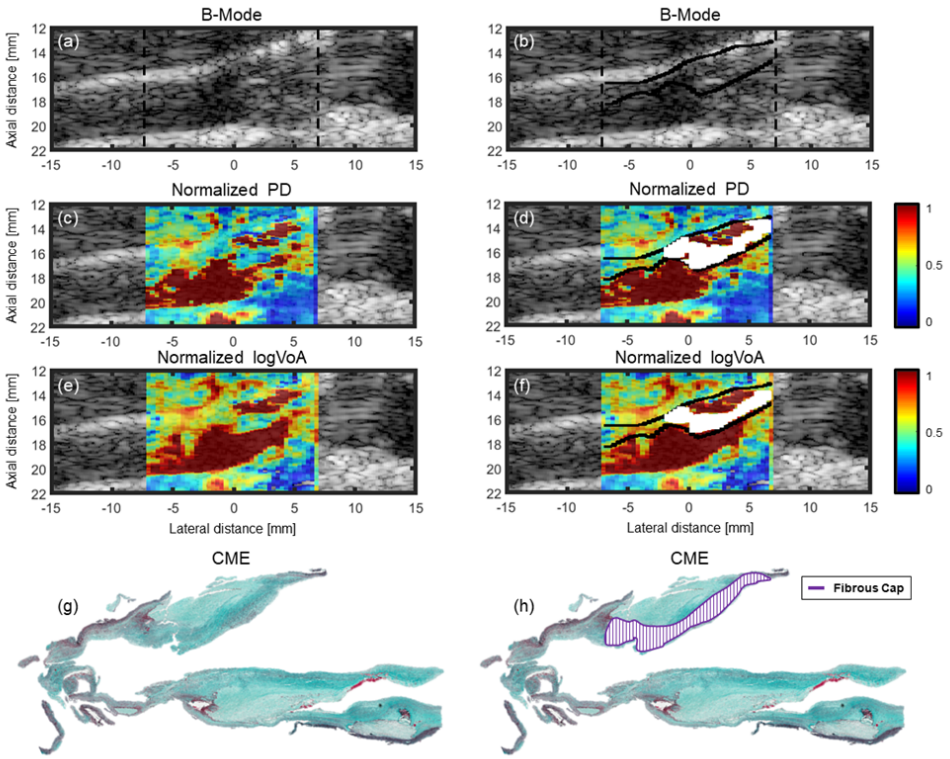

Figure 6.2: Carotid plaque ARFI images with matched histology in a symptomatic 45-year-old female. From top to bottom: B-mode (a, b), normalized ARFI PD image (c, d), and normalized ARFI log(VoA) image (e, f), and CME stains (g, h). In (b), (d), and (f), the plaque boundary hand-delineated from ARFI PD images by the best performing reader in [25] is shown in black, and the fibrous caps automatically segmented from PD and log(VoA) images are shown in white. In (h), the fibrous cap outline hand-delineated by the pathologist is shown.

0.88 (95% CI: 0.38 to 0.90; P = 0.001), while the correlation with log(VoA) was stronger, at 0.98 (95% CI: 0.94 to 0.99, P<0.0001). In figure 6.5, Bland-Altman results indicate that the coefficient of variation was 16% for PD-derived median fibrous cap thickness versus 6.3% for log(VoA)-derived median fibrous cap thickness. The bias in PD-derived median fibrous cap thickness, 0.10 mm, was statistically significant, while the 0.05 mm bias in log(VoA)-derived median fibrous cap thickness was not statistically significant (p<0.05).

Figure 6.6 illustrates minimum (a) PD and (b) log(VoA) fibrous cap thickness measurements plotted versus the histological validation standard. The (R2, SSE) values were (0.74, 0.22) for PD and (0.95, 0.05) for log(VoA). The concordance correlation coefficient (CCC) was 0.61 for PD and 0.87 for log(VoA). Figure 6.7 shows Bland-Altman results for the minimum fibrous cap thickness measurements. The coefficient of variation for minimum fibrous cap thickness measurement was 20%

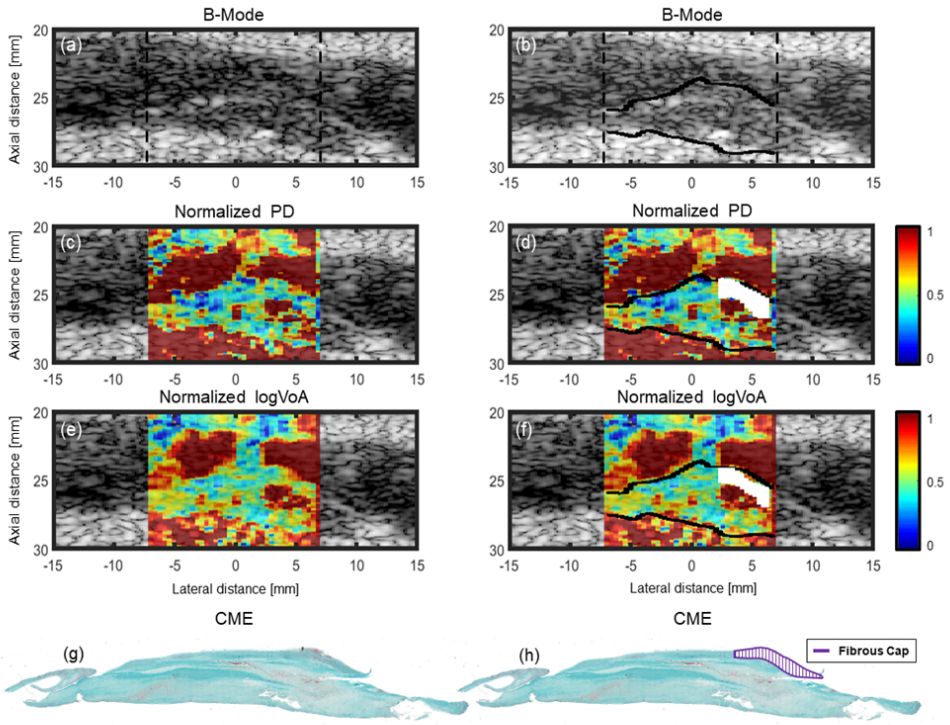

Figure 6.3: Carotid plaque ARFI images with matched histology in a symptomatic 59-year-old male. From top to bottom: B-mode (a, b), normalized ARFI PD image (c, d), and normalized ARFI log(VoA) image (e, f), and CME stains (g, h). In (b), (d), and (f), the plaque boundary hand-delineated from ARFI PD images by the best performing reader in [25] is shown in black, and the fibrous caps automatically segmented from PD and log(VoA) images are shown in white. In (h), the fibrous cap outline hand-delineated by the pathologist is shown.

for PD versus 8.6% for log(VoA).

Figure 6.8 illustrates maximum (a) PD (a) and (b) log(VoA) fibrous cap thickness measurements plotted versus the histological validation standard. For the maximum fibrous cap thickness measurements, the (R2, SSE) values were (0.67, 0.35) for PD and (0.84, 0.23) for log(VoA). The concordance correlation coefficient (CCC) was 0.55 for PD and 0.89 for log(VoA). Figure 6.9 shows Bland-Altman results for maximum fibrous cap thickness measurements. The coefficient of variation for maximum fibrous cap thickness measurement was 21% for PD versus 16% for log(VoA).

The axial locations of PD- and log(VoA)-derived lumen-cap and cap-LRNC boundaries were compared. The median difference in PD - log(VoA) lumen-cap boundary position was -0.33 $\pm$ 0.21 mm. The median difference in PD - log(VoA) cap-LRNC boundary position was +0.21 $\pm$ 0.10 mm.

ARFI-derived component areas were also compared between ARFI PD and log(VoA). Figures

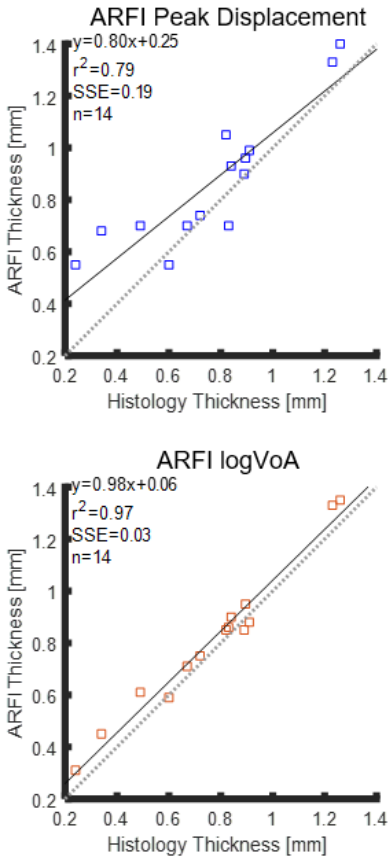

Figure 6.4: Linear regressions of ARFI PD- (top) and log(VoA)- (bottom) derived median fibrous cap thicknesses versus median histological standard over fourteen human carotid plaques, in vivo (black lines). Median values per plaque are shown as circular scatters. R^2: coefficient of determination. SSE: Sum of squared error.

6.10, 6.11, and 6.12 show Bland-Altman plots comparing ARFI PD and log(VoA)-derived areas for CAL, LRNC, and IPH. For measuring the area of calcium, PD achieves a Reproducibility Coefficient (RPC) of 3.5 and a Coefficient of Variation (CV) of 110% whereas log(VoA) achieves a RPC of 1.1 and a CV of 55%. For measuring the area of lipid-rich necrotic core, PD achieves a RPC of 6.9 and a CV of 45% whereas log(VoA) achieves a RPC of 4.7 and a CV of 40%. For measuring the area of intraplaque hemorrhage, PD achieves a RPC of 29 and a CV of 120% whereas log(VoA) achieves a RPC of 6.0 and a CV of 36%.

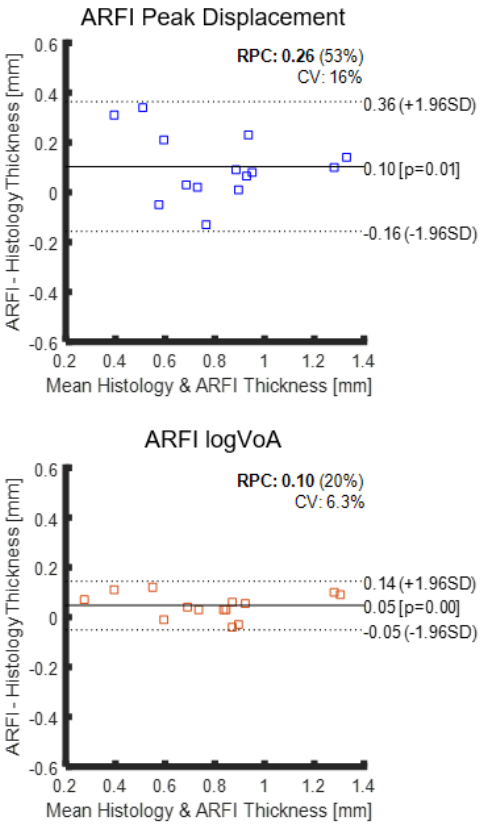

Figure 6.5: Bland-Altman plots assessing the reproducibility of median plaque thickness results derived from ARFI PD (top) and ARFI logVoA (bottom). RPC: Reproducibility coefficient, CV: Coefficient of variation.

6.4 Discussion

In Figure 6.1, the boundary using the ARFI PD image yields a median fibrous cap thickness measurement that is 10.71% larger than the histological validation standard, while the thickness derived using log(VoA) is 7.14% larger. These data, suggesting that median fibrous cap thickness measurement by log(VoA) is in better agreement with the histological validation standard than that by PD, are consistent with the results observed in Figure 6.2 (relative to histology, 8.79% larger median fibrous cap thickness by PD versus 1.10% larger by logVoA) and Figure 6.3 (relative to histology, 11.11% larger median fibrous cap thickness by PD versus 7.14% larger by logVoA). Over these plaques, median fibrous cap thickness measured by PD had an absolute difference of 0.10 $\pm$ 0.26 mm compared to histology, whereas fibrous cap thickness measured by log(VoA) had an absolute difference of 0.05 $\pm$ 0.09 mm compared to histology.

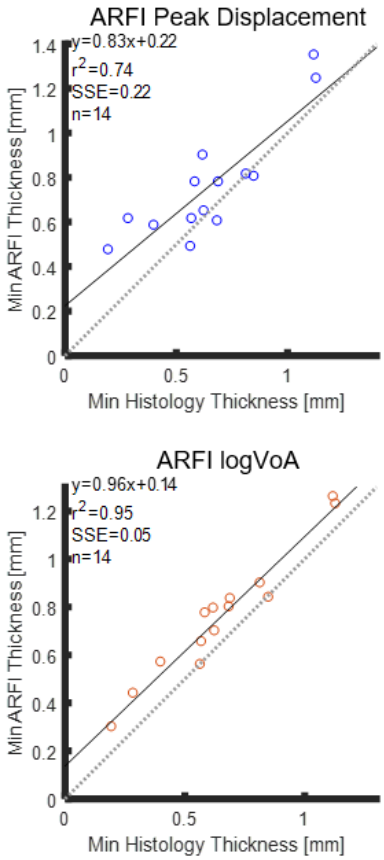

Figure 6.6: Linear regressions of ARFI PD- (top) and log(VoA)- (bottom) derived minimum fibrous cap thicknesses versus minimum histological standard over fourteen human carotid plaques, in vivo (black lines). Median values per plaque are shown as circular scatters. R^2: coefficient of determination. SSE: Sum of squared error.

Figure 6.4 illustrates that, over all 14 examined plaques, median fibrous cap thickness measured by log(VoA) is more strongly correlated ($R^2 = 0.97$) with the histological validation standard than that measured using PD ($R^2 = 0.79$). Further, the CCC of 0.95 for log(VoA) versus 0.62 for PD suggests that ARFI log(VoA) enables more accurate and precise measurement of median fibrous cap thickness than ARFI PD. Figure 6.5 also supports that median fibrous cap thickness measurement is more accurate and precise by log(VoA) than by PD. While neither parameter's bias was statistically significant ($p<0.05$), log(VoA) bias was 0.05 mm versus 0.10 mm for PD. Similarly, the (reproducibility coefficient (RPC) and coefficient of variation (CV)) were lower for log(VoA) (0.10 and 6.3%) than for PD (0.26 and 16%) median fibrous cap thickness measurements.

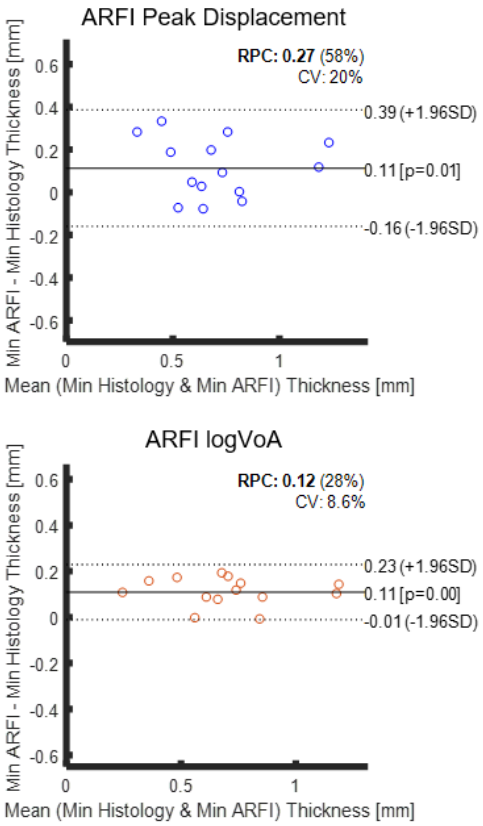

Figure 6.7: Bland-Altman plots assessing the reproducibility of minimum plaque thickness results derived from ARFI PD (top) and ARFI logVoA (bottom). RPC: Reproducibility coefficient, CV: Coefficient of variation.

While the accuracy and precision of median fibrous cap thickness measurement suggest general utility, ability to measure minimum fibrous cap thickness indicates relevance to identify caps with high rupture potential. In figures 6.6 and 6.7, minimum fibrous cap thickness measures were more strongly correlated to the histological standard (R^2 = 0.95 v. 0.74) and had lower error (SSE = 0.22 v. 0.05) when measured by log(VoA) versus PD. Moreover, log(VoA) measures of minimum fibrous cap thickness had lower RPC and CV (0.12 and 8.6%) than PD measures (0.27 and 20%). Interestingly, both log(VoA) and PD measures of minimum fibrous cap thickness had the same bias (0.11), but neither bias was statistically significant ($p<0.05$). These results show that log(VoA) enables more accurate and precise measures of minimum fibrous cap thickness than PD, suggesting that rupture potential is better determined by log(VoA).

Like median and minimum, log(VoA) outperforms PD in terms of accuracy and precision of

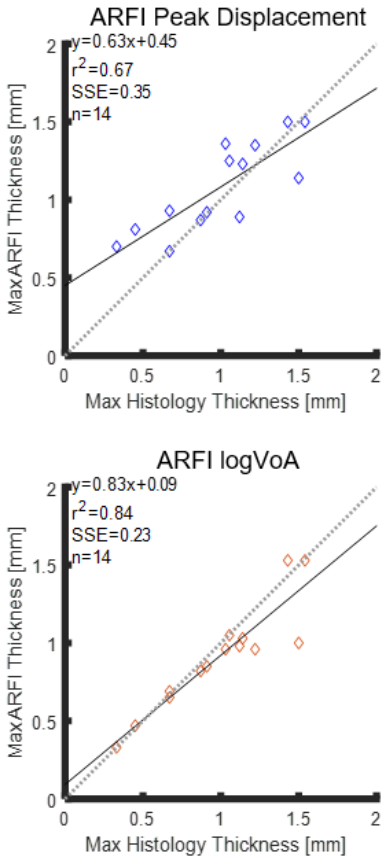

Figure 6.8: Linear regressions of ARFI PD- (top) and log(VoA)- (bottom) derived maximum fibrous cap thicknesses versus maximum histological standard over fourteen human carotid plaques, in vivo (black lines). R^2: coefficient of determination. SSE: Sum of squares error.

maximum fibrous cap thickness measurement. Figure 6.8 shows that log(VoA) maximum fibrous cap thickness measures are more strongly correlated to the histological standard (R2 = 0.84 v. 0.67) and had lower error (SSE = 0.23 v. 0.35) than PD. Further, in figure 6.9, log(VoA) had greater precision than PD (RPC = 0.29 v. 0.42; CV = 16% v. 21%). Finally, while both log(VoA) and PD measures of maximum fibrous cap thickness had statistically significant bias (p>0.05), the log(VoA) bias was -0.08 mm, while the PD bias was 0.08.

More accurate and precise median, minimum, and maximum fibrous cap thickness measurement by log(VoA) versus PD is consistent with results previously reported by Torres et al. [111], which showed that contrast-to-noise ratio (CNR) for differentiating collagen from LRNC was 3.3 times greater by log(VoA) than by PD and that CNR for discriminating stiff from soft plaque features was

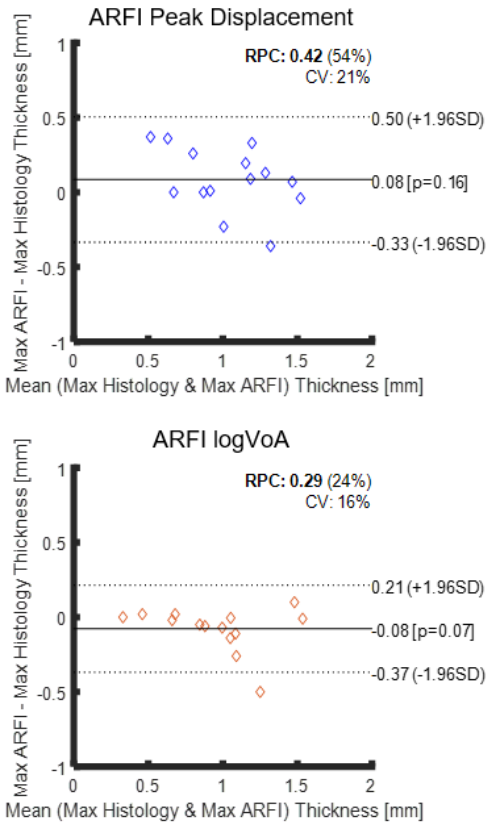

Figure 6.9: Bland-Altman plots assessing the reproducibility of maximum plaque thickness results derived from ARFI PD (top) and ARFI logVoA (bottom). RPC: Reproducibility coefficient, CV: Coefficient of variation.

3.6 times greater. However, an unexpected outcome is that, for both log(VoA) and PD, maximum fibrous cap thickness measurement performance was worse than median and minimum cap thickness measurement performance. Specifically, maximum thickness measures were less correlated with the histological standard (PD $R^2 = 0.67$ for maximum v. 0.79 for median and 0.74 for minimum, log(VoA) $R^2 = 0.84$ for maximum v. 0.97 for median and 0.95 for minimum), had higher error (PD SSE = 0.35 for maximum v. 0.19 for median and 0.22 for minimum, log(VoA) SSE = 0.23 for maximum v. 0.03 for median and 0.05 for minimum), and had lower precision (PD RPC = 0.42 for maximum v. 0.26 for median and 0.27 for minimum, log(VoA) RPC = 0.29 for maximum v. 0.10 for median and 0.12 for minimum). The reasons for the observed poorer maximum fibrous cap thickness performance are yet to be determined.

It is interesting to consider that, relative to PD, log(VoA) yielded thinner fibrous cap delineations

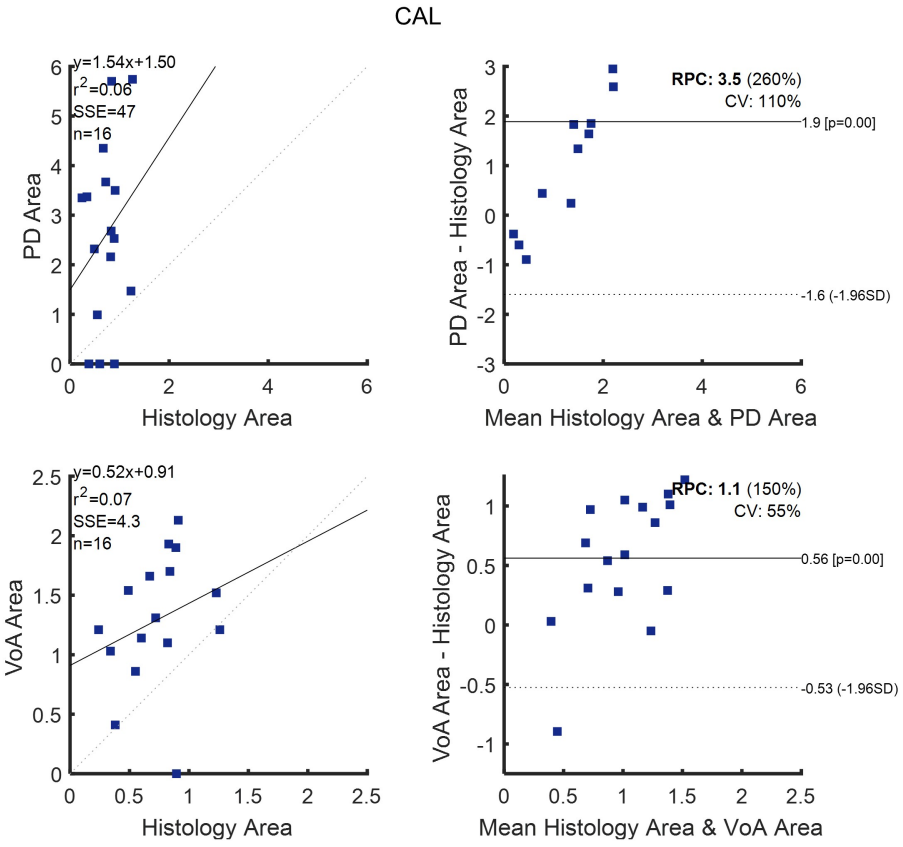

Figure 6.10: Regression and Bland-Altman plots assessing the reproducibility of calcium area results derived from ARFI PD (top) and ARFI logVoA (bottom). RPC: Reproducibility coefficient, CV: Coefficient of variation.

on both the lumen-cap (median difference of -0.33 $\pm$ 0.21 mm) and cap-LRNC (median difference of 0.21 $\pm$ 0.10 mm) interfaces. These data suggest that log(VoA) improves discrimination of fibrous cap from LRNC (which is consistent with results reported in [111]) and from luminal blood (which has not been previously shown). Future studies are needed to more comprehensively evaluate log(VoA)'s potential for discriminating plaque from blood under variable flow and clutter conditions.

Additionally, it is important to note that for all plaque components analysed, all area measurements achieved higher correlation to histology using log(VoA) compared to PD. Specifically, area measurements were improved when using log(VoA) compared to PD for CAL (CV for PD: 110%, VoA: 55%), LRNC (CV for PD: 45%, VoA: 40%), and IPH (CV for PD: 120%, VoA: 36%), independently.

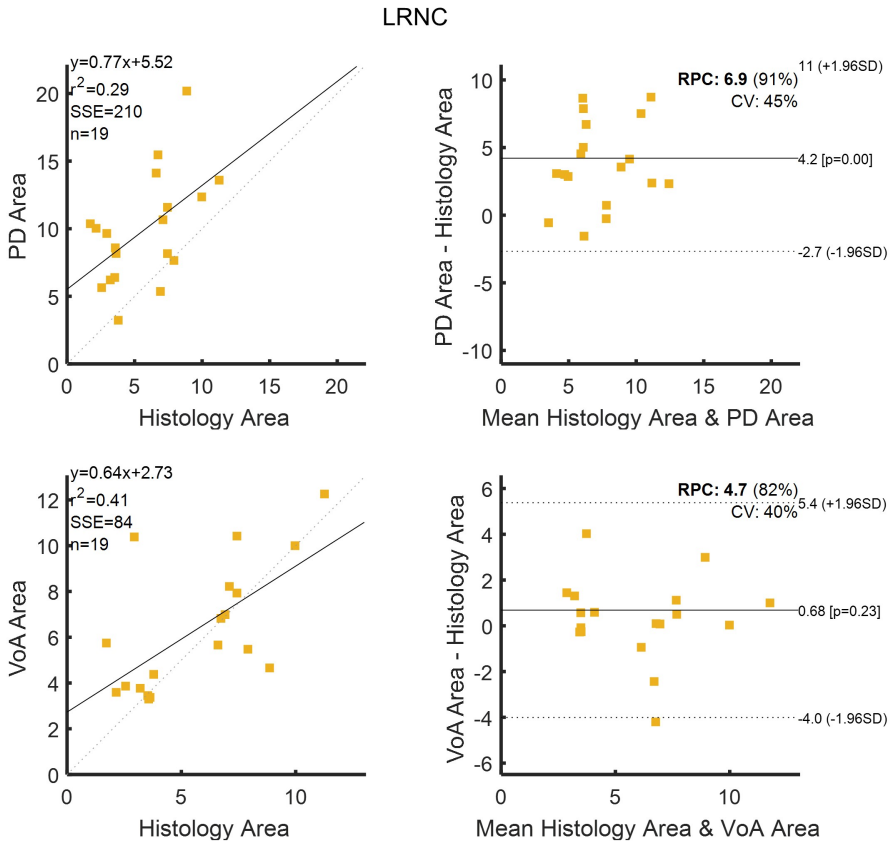

Figure 6.11: Regression and Bland-Altman plots assessing the reproducibility of lipid-rich necrotic core area results derived from ARFI PD (top) and ARFI logVoA (bottom). RPC: Reproducibility coefficient, CV: Coefficient of variation.

Aspects of the study design may have influenced outcomes. First, component area measurement performances by ARFI PD and log(VoA) were evaluated relative to histology-derived measurements, which was considered to be a validation standard. However, inconsistency between areas in histology and ARFI images could arise due to plaque stretching and/or compression during *in vivo* imaging or due to sample shrinkage during histological processing. Plaque stretching and compression were minimized by acquiring *in vivo* data with gating to diastole, and specimens that were evidently warped were excluded from the study.

In addition, it is important to consider that the ARFI imaging focal depth could have impacted fibrous cap thickness and component area measurement. In this study, the imaging focal depth was determined by the position of the carotid plaque and ranged from 1.8 to 2.3 cm across the

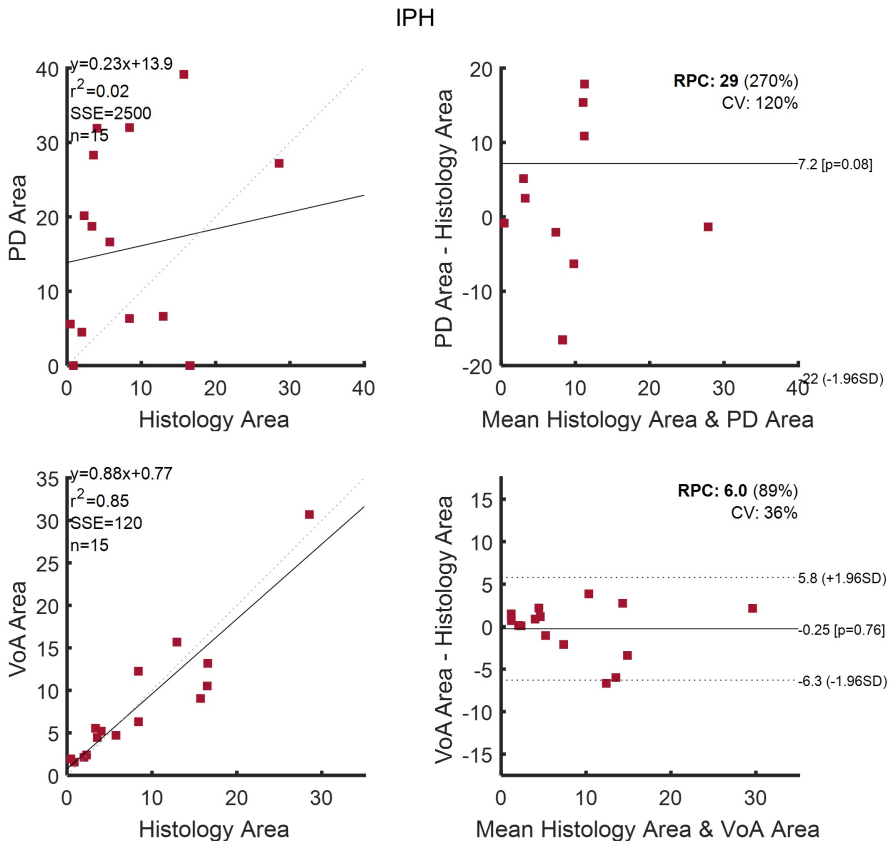

Figure 6.12: Regression and Bland-Altman plots assessing the reproducibility of intraplaque hemorrhage area results derived from ARFI PD (top) and ARFI logVoA (bottom). RPC: Reproducibility coefficient, CV: Coefficient of variation.

examined plaques. Generally speaking, deeper focal depths experience lower radiation force magnitude [113, 109], and therefore smaller displacements, which could reduce plaque component contrast in PD and log(VoA) images. Further, tracking ARFI-induced displacements at deeper focal depths results in lower SNR and higher jitter, to the potential detriment of component contrast by both PD and log(VoA).

Along with focal depth, the implemented tracking center frequency (6.15 MHz) and normalized axial cross-correlation displacement tracking kernel size (1.5λ) could have impacted fibrous cap thickness measurement. Czernuszewicz et al. showed that for these values, the expected minimum fibrous cap thickness measurement resolution is 0.2 mm [110], which is comparable to the thickness of the thinnest fibrous cap included in this study. Notably, no caps thinner than 0.2 mm were contained

in the available data set and, therefore, could not be evaluated. Using higher tracking center frequencies and/or smaller displacement tracking kernel sizes could improve thickness resolution, but at the potential cost of SNR and increases in jitter that impact fibrous cap contrast in PD and log(VoA) images. Comparing *in vivo* ARFI fibrous cap thickness measurement across tracking center frequencies and kernel sizes is work in progress.

Another factor impacting ARFI-based plaque area measurement is reverberation clutter, which can be accentuated when calcium deposits are present in the plaque [8]. Clutter artifact corrupts displacement estimation as well as signal correlation and SNR and therefore diminishes component contrast in PD and log(VoA) images. Advanced clutter filters and harmonic imaging could suppress clutter artifact and improve fibrous cap thickness and component area measurement [99, 95].

Finally, while the results reported herein suggest that *in vivo*, human carotid fibrous cap thickness and component area measurement is better supported by log(VoA) than by PD imaging, and while Bland Altman analyses and the CCC showed that performance improved when using log(VoA) in comparison to PD, the work is pilot in nature. After exclusions, only twenty examples were included, and larger studies are needed in the future to more comprehensively compare ARFI PD and log(VoA) for fibrous cap thickness and component area measurement.

6.5 Conclusion

This chapter demonstrates the potential of ARFI log(VoA) for improving fibrous cap thickness and component area measurement in comparison to ARFI PD. In fourteen human carotid plaques, imaged *in vivo*, log(VoA)-derived fibrous cap thickness is more strongly correlated to true thickness, has a higher CCC, and is less variable than PD-derived fibrous cap thickness. Further, in twenty human carotid plaques, a blinded-reader study achieved better performance when delineating plaque composition when using log(VoA) images than when using ARFI PD. Overall, these results suggest that ARFI-based imaging, evaluating log(VoA) in particular, is relevant to delineating carotid plaque structure and composition for vulnerable carotid plaque detection. In the following chapter, this analysis will be extended to the application of log(VoA) in a blinded-reader study where a group of six readers used this ARFI-derived parameter for identifying and delineating plaque composition and structure.

CHAPTER 7

BLINDED-READER PERFORMANCE OF ARFI LOG(VOA) PLAQUE CHARACTERIZATION

7.1 Introduction

In the previous chapter, ARFI log(VoA) was demonstrated to achieve higher accuracy and precision for fibrous cap thickness and component area measurement than ARFI PD. However, results were derived using a semi-automatic segmentation method that used *a priori* knowledge of true component location from histology to seed component area clusters. To evaluate the performance of ARFI log(VoA) in a more clinically realistic scenario, one in which no *a priori* information about plaque component types or locations is available, a statistical reader study was performed.

This chapter evaluates log(VoA) for delineating the structure and composition of human carotid atherosclerotic plaque *in vivo*, as assessed by six blinded readers comprising three neuroradiologists, one abdominal radiologist, one pathologist, and one sonographer [8]. Results suggest improved reader performance using log(VoA) versus ARFI PD for delineating CAL, COL, LRNC, and IPH, independently.

7.2 Methods

Analysis of log(VoA) in a blinded-reader study was performed to further investigate its performance for improving discrimination between plaque features. Specifically, ARFI imaging was performed using a Siemens S3000 scanner and a 9L4 linear array with fundamental tracking at 8.89 MHz and harmonic tracking at 8.0 MHz. Then, after using 1D normalized cross-correlation to estimate ARFI-induced axial displacement profiles, both log(VoA) and PD were calculated. For all methods, ARFI excitations were 300 cycles in duration. All tracking pulses were two cycles with a F/1.5 focal configuration. ARFI imaging was performed *in vivo* in 21 patients with 50-99% stenotic carotid artery plaque with clinical indication for CEA. A registered sonographer acquired data with gating to diastole and systole with imaging directed at the plaque indicated for CEA.

Once *in vivo* ARFI data acquisition was completed, the plaque samples underwent volumetric

μCT imaging. The μCT images were used to identify arterial shape and morphology and support fine alignment of imaging and histology planes, as previously performed in [8]. With calcium recorded on μCT images, the samples then were decalcified to prevent tearing during sectioning, and sections were stained with H&E and CME. A pathologist with expertise in atherosclerosis identified and delineated TRFC, CAL, COL, LRNC, and IPH in histology images, and the pathologist's ratings were used as the validation standard for ARFI performance, as performed previously [8]. Finally a blinded-reader study was implemented to assess log(VoA) for identifying plaque components. The readers included three neuroradiologists, one radiologist, one sonographer, and one pathologist (who did not evaluate the histology).

7.3 Results

Tables 7.1 - 7.3 show Regression and Bland-Altman results for delineating calcium, collagen, lipid-rich necrotic core, and intraplaque hemorrhage, respectively, for all readers participating in the Part II trained blinded-reader study. Neuroradiologists are readers 2, 3 and 6.

Neuroradiologists averaged CVs of 29.7%, 39.7%, 28.3%, and 48% for delineating CAL, COL, LRNC, and IPH, respectively. The other three readers averaged CVs of 33%, 43%, 25.7%, and 60% for delineating CAL, COL, LRNC, and IPH, respectively. In terms of bias, neuroradiologists averaged 1.3, 0.22, 0.86, 0.43 mm for delineating CAL, COL, LRNC, and IPH, respectively, versus the other readers who averaged 1.1, 0.44, 0.94, and 0.63 mm for delineating CAL, COL, LRNC, and IPH, respectively.

CAL	Regression		Bland-Altman		
Reader	R2	SSE	RPC	CV	Bias [mm]
1	0.80	120	5.8	42	**0.89**
2	0.90	68	4.3	32	1.30
3	0.90	57	**3.4**	**26**	1.40
4	0.86	79	4.0	31	1.30
5	**0.93**	**41**	**3.4**	**26**	0.96
6	0.88	77	4.0	31	1.20
Average (all readers)	0.88	73.67	4.15	31.33	1.18
Average (only NR)	0.86	88.33	4.70	35.00	1.13

Table 7.1: Calcium area measurement metrics from regression and Bland Altman analysis for all trained blinded-to-histology readers. SSE = sum of squared errors, RPC = reproducibility coefficient, CV = coefficient of variation, NR = Neuroradiologists.

Boxplots of AUC values achieved by the readers are shown in Figure 7.1-top for each of the four plaque components evaluated in this study (CAL, COL, LRNC, IPH), as well as combined

LRNC	Regression		Bland-Altman		
Reader	R2	SSE	RPC	CV	Bias [mm]
1	0.86	90	5.4	27	0.43
2	**0.91**	74	4.6	26	**0.36**
3	0.88	78	4.7	29	1.30
4	0.85	120	5.2	29	1.40
5	0.90	**60**	**3.9**	**21**	1.00
6	0.90	100	5.3	30	0.91
Average (all readers)	0.88	87	4.85	27	0.90
Average (only NR)	0.89	88	5.10	27.67	0.57

Table 7.2: Lipid-rich necrotic core area measurement metrics from regression and Bland Altman analysis for all trained blinded-to-histology readers. SSE = sum of squared errors, RPC = reproducibility coefficient, CV = coefficient of variation, NR = Neuroradiologists.

IPH	Regression		Bland-Altman		
Reader	R2	SSE	RPC	CV	Bias [mm]
1	**0.92**	**9.9**	3.2	37	0.44
2	0.72	15	**2.6**	42	0.57
3	0.66	110	5.6	70	0.27
4	0.45	210	7.6	82	1.40
5	0.54	85	5.0	61	**0.06**
6	0.87	25	**2.6**	**32**	0.46
Average (all readers)	0.69	75.82	4.43	54	0.53
Average (only NR)	0.84	16.63	2.80	37	0.49

Table 7.3: Intraplaque hemorrhage area measurement metrics from regression and Bland Altman analysis for all trained blinded-to-histology readers. SSE = sum of squared errors, RPC = reproducibility coefficient, CV = coefficient of variation, NR = Neuroradiologists.

categories (CAL/COL and LRNC/IPH). Figure 7.1 depicts the results for all six readers, and Figure 7.1-bottom shows the results for the neuroradiologists alone. When all readers were considered, the average AUCs for each feature were as follows: LRNC, 0.79; COL, 0.76; IPH, 0.82; CAL, 0.77. The median AUC for the combined categories were higher than both taken separately, with the COL/CAL category reaching a average AUC of 0.88 and the LRNC/IPH category reaching a median AUC of 0.87. When only the AUCs from the neuroradiologists were considered, the average AUCs for each feature were as follows: LRNC, 0.78; COL, 0.74; IPH, 0.77; CAL, 0.74. The average AUC for the combined metrics when only considering neuroradiologists were 0.91 for COL/CAL and 0.92 for LRNC/IPH. Compared to the results in [8] based on ARFI PD, readers' average AUCs improved by 16.56% for COL/CAL and 1.16% for LRNC/IPH, and significantly improved by 36.04% for CAL, 17.47% for COL, for 3.67% LRNC, and for 28.93% IPH.

The readers' ROC analysis results for the independent plaque categories are shown in Table 7.4,

including sensitivities and specificities for an operating point that maximizes their sum.

Reader	CAL			COL			LRNC			IPH		
	AUC	Sens	Spec	AUC	Sens	Spec	AUC	Sens	Spec	AUC	Sens	Spec
1	0.79	0.72	0.72	0.83	0.77	0.77	0.84	0.78	0.78	0.91	0.85	0.85
2	0.70	0.65	0.75	0.62	0.58	0.63	0.71	0.69	0.62	0.71	0.75	0.65
3	0.81	0.75	0.71	0.75	0.68	0.68	0.86	0.81	0.74	0.82	0.74	0.74
4	0.76	0.69	0.69	0.62	0.66	0.51	0.70	0.68	0.61	**0.92**	0.89	0.81
5	**0.82**	0.74	0.74	**0.91**	0.88	0.79	**0.87**	0.94	0.73	0.78	0.71	0.71
6	0.72	0.76	0.66	0.85	0.84	0.71	0.77	0.63	0.63	0.77	0.81	0.69
Average (all readers)	0.77	0.72	0.71	0.76	0.74	0.68	0.79	0.76	0.69	0.82	0.79	0.74
Average (only NR)	0.74	0.71	0.71	0.77	0.73	0.70	0.77	0.70	0.68	0.80	0.80	0.73

Table 7.4: AUC, sensitivity and specificity achieved by all readers for plaque categories. NR = Neuroradiologists.

7.4 Discussion

This chapter shows results that support the effectiveness of using log(VoA) for identifying plaque components and measuring their corresponding areas in comparison to PD [8]. Specifically, all blinded-readers that used log(VoA) achieved high correlation with histology when measuring component areas, overall having an average R^2 higher than 0.69, and an average bias lower than 1.18 mm.

For calcium, all readers on average achieved an $R^2 = 0.88$, CV = 37, and a bias of 1.18 mm. On average, neuroradiologists achieved $R^2 = 0.86$, CV = 35, and a bias of 1.13 mm. These results indicate that all readers performed comparably and neuroradiologists achieved lower bias but higher variability than the overall readers.

For lipid-rich necrotic core, all readers on average achieved an $R^2 = 0.88$, CV = 27, and a bias of 0.90 mm. On average, neuroradiologists achieved $R^2 = 0.89$, CV = 27, and a bias of 0.57 mm. These results show comparable performance by all readers in terms of correlation with histology, neuroradiologists achieved lower bias but comparable variability compared to the overall readers.

For intraplaque hemorrhage, all readers on average achieved an $R^2 = 0.69$, CV = 54, and a bias of 0.53 mm. On average, neuroradiologists achieved $R^2 = 0.84$, CV = 37, and a bias of 0.49 mm. These results show higher performance by neuroradiologists in terms of higher correlation with histology, lower variability and lower bias.

In terms of performance, on average readers had AUCs higher than 0.68 for identifying plaque components independently. This represents an important improvement compared to [8] in which readers achieved AUCs between 0.50 and 0.92 when identifying independent components. When

comparing AUCs when all readers were considered, the median AUCs for each feature were as follows: calcium, 0.775 (compared to 0.566 in [8]); lipid-rich necrotic core, 0.805 (compared to 0.762 in [8]); intraplaque hemorrhage, 0.80 (compared to 0.0.636 in [8]). When only the AUCs from the neuroradiologists were considered, the median AUCs for each feature were as follows: calcium, 0.720 (compared to 0.612 in [8]); lipid-rich necrotic core, 0.770 (compared to 0.809 in [8]); intraplaque hemorrhage, 0.770 (compared to 0.639 in [8]).

When further comparing performance with [8], readers' average AUCs for grouped components improved by 16.56% for COL/CAL and 1.16% for LRNC/IPH, and significantly improved for independent components by 36.04% for CAL, 17.47% for COL, for 3.67% LRNC, and for 28.93% IPH. These results highlight that log(VoA) improved all readers' performance for delineating plaque components compared to using PD.

Additionally, it is interesting to mention that in [8], neuroradiologists achieved significantly higher performances than other readers, whereas in the present study, all readers achieved comparable high performances for identifying independent plaque components, as visible in 7.1. In terms of bias, neuroradiologists achieved lower bias when delineating component areas, but comparable variability and correlation with histology.

Even though results are encouraging, reader-based delineation presents challenges in terms of variability. User training is also required for higher performance, as it impacts the bias when characterizing plaque composition. Plaque delineation independent of reader assessment reduces these limitations and will be explored in the next chapter.

7.5 Conclusion

This study has demonstrated the potential for blinded readers to use log(VoA) for discriminating plaque components independently. All readers achieved relatively high AUCs for distinguishing individual plaque components, compared to a previous blinded reader study where delineation was performed using ARFI PD. Additionally, the performance of log(VoA) for plaque characterization was shown to be not highly correlated with reader specialization (with neuradiologists performing not-significantly better than other readers). Given these encouraging preliminary results, the next step to characterizing plaque structure and composition via ARFI will be to develop automatic classification algorithms without reader variability.

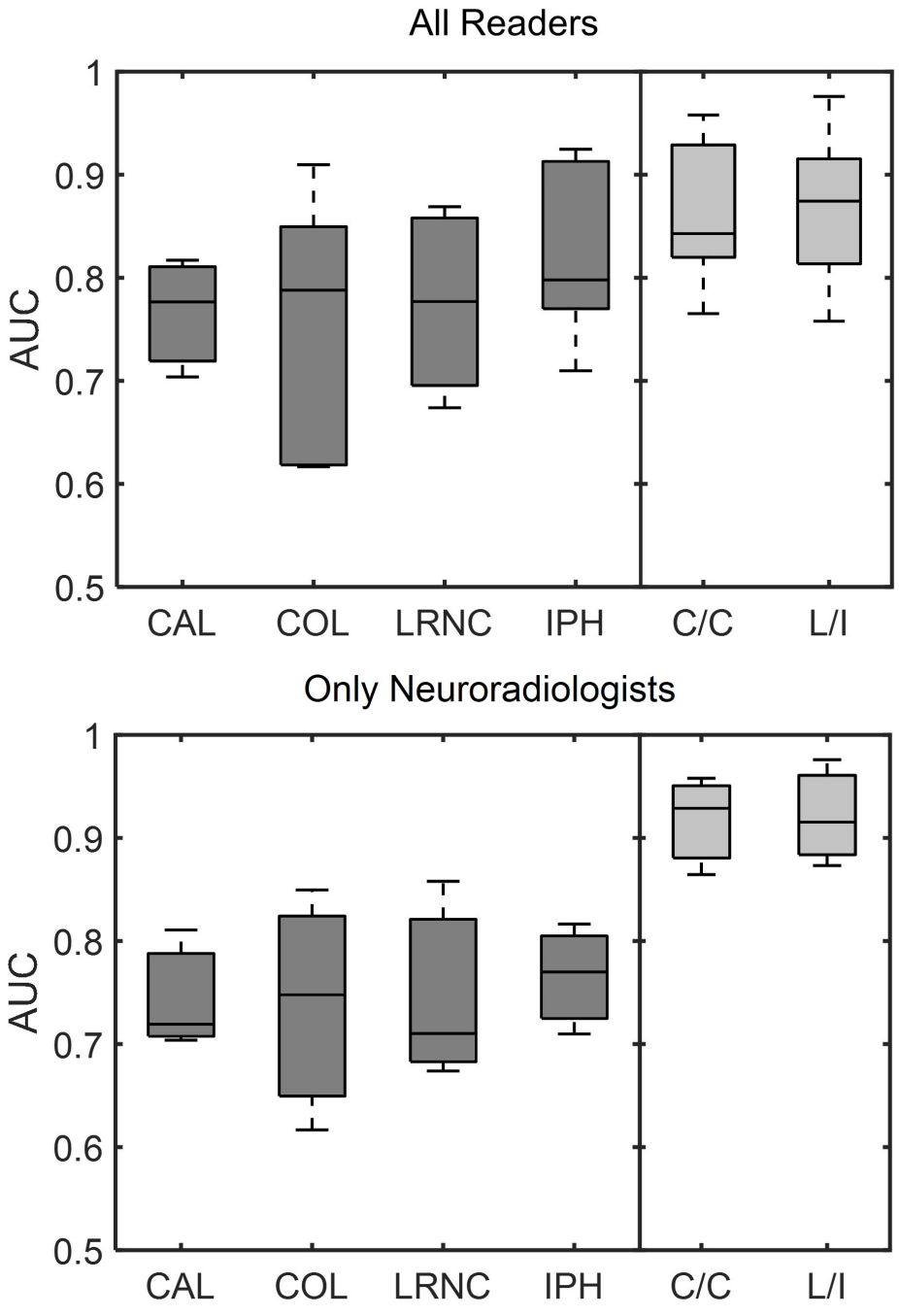

Figure 7.1: Performance for identifying calcium, collagen, lipid-rich necrotic core, and intraplaque hemorrhage from (top) all readers, and (bottom) only neuroradiologists.

CHAPTER 8

MACHINE LEARNING ALGORITHMS TO CLASSIFY PLAQUE COMPONENTS

8.1 Introduction

Ultrasound technologies that aim to delineate plaque structure and composition include those that interrogate speckle characteristics [114, 115, 116] and those that evaluate mechanical property [81, 117, 118]. A new ultrasound-based approach to delineating plaque structure and composition incorporates both speckle characteristics and mechanical property by evaluating the decadic log of the Variance of Acceleration, or log(VoA), derived from Acoustic Radiation Force Impulse (ARFI) imaging [96, 97]. In the previous chapter, the log(VoA) parameter differentiates plaque components by exploiting differences in displacement estimation variance, often referred to as jitter [102], which is impacted by variation in signal-to-noise ratio (SNR) and signal correlation. Echo-bright features that remain highly correlated because they displace minimally in response to an ARFI excitation, like calcium, yield low log(VoA). Conversely, echo-dim features that decorrelate because they displace substantially in response to an ARFI excitation, like intraplaque hemorrhage, yield high log(VoA). The log(VoA) parameter has been demonstrated to statistically differentiate intraplaque hemorrhage, lipid-rich necrotic core, collagen, and calcium *in vivo* in the carotid plaques of patients undergoing clinically-indicated carotid endarterectomy (CEA), with higher sensitivities and specificities for differentiating between soft (intraplaque hemorrhage versus lipid-rich necrotic core) and between stiff (collagen versus calcium) plaque components than achieved by evaluating ARFI peak displacement (PD) [8]. Further, log(VoA) has been shown to improve the accuracy and precision of fibrous cap thickness measurement in human carotid plaques *in vivo* relative to ARFI PD [111].

While evaluating ARFI log(VoA) has improved discrimination of carotid plaque components that convey rupture risk relative to ARFI PD, greater performance gains may be possible by enhanced evaluation of SNR, correlation, and displacement information. Further, a remaining impediment to widespread clinical adoption of log(VoA) as a diagnostic standard is correct interpretation of

qualitative log(VoA) outcomes. The diagnostic relevance of ARFI plaque interrogation could be improved by automated classification of plaque constituents, which may be possible by machine learning models. Machine learning has previously been applied to differentiating tissue [119, 120, 121] and, more specifically, to identifying carotid plaque features using echogenic [122, 123, 124] and mechanical [117, 125] features. However, achieving semiautomatic differentiation of independent plaque features with high sensitivity and specificity remains a challenge. In this chapter, two machine learning-based automated classification schemes are herein described and compared to each other, to log(VoA), and to peak displacement in terms of plaque feature contrast, fibrous cap thickness measurement, and receiver operating characteristic analysis with spatially matched histological validation *in vivo* in 25 patients undergoing clinically indicated CEA.

8.2 Methods

8.2.1 Patient Recruitment

Following the protocol described in 4.4 [8], 25 patients undergoing clinically indicated CEA were recruited from UNC Hospitals. Inclusion criteria included asymptomatic carotid artery disease with >60% Doppler-indicated stenosis and unresponsive to medical management or symptomatic carotid artery disease with a stenosis suspected to be the source of emboli. All procedures were approved by the University of North Carolina Chapel Hill Institutional Review Board, and written informed consent was given from each study participant (ClinicalTrials.gov No. NCT01581385). From the 25 patients, a total of 26 plaques were collected, and after exclusions due to specimen damage or fracture during surgery (N = 6), a total of 20 plaques were evaluated [8].

8.2.2 ARFI Imaging

A Siemens Acuson Antares imaging system equipped for research and VF7-3 linear array transducer (Siemens Healthineers, Ultrasound Division, USA, Inc.) were used for *in vivo* imaging. ARFI excitation pulses were 300-cycles at 4.21 MHz, tracking pulses were 2-cycles at 6.15 MHz, and acquisitions were timed to diastole using electrocardiogram gating.

A registered sonographer acquired all imaging data before patient sedation on the same day of surgery. The plaque to be removed by CEA was identified from prior ultrasound imaging sessions archived in the patients' medical record and was typically the plaque with the greatest stenosis. Before completing the ARFI imaging session in which the artery was evaluated in the longitudinal

plane, the transducer was rotated 90°, and transverse B-modes and CINE loops of the carotid bifurcation were obtained to aid in sample alignment. The time interval between imaging and specimen extraction was approximately four hours.

8.2.3 Histology Processing

The extracted CEA specimens were fixed in 10% neutral-buffered formalin (48 hours) and then imaged by μCT with a Scanco μCT 40 (Scanco Medical AG, Bassersdorf, Switzerland) at an isotropic voxel resolution of 20 μm. The purpose of *ex vivo* micro-CT was twofold: 1) to identify and localize calcifications in the samples so that the samples could be de-calcified prior to sectioning, and 2) to orient the specimens before embedding in paraffin so that histology sections were aligned with ARFI imaging planes [16]. Once sectioned, samples were stained with hematoxylin and eosin (H&E), Von Kossa (VK), and combined Masson's elastin (CME) stains. A pathologist with experience in atherosclerosis examined and annotated the digitized histology slides to identify plaque features.

8.2.4 ARFI Data Processing

From the acquired radio frequency data, temporal profiles of SNR were calculated as μ/σ, where μ represents the signal amplitude in each independent pixel per frame, and σ represents the noise component, which was calculated as the average signal amplitude in a 3 x 3 mm^2 anechoic region inside the lumen of each carotid artery. The size of the noise region was selected as the size of the largest anechoic region consistently recognizable in all of the carotid images. Additionally, temporal profiles of correlation and displacement were calculated from the radio frequency data using one-dimensional (axial) normalized cross correlation (NCC) with a 1.5λ (376-μm) kernel, two-stage interpolation, and linear motion filtering [91]. From the displacement profiles, log(VoA) was calculated as indicated in Equation 6.1.

Parametric log(VoA) images were rendered with normalization to $\pm$ two median absolute deviations. Then, from these images, plaque components (collagen, calcium, lipid-rich necrotic core, and intraplaque hemorrhage) were segmented using a semiautomatic k-means clustering method, which we have previously described [8]. The method involved first cropping histology images to the region that spans the ultrasonically interrogated plaque region. Then, the centroids of the plaque features identified by the pathologist were identified. Next, histology images were resized so that the numbers of lateral and axial pixels in the cropped histology image matched those of the log(VoA) image. Finally, the histology-derived centroid positions in the log(VoA) image were input to the

k-means algorithm as the starting locations for k regions to be segmented in the parametric image, where k is the number of plaque component regions identified by the pathologist. This methodology supported identification of independent pixels containing intraplaque hemorrhage, lipid-rich necrotic core, collagen, or calcium.

8.2.5 Machine Learning Classifiers

After semiautomatic segmentation, in Part 1, a total of 31,756 pixels were identified as being intraplaque hemorrhage, lipid-rich necrotic core, collagen, or calcium within the 20 retained carotid plaques, and in Part 2, a total of 31,368 pixels were identified as being intraplaque hemorrhage, lipid-rich necrotic core, collagen, or calcium within the 20 retained carotid plaques From this total, pixels with overlapping plaque components as identified by the pathologist were excluded. Further, to avoid edge affects, pixels located outside 80% of the histology-derived boundary were excluded. The remaining pixels independently constituted a region of intraplaque hemorrhage, lipid-rich necrotic core, collagen, or calcium. Tables 8.1 and 8.2 indicate the number of pixels that were considered per plaque component per patient, with each pixel having spatial dimension of 354 μm x 19.25 μm (lateral x axial), for Parts 1 and 2 of the clinical study.

Plaque Component	Selected Samples	Selected Samples per Patient
CAL	6533	325 ± 75
COL	8511	426 ± 74
LRNC	8182	347 ± 239
IPH	8530	370 ± 257
Total	31756	1468 ± 157

Table 8.1: Number of samples per plaque component per patient for Part I. Each sample has corresponding temporal profiles of ARFI displacement, cross-correlation coefficient and SNR. Data acquired with Siemens Antares, VF7-3 linear array.

Plaque Component	Selected Samples	Selected Samples per Patient
CAL	7482	304 ± 71
COL	8630	426 ± 60
LRNC	7958	389 ± 61
IPH	7298	354 ± 118
Total	31368	1473 ± 78

Table 8.2: Number of samples per plaque component per patient for Part II. Each sample has corresponding temporal profiles of ARFI displacement, cross-correlation coefficient and SNR. Data acquired with Siemens S3000, 9L4 linear array.

From each pixel, temporal profiles of ARFI-induced displacement, normalized cross-correlation

coefficient (CC), and radio frequency signal to noise ratio (SNR) were calculated. These temporal profiles were used in combinations of two or three to comprise the feature set for the machine learning classifiers. Two classifiers were evaluated, the first a nonlinear radial basis function support vector machine (SVM) with a Gaussian kernel function, and the second a linear Random Forests (RaF) classifier. The classifiers were trained using 80% of the dataset per plaque component, and the remaining 20% were used for validation. The machine learning algorithms were implemented in MATLAB using the classification learner toolbox (Mathworks, Natick, MA). Five-fold cross-validation was applied for testing precision, and hyperparameter tuning was developed via grid search.

The ML classifiers predicted, on a pixel-by-pixel basis, the likelihood that a given pixel represented a region of intraplaque hemorrhage, lipid-rich necrotic core, collagen, or calcium. Output parametric images were then rendered by first assigning to each plaque component a RGB color combination (red for intraplaque hemorrhage, yellow for lipid-rich necrotic core, cyan for collagen, and blue for calcium) and then displaying the likelihood-weighted color per pixel. In this manner, a pixel that was classified as 50% likely to be intraplaque hemorrhage (with RGB color = [255 0 0]) and 50% likely to be lipid-rich necrotic core (with RGB color = [255 255 0]) would be orange (with an output RGB color = [255 128 0]), for example.

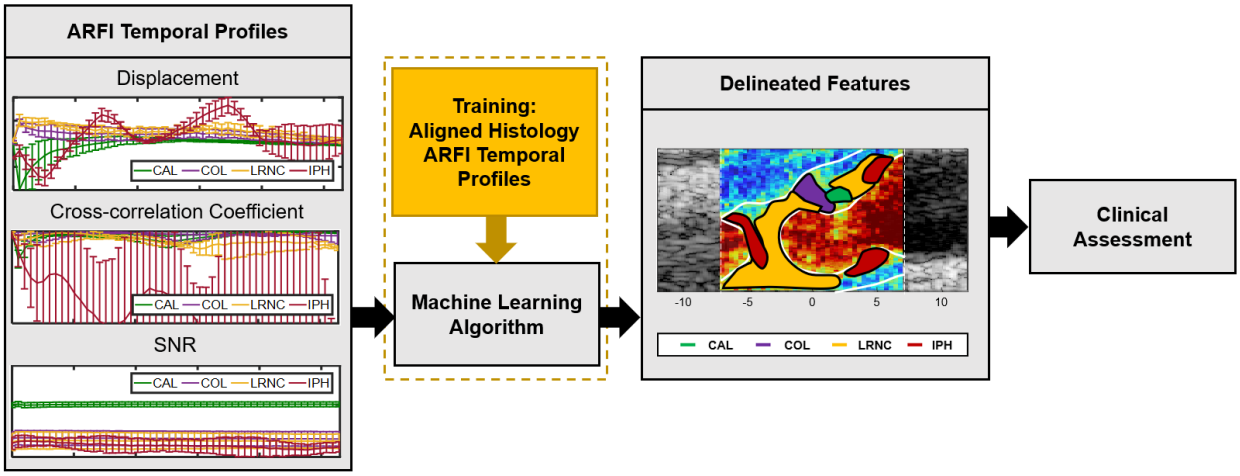

Figure 8.1: Schematic for generating automatic plaque feature segmentation with an ML algorithm. The time profile inputs to the algorithm are ARFI displacement, cross-correlation coefficient and SNR.

Figure 8.1 illustrates the process by which the SVM and RaF classifiers were implemented to generate images of plaque composition and structure. Shown on the left are representative examples

of the data comprising the machine learning feature set: temporal profiles of ARFI displacement, ARFI CC, and SNR measured in a carotid plaque from a 65-year-old, asymptomatic male patient. From these input data, the trained classifiers derived, on a pixel-by-pixel basis, the likelihood that the corresponding pixel was intraplaque hemorrhage, lipid-rich necrotic core, collagen, or calcium. From the derived likelihoods, parametric images of predicted plaque composition and structure were prepared for evaluation.

8.2.6 Classifier Performance Analysis

Machine learning classifier performance was assessed in terms of identified component contrast-to-noise ratio (CNR), receiver operating characteristics (ROC) analysis, and precision and bias of fibrous cap thickness measurement from Bland-Altman analysis. CNR outputs were evaluated per plaque and then reported as overall median CNR and CNR coefficient of variation.

The sensitivity and specificity of plaque component detection were determined by Youden's index as the values that maximized the area under the curve by ROC analysis, using the spatially matched histology as the validation standard. Performance in terms of fibrous cap thickness measurement was evaluated over 14 of the 20 retained plaques because four plaques did not contain a fibrous cap, and two were excluded because the fibrous cap was located more than 5 mm away from the focal depth. In these 14 examples, the minimum, maximum and average thicknesses of the fibrous caps in parametric RaF and SVM likelihood images were compared using Bland-Altman analysis to the corresponding minimum, maximum, and average thicknesses of the fibrous caps delineated by the pathologist from histology images.

The evaluated performance metrics were compared across feature sets and machine learning algorithms. Further, to benchmark machine learning outcomes against those previously achieved using other ARFI data evaluation methods, CNR, AUC, and Bland-Altman metrics achieved by the RaF and SVM classifiers were compared to those produced by semiautomatically segmented ARFI log(VoA) and PD images [8]. Comparisons were performed using the Wilcoxon rank-sum test, with p-values less than 0.05 indicating significance.

8.3 Results

Figures 8.2-8.4 show parametric images depicting ARFI PD, log(VoA), and RaF and SVM classifications for representative Type VI carotid plaques. Spatially matched B-Mode and histology (with plaque components marked by the pathologist) are shown for reference.

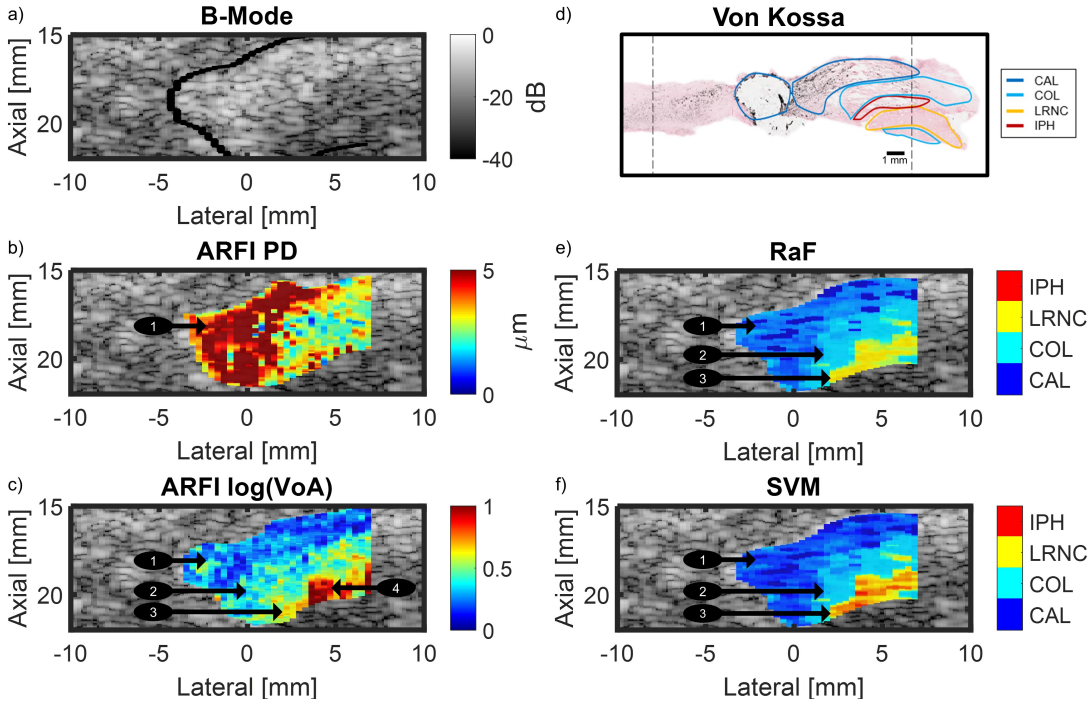

Figure 8.2: Type VI symptomatic carotid plaque with corresponding aligned histology. (a) B-Mode), (b) ARFI peak displacement, (c) ARFI log(VoA), (d) Von Kossa histology stain with plaque components delineated by pathologist, (e) ML random forest (RaF) likelihood map, (f) ML support vector machine (SVM) likelihood map.

In Figure 8.2 the histology section spatially aligned with the imaging plane shows two large calcium deposits (dark blue outlines) positioned posterior to regions of collagen (light blue outline), intraplaque hemorrhage (red outline), and lipid-rich necrotic core (yellow outline). The parametric ARFI PD image depicts large displacements in the position of the calcium deposits, which erroneously suggest soft material (arrow 1). Importantly, the regions of intraplaque hemorrhage and lipid-rich necrotic core anterior to the calcium deposits are not clearly indicated. In the parametric log(VoA) image, low (dark blue) log(VoA) in the anterior region of the plaque (arrow 1) spatially correspond to calcium deposits, below which a region of moderate (light blue) log(VoA) corresponds to collagen (arrow 2). Finally, higher (yellow and red) log(VoA) measurements in the anterior plaque region spatially correspond to lipid-rich necrotic core (arrow 3) and intraplaque hemorrhage (arrow 4). Similar to the log(VoA) image, the parametric images of RaF and SVM classifications show a region classified as calcium (dark blue, arrow 1) in the posterior portion of the plaque, which corresponds to the position of calcium in the histology section. Notably, the assessed likelihood of calcium is higher by the SMV classifier, as indicated by the darker shade of blue in the SVM image. Below the

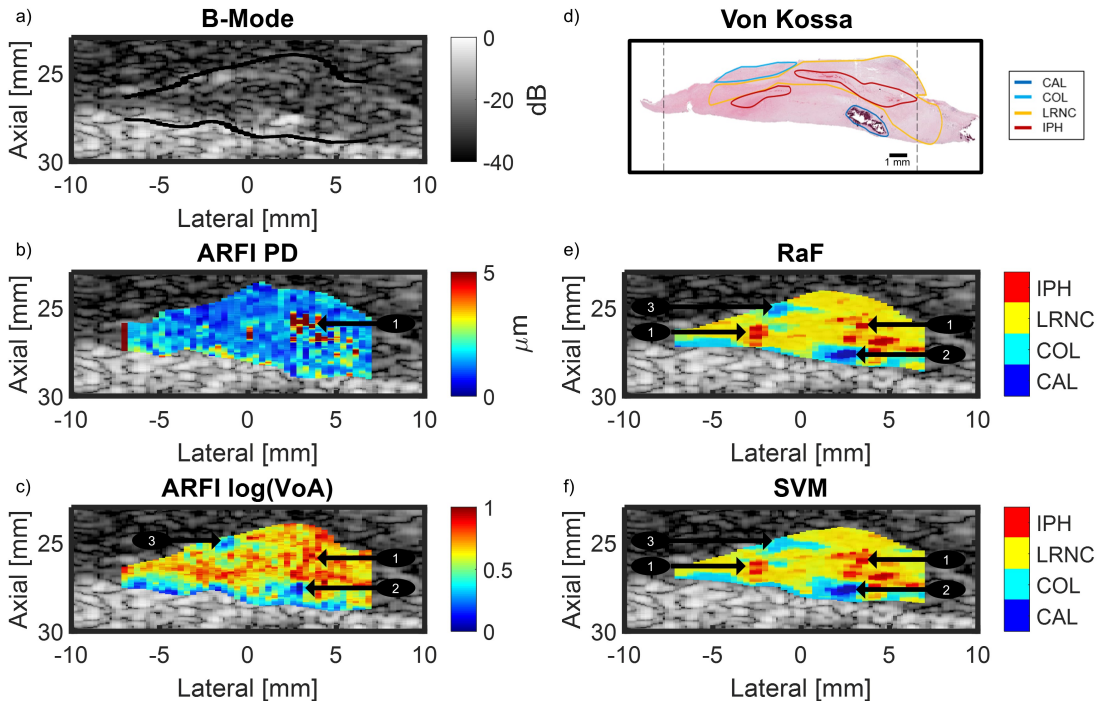

Figure 8.3: Type VI symptomatic carotid plaque with corresponding aligned histology. (a) B-Mode), (b) ARFI peak displacement, (c) ARFI log(VoA), (d) Von Kossa histology stain with plaque components delineated by pathologist, (e) ML random forest (RaF) likelihood map, (f) ML support vector machine (SVM) likelihood map.

region classified as calcium is a region classified as collagen (light blue, arrow 2), which spatially corresponds with collagen in the histology section. This collagen region is delineated comparably in RaF and SVM likelihood images. Finally, in the anterior region of the plaque, the RaF classifier identifies a region of lipid-rich necrotic core with high likelihood (as indicated by the bright yellow color, arrow 3), while for the same region, the SVM classifier predicts mixed lipid-rich necrotic core and intraplaque hemorrhage composition (as indicated by the red-orange-yellow coloring, arrow 3).

Figure 8.3 depicts the histology section spatially aligned with the imaging plane for a second type VI plaque comprised of a large lipid-rich necrotic core (yellow outline), with a small fibrous cap (light blue outline), two regions of intraplaque hemorrhage (red outlines), and a calcium deposit (dark blue outline). The parametric ARFI PD image shows predominantly low displacement (blue) within the plaque, suggesting collagen composition, with a region of high displacement (red) suggesting lipid-rich necrotic core or intraplaque hemorrhage (arrow 1) in the position of the larger region of intraplaque hemorrhage in the histology section. Notably, the large lipid-rich necrotic core is not well indicated, and neither is the calcium deposit. In panel (c), the parametric log(VoA) image

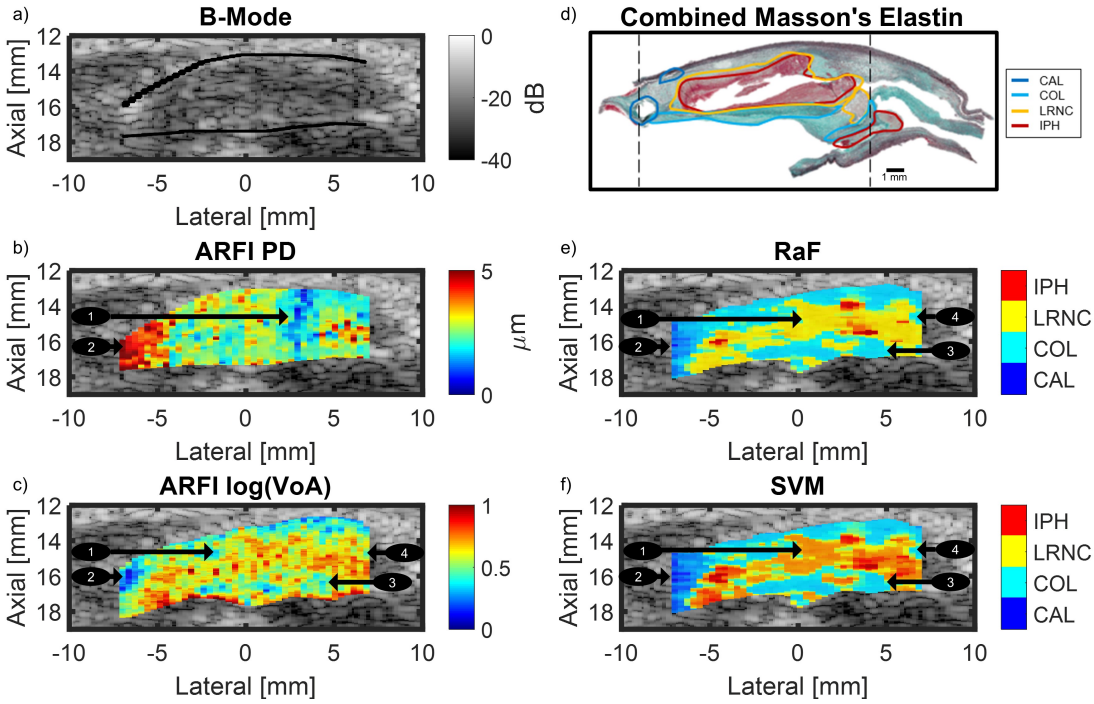

Figure 8.4: Type VI symptomatic carotid plaque with corresponding aligned histology. (a) B-Mode), (b) ARFI peak displacement, (c) ARFI log(VoA), (d) Von Kossa histology stain with plaque components delineated by pathologist, (e) ML random forest (RaF) likelihood map, (f) ML support vector machine (SVM) likelihood map.

shows predominantly high log(VoA) values (yellow), suggesting lipid-rich necrotic core, intermixed with higher (orange, red) log(VoA) values, suggesting intraplaque hemorrhage. The higher log(VoA) values aggregate (arrow 1) in regions spatially corresponding to the two regions of intraplaque hemorrhage in the histology section, but the higher values are also present throughout the plaque, which falsely suggests diffuse intraplaque hemorrhage. A moderate (light blue) log(VoA) region in the plaque shoulder (arrow 3) and a low (dark blue) log(VoA) region in the anterior region of the plaque (arrow 2) spatially correspond to positions of fibrous cap and calcium in the histology, respectively. The parametric images of RaF and SVM classifications appear quite similar to each other: a region classified as lipid-rich necrotic core spans most of the plaque, consistent with the histology section, with regions classified as intraplaque hemorrhage (red, arrows 1), collagen (fibrous cap) (light blue, arrow 3), and calcium (dark blue, arrow 2) corresponding to the positions of such in the histology section.

A third type VI plaque is shown in Figure 8.4 with histology showing a large region of combined lipid-rich necrotic core and intraplaque hemorrhage (overlapping yellow and red outlines). Below

this region is a fibrous cap (light blue outline), and two calcium deposits are in the left of the section near the edge of the lateral imaging range. The parametric ARFI PD image shows high displacement (red) on the left edge of the lateral ARFI field of view (arrow 2), falsely suggesting soft material in the position of calcium deposits. Moderately high (yellow) displacements are visible in the center of the plaque (from -5 to 2 mm laterally), where lipid-rich necrotic core and intraplaque hemorrhage are located. However, the moderately-high displacements generally span the full axial range of the plaque (13-17 mm axially) without clear indication of the fibrous cap anterior or the region of diffuse collagen posterior to the region of lipid-rich necrotic core and intraplaque hemorrhage. Low displacements (dark blue) span the axial range of the plaque from 3-4 mm laterally, which falsely suggests calcium (arrow 1), followed by a high displacing (yellow) region on the right of the lateral field of view that spatially corresponds to areas of lipid-rich necrotic core and intraplaque hemorrhage. Unlike the ARFI PD image, the log(VoA) image shows a focal region of low (dark blue) log(VoA) values (arrow 2) spatially corresponding to the position of calcium in the histology section. A large region of high (yellow) log(VoA), intermixed with higher (orange, red) values spans the majority of the plaque (arrow 1) in the location of the lipid-rich necrotic core and intraplaque hemorrhage in the histology section. Lower (light blue) log(VoA) values are seen in the positions of the fibrous cap (arrow 3) and diffuse collagen (arrow 4) anterior and posterior to the lipid-rich necrotic core and intraplaque hemorrhage, respectively. The RaF and SVM classifications both show a region on the left side of the plaque that is likely to be calcium (dark blue, arrow 2), but this region is larger than the low log(VoA) region suggesting calcium. Both classifiers identify a large feature spanning most of the lateral range of the plaque, but while the RaF classifier identifies this as being predominantly lipid-rich necrotic core (yellow) with a few small regions of intraplaque hemorrhage (arrow 1), the SVM classifier more correctly identifies the region as being roughly equally likely to be both lipid-rich necrotic core and intraplaque hemorrhage (orange, arrow 1). Both RaF and SVM classifiers correctly identify collagen (light blue) in the regions of the fibrous cap (arrow 3) posterior and of the diffuse collagen (arrow 4) anterior to the region of lipid-rich necrotic core and intraplaque hemorrhage.

Tables 8.3 and 8.4 depict receiver operating characteristic (ROC) metrics for detecting calcium, diffuse collagen, fibrous cap, lipid-rich necrotic core, and intraplaque hemorrhage, from studies Part 1 and 2, respectively. In Part 1, for detecting calcium, SVM achieved the highest AUC of

Plaque Component	Metric	AUC	Sensitivity	Specificity
Calcium	ARFI PD SS	0.631	0.598	0.598
	ARFI PD BR	0.650	0.600	0.600
	ARFI Log(VoA) SS	0.723	0.669	0.668
	RaF	0.839	**0.806**	0.773
	SVM	**0.915**	0.799	**0.822**
Diffuse Collagen	ARFI PD SS	0.581	0.558	0.557
	ARFI PD BR	**0.810**	**0.750**	**0.750**
	ARFI Log(VoA) SS	0.771	0.707	0.706
	RaF	0.775	0.668	0.65
	SVM	0.802	0.733	0.663
Fibrous Cap	ARFI PD SS	0.792	0.888	0.618
	ARFI PD BR	0.810	0.730	0.730
	ARFI Log(VoA) SS	0.852	0.771	0.77
	RaF	0.893	**0.827**	**0.796**
	SVM	**0.895**	0.781	0.72
Lipid-rich Necrotic Core	ARFI PD SS	0.715	0.736	0.583
	ARFI PD BR	0.910	0.840	0.840
	ARFI Log(VoA) SS	0.913	0.839	0.838
	RaF	0.897	0.761	0.805
	SVM	**0.915**	**0.902**	**0.855**
Intraplaque Hemorrhage	ARFI PD SS	0.589	0.571	0.555
	ARFI PD BR	0.700	0.600	0.600
	ARFI Log(VoA) SS	0.795	0.734	0.733
	RaF	0.885	0.808	0.767
	SVM	**0.928**	**0.819**	**0.821**

Table 8.3: Part 1 Study - Performance metrics for detecting calcium, diffuse collagen, fibrous cap, lipid-rich necrotic core, and intraplaque hemorrhage by ARFI PD, log(VoA), ML Random Forest (RaF), and ML Support Vector Machine (SVM). SS = Semi-automatically Segmented, BR = Best Reader.

0.95, followed by RaF (0.906), semiautomatically segmented ARFI log(VoA) (0.723), and, finally, semiautomatically segmented ARFI PD (0.631). For detecting diffuse collagen, SVM also achieved the highest AUC of 0.851, followed by RaF (0.813), ARFI log(VoA) (0.77), and, finally, ARFI PD (0.581). For detecting fibrous cap, RaF achieved the highest AUC (0.911), followed by SVM (0.909), ARFI log(VoA) (0.852), and ARFI PD (0.792). For detecting lipid-rich necrotic core, SVM achieved the highest AUC of 0.963, followed by RaF (0.924), ARFI log(VoA) (0.913), and ARFI PD (0.715). Finally, for detecting intraplaque hemorrhage, SVM also achieved the highest AUC of 0.945, followed by RaF (0.931), ARFI log(VoA) (0.795), and ARFI PD (0.589).

For Part 1 , Figure 8.5 shows regression and Bland-Altman plots for ARFI PD-, log(VoA),

Performance	Metric	AUC	Sensitivity	Specificity
Calcium	ARFI PD SS	0.608	0.684	0.623
	ARFI log(VoA) BR	0.820	0.740	0.740
	ARFI log(VoA) SS	0.830	0.767	0.750
	RaF	0.895	0.914	0.836
	SVM	**0.904**	**0.946**	**0.941**
Diffuse Collagen	ARFI PD SS	0.544	0.653	0.623
	ARFI log(VoA) BR	0.850	0.710	0.710
	ARFI log(VoA) SS	0.796	0.766	0.762
	RaF	0.895	0.808	**0.769**
	SVM	**0.899**	**0.857**	0.759
Fibrous Cap	ARFI PD SS	0.802	0.890	0.682
	ARFI log(VoA) BR	0.910	0.880	0.790
	ARFI log(VoA) SS	0.882	0.790	0.804
	RaF	0.908	**0.914**	**0.906**
	SVM	**0.912**	0.853	0.891
Lipid-rich Necrotic Core	ARFI PD SS	0.706	0.811	0.592
	ARFI log(VoA) BR	0.860	0.810	0.740
	ARFI log(VoA) SS	0.908	0.902	0.875
	RaF	0.929	0.942	0.865
	SVM	**0.938**	**0.986**	**0.937**
Intraplaque Hemorrhage	ARFI PD SS	0.600	0.602	0.563
	ARFI log(VoA) BR	0.920	0.850	0.850
	ARFI log(VoA) SS	0.772	0.756	0.740
	RaF	0.928	**0.935**	0.862
	SVM	**0.930**	0.877	**0.871**

Table 8.4: Part 2 Study - Performance metrics for detecting calcium, diffuse collagen, fibrous cap, lipid-rich necrotic core, and intraplaque hemorrhage by ARFI PD, log(VoA), ML Random Forest (RaF), and ML Support Vector Machine (SVM). SS = Semi-automatically Segmented, BR = Best Reader.

RaF-, and SVM-derived average fibrous cap thickness. The R2 values were the highest for SVM and RaF classifiers, followed by log(VoA) and then ARFI PD. Additionally, SVM achieved the lowest reproducibility coefficient (9.5%), coefficient of variation (3.3%), and bias in fibrous cap thickness measurement (Wilcoxon Ranksum test $p < 0.01$), although the RaF bias (0.04 mm) was not statistically significant. The corresponding regression and Bland-Altman results for measuring average, minimum, and maximum fibrous cap thicknesses are listed in Table 8.5.

For Part 2 , Table 8.6 shows regression and Bland-Altman results for ARFI PD-, log(VoA), RaF-, and SVM-derived average fibrous cap thickness. The R2 values were the highest for SVM and RaF classifiers, followed by log(VoA) and then ARFI PD. Additionally, SVM achieved the lowest

Measurement	Metric	R	RPC	CV	Bias [mm]	
Average FC Thickness	ARFI PD SS	0.79	0.26	16.00%	0.1	(p = 0.01)
	ARFI PD BR	0.89	0.12	9.10%	0.13	(p = 0.01)
	ARFI Log(VoA) SS	0.97	0.10	6.30%	0.05	(p <0.01)
	RaF	**0.98**	0.06	4.10%	0.04	(p <0.01)
	SVM	**0.98**	**0.05**	**3.80%**	0.04	(p <0.01)
Minimum FC Thickness	ARFI PD SS	0.74	0.58	20.00%	0.11	(p = 0.01)
	ARFI PD BR	0.75	0.58	20.00%	0.11	(p = 0.01)
	ARFI Log(VoA) SS	**0.95**	0.28	8.60%	0.11	(p <0.01)
	RaF	**0.95**	0.22	**8.50%**	0.09	(p <0.01)
	SVM	0.93	**0.21**	10.10%	0.08	(p <0.01)
Maximum FC Thickness	ARFI PD SS	0.67	0.54	21%	0.08	(p = 0.16)
	ARFI PD BR	0.70	0.50	23%	0.20	(p = 0.01)
	ARFI Log(VoA) SS	0.84	**0.24**	16%	0.08	(p = 0.07)
	RaF	0.84	0.25	18.20%	0.11	(p <0.01)
	SVM	**0.88**	**0.24**	**14%**	0.12	(p <0.01)

Table 8.5: Part 1 Study - Fibrous cap thickness measurement metrics from regression and Bland Altman analysis for average, minimum, and maximum thicknesses. RPC = reproducibility coefficient, CV = coefficient of variation, SS = Semi-automatically Segmented, BR = Best Reader.

reproducibility coefficient (9.15%), coefficient of variation (3.99%), and bias in fibrous cap thickness measurement (Wilcoxon Ranksum test $p< 0.01$), although the SVM and RaF bias (0.20 mm) was not statistically significant. The corresponding regression and Bland-Altman results for measuring average, minimum, and maximum fibrous cap thicknesses show similar trends as shown in Table 8.5.

8.4 Discussion

The in vivo human carotid plaque images shown in Figures 8.2-8.4 qualitatively demonstrate that plaque features are delineated in a manner that is generally more accurate to component type and more spatially precise by RaF and SVM classifiers than by log(VoA) or ARFI PD. Quantitative evaluations of feature CNR, shown in Table 8.2, and AUC analyses of sensitivity and specificity of feature detection, shown in Figure 8.5 and Table 8.3, further support the superior performance of RaF and SVM classifiers relative to log(VoA) and ARFI PD.

Of interest is that using the three temporal profiles of SNR, correlation, and displacement as the classifier feature set yielded higher performance than using any combination of two temporal profiles. This result suggests that echogenicity (SNR) and mechanical property (correlation and displacement) are complementary for discriminating plaque features. The complementarity of echogenicity and mechanical property is consistent with prior work showing that log(VoA), which is influenced by both SNR and correlation, better discriminates plaque components than ARFI PD alone, which

Measurement	Metric	R	RPC	CV	Bias [mm]
Average FC Thickness	ARFI PD SS	0.51	0.42	25%	0.14 (p = 0.02)
	ARFI log(VoA) BR	0.94	0.18	25%	0.64 (p = 0.01)
	ARFI log(VoA) SS	0.92	0.16	10%	0.06 (p = 0.01)
	RaF	**0.97**	0.13	8%	0.03 (p = 0.07)
	SVM	**0.97**	**0.11**	**7%**	0.00 (p = 0.82)
Minimum FC Thickness	ARFI PD SS	0.75	0.55	21.82%	0.21 (p <0.01)
	ARFI log(VoA) BR	0.74	0.56	24.00%	0.71 (p <0.01)
	ARFI log(VoA) SS	0.93	0.31	18.20%	0.22 (p = 0.01)
	RaF	0.93	0.19	**8.55%**	0.39 (p <0.01)
	SVM	**0.94**	**0.18**	8.57%	0.41 (p <0.01)
Maximum FC Thickness	ARFI PD SS	0.70	0.53	21.99%	0.18 (p = 0.05)
	ARFI log(VoA) BR	0.80	0.27	26.00%	0.37 (p = 0.01)
	ARFI log(VoA) SS	0.86	0.26	17.35%	0.07 (p = 0.06)
	RaF	0.90	0.24	**17.22%**	0.15 (p <0.01)
	SVM	**0.91**	**0.23**	17.28%	0.15 (p <0.01)

Table 8.6: Part 2 Study - Fibrous cap thickness measurement metrics from regression and Bland Altman analysis for average, minimum, and maximum thicknesses. RPC = reproducibility coefficient, CV = coefficient of variation, SS = Semi-automatically Segmented, BR = Best Reader.

predominantly reflects mechanical property.

Using temporal profiles of SNR, correlation, and displacement as the feature set, the two machine learning classifiers generally perform comparably to each other except in regard to contrasting lipid-rich-necrotic core and intraplaque hemorrhage. In this case, the SVM classifier achieved statistically significantly higher CNR, which is clinically meaningful because intraplaque hemorrhage has a higher hazard ratio for stroke (HR = 4.59) than lipid-rich necrotic core (HR = 3.00) [3]. This suggests that the SVM classifier may be the more appropriate method for widespread clinical translation, but further evaluation is needed to confirm this suggestion.

Apart from lipid-rich necrotic core and intraplaque hemorrhage, indicators of stroke risk include fibrous cap thickness. In particular, average and minimum cap thicknesses are predictive of plaque rupture potential [3, 34, 126]. These were more accurately and precisely measured by the machine learning classifiers than by the best blinded-reader and semiautomatically segmented ARFI PD or log(VoA), as shown in Table 8.3. Between the two classifiers, the SVM approach achieved slightly lower average and minimum cap thickness measurement biases.

In addition to improving delineation of plaque components that convey rupture potential, including fibrous cap thickness, the machine learning classifiers offer the important advantage of automating component classification. While a user must interpret qualitative ARFI PD and log(VoA)

values to determine plaque feature type, with potential for misinterpretation errors, the machine learning classifiers output predicted likelihood values. High likelihood predictions suggest strong confidence in component type, while low likelihood values can suggest blended components (such as the large region of combined lipid-rich necrotic core and intraplaque hemorrhage in the plaque of Figure 8.4) or uncertainty in the model prediction. This highlights an important shortcoming to the presented methods - inability to discriminate low likelihood reflecting blended components from low likelihood reflecting model uncertainty due to poor data or other corrupting factors.

By the employed methods of performance analysis, low likelihood was considered to reflect model uncertainty, which penalized classifiers that appropriately predicted low likelihood to reflect blended components. More specifically, in this study, four of the 20 evaluated plaques contained regions marked by the pathologist as being comprised of both lipid-rich necrotic core and intraplaque hemorrhage. In these regions, the plaque component spanning the greatest percent area of the region was considered as the single valid compositional element. Therefore, uncertainty between plaque components in the RaF and SVM likelihood images (reflected as blended color) was considered "incorrect" and resulted in reduced feature contrast and AUC. While the number of such cases in this study was relatively small, future work involving larger data sets will consider blended composition as a valid outcome and adjust performance metrics accordingly. Similarly, methods for discriminating likelihoods indicating blended composition from model uncertainty will be developed.

An additional factor influencing outcomes is the method of implementing and validating the machine learning classifiers. In regard to implementation, only RaF and SVM models were evaluated. Alternative classifier structures, including neural networks, may yield improved performance when training and validation set sizes grow. In regard to validation, classifier performance was evaluated using five-fold cross-validation. While this validation approach has been implemented extensively in numerous other applications [124, 117, 125], the method is prone to low variance. In the future, when more data is available, holdout and k-fold validation strategies will be implemented

8.5 Conclusion

This chapter demonstrates machine learning classifiers for fully-automated delineation of carotid plaque components conferring stroke risk. In addition to automating classification of plaque features, the machine learning classifiers yield higher feature contrast, improved sensitivity and specificity of feature detection, and more accurate and precise fibrous cap thickness and independent plaque

component area measurement than the best reader using ARFI PD or log(VoA) (presented in Chapter 7) and semi-automatic segmentation (presented in Chapter 6). Two classifiers were compared, RaF and SVM, and while the classifiers generally performed comparably, the SVM classifier achieved statistically higher contrast of intraplaque hemorrhage from lipid-rich necrotic core, suggesting that it may be the more relevant classifier for routine clinical use. In the following chapter, further analysis will be presented to improve classifier models, by using harmonic and high frequency tracking, and data acquisitions at systole and diastole.

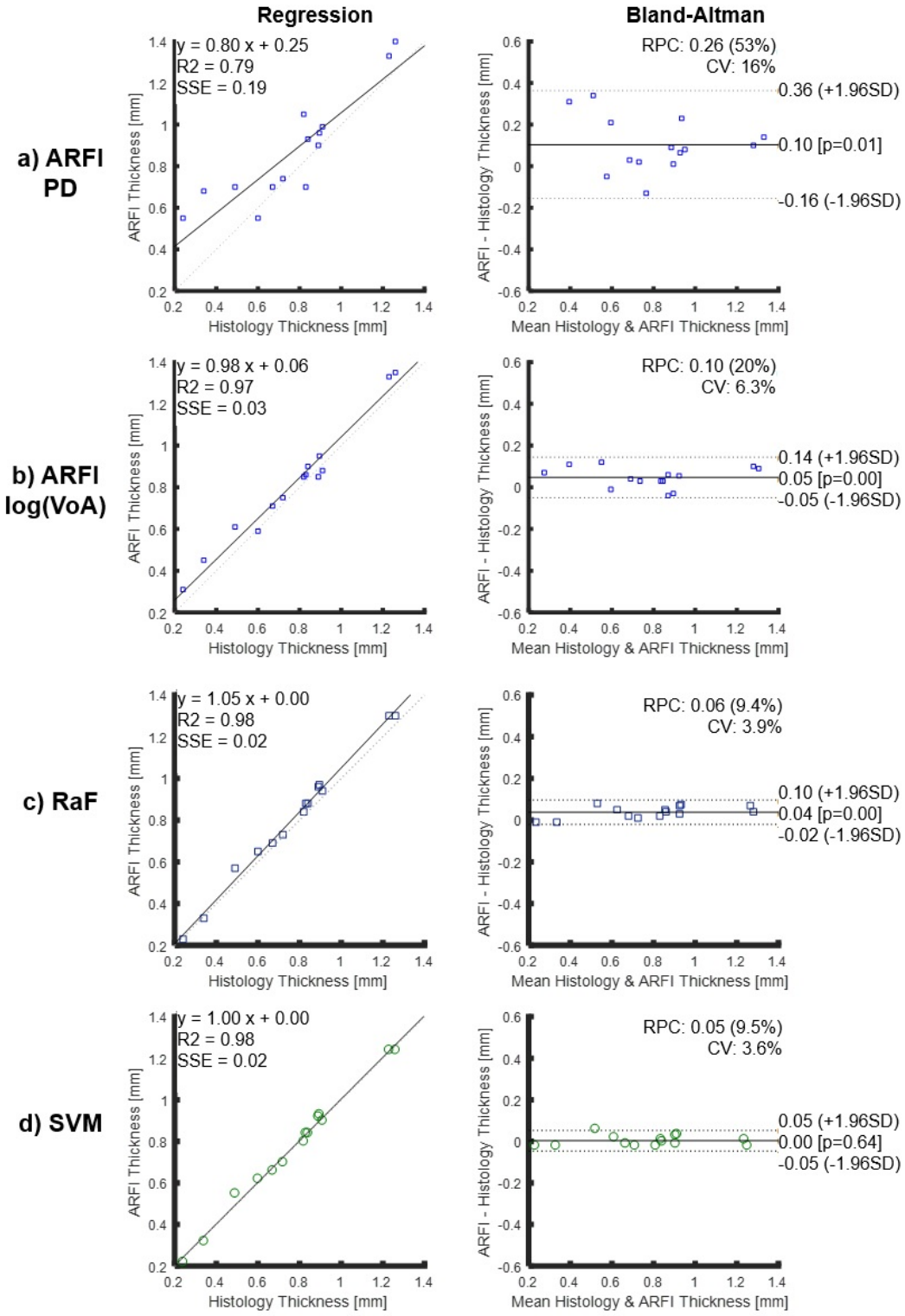

Figure 8.5: Part 1 Study - Regression and Bland-Altman plots for ARFI peak displacement, log(VoA), ML Random Forest (RaF), and ML Support Vector Machine (SVM) median FC thickness measurement.

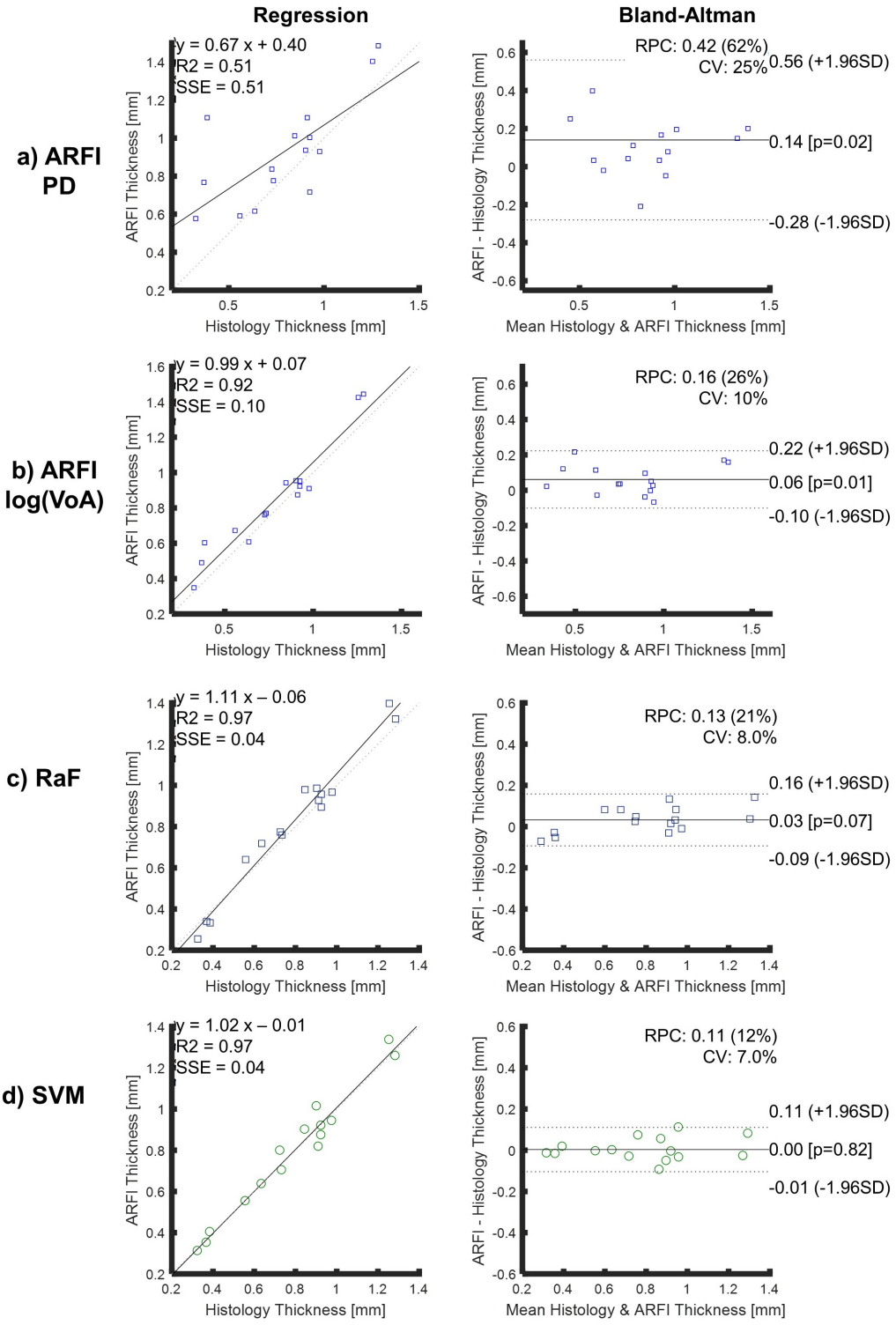

Figure 8.6: Part 2 Study - Regression and Bland-Altman plots for ARFI peak displacement, log(VoA), ML Random Forest (RaF), and ML Support Vector Machine (SVM) median FC thickness measurement.

CHAPTER 9

IMPROVING DELINEATION OF HUMAN CAROTID PLAQUE FEATURES USING HARMONIC ARFI VARIANCE OF ACCELERATION, COMBINATION OF ARFI EXCITATION POWERS, AND ACQUISITIONS AT DIASTOLE AND SYSTOLE

9.1 Introduction

Previous chapters have shown that log(VoA), an ARFI outcome parameter derived as the decadic log of the variance of the second-time derivative of displacement, differentiated LRNC, IPH, collagen (COL), and calcium (CAL) [111] and supported more accurate measurement of fibrous cap thickness than ARFI peak displacement (PD), using semi-automatic segmentation, via a blinded-reader study, and using machine learning classifiers. The purpose of this chapter is to evaluate if automatic performance for plaque feature delineation is improved by additional optimization methodologies using harmonic imaging and multiple acquisitions at diastole and systole. Specifically, this chapter will evaluate if incorporating additional information into the feature set of a machine learning classifier further improves discrimination of human carotid atherosclerotic plaque features, *in vivo*. The additional information consists of temporal profiles of displacement, CC, and SNR acquired with a 0% power (no) ARFI excitation with gating to diastole and systole, using high frequency and harmonic tracking.

Machine learning classifiers improve plaque feature detection, area and minimum fibrous cap thickness measurement, and they do so in a fully automated way, but they have another potential advantage. A machine learning model can be trained to take in more information than a human reader readily can, so this chapter evaluates if more information about the plaque could further improve carotid plaque feature detection and size measurement.

The basis for acquiring data at multiple gating points in the cardiac cycle is based on the potential use of additional information to improve component detection. Typically, ARFI data collection is gated to diastole; however, for this study, data collection were incorporated at diastole and at systole. Further, data were acquired with and without the acoustic radiation force excitation. For each of

these data collection methods, temporal profiles of displacement, signal correlation, and SNR were included as the feature set to the support vector machine classifier, which, as in the previous study, output the likelihood that each pixel was CAL, COL, LRNC and IPH.

The justification for using harmonic tracking is that it improves spatial resolution and reduces clutter relative to imaging at the corresponding fundamental frequency. The finer spatial resolution afforded by harmonic imaging could enable detection of smaller plaque features and/or more precise boundary definition by log(VoA). Clutter, which is characterized as diffuse echoes overlaying the signal of interest caused by sound reverberation between tissue layers, scattering from off-axis tissue structures, ultrasound beam distortion, returning echoes from previously transmitted pulses, and electronic noise [127], distorts displacement measurement variance, thereby impacting log(VoA). Therefore, clutter reduction with harmonic imaging could improved discrimination of plaque features by log(VoA), particularly in clutter-prone regions such as the lumen-plaque boundary where fibrous caps reside. However, a potential disadvantage to harmonic tracking is that it yields lower SNR compared to fundamental tracking at comparable frequencies. Similarly, additional relevant information could be obtained by tracking at higher fundamental frequency for greater spatial resolution, but at the cost of greater off-axis contributions.

9.2 Methods

9.2.1 Patient Recruitment

Following the methodology depicted in Chapter 6, a total of twenty patients undergoing clinically indicated CEA were recruited from UNC Hospitals. Inclusion criteria included symptomatic 50-99% Doppler-indicated stenotic plaque in the carotid artery. Patients with probable causes of stroke unrelated to the surgical carotid plaque were excluded. All procedures were approved by the institutional review board (IRB), and informed written consent was given from each study participant. After imaging, spatially-matched histology derived from the extracted plaque specimens was delineated by a trained pathologist and used as a validation standard.

9.2.2 High Frequency and Harmonic ARFI Imaging

ARFI imaging was performed in vivo using a Siemens S3000 scanner and a 9L4 transducer. ARF excitations were centered at 4.0 MHz, with harmonic tracking by pulse inversion at 8.0 MHz. ARFI tracking pulse sequences were also implemented at fundamental frequencies of 4 MHz and 8.89

MHz for comparison. Ensembles (2 reference + 1 ARF + 43 tracking pulses) were acquired in 40 lateral positions evenly spaced across an 18 mm lateral field of view for 2D imaging. ARF-induced displacements were measured using 1-D axial normalized cross-correlation (NCC) [111, 128].

9.2.3 Harmonic ARFI log(VoA) Analysis

ARFI variance of acceleration (VoA) was calculated from ARFI-induced displacement versus time profiles as the unbiased variance of the second time derivative through ensemble time calculated in 6.1. Then, the decadic log of VoA (log(VoA) was evaluated, from which contrast-to-noise ratio (CNR) between plaque components was calculated in 5.3, where μ and σ are the median and standard deviation log(VoA) within the plaque component region, segmented by a semi-automatic k-means clustering method [128], and the subscripts a and b refer to the two features being compared, i.e., CAL and COL, or LRNC and IPH, or COL and LRNC, respectively.

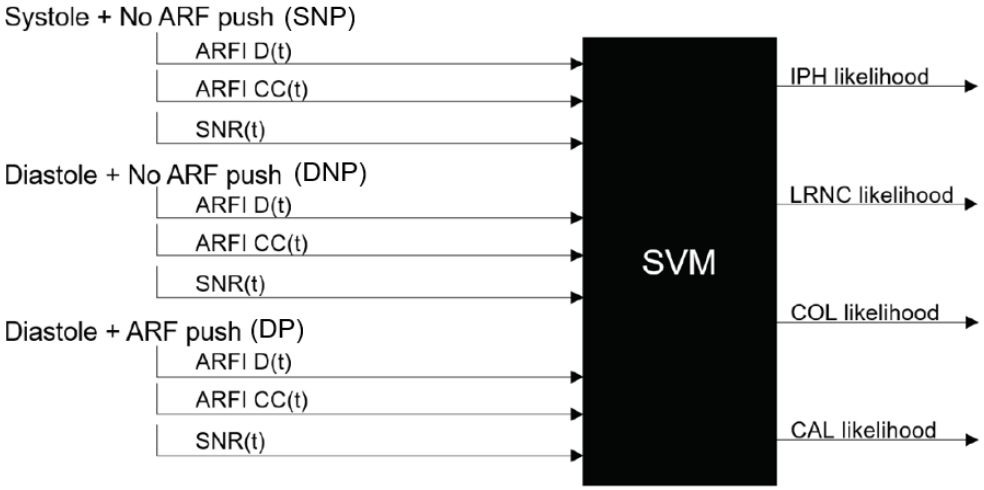

Figure 9.1: Schematic of total inputs to the support vector machines (SVM) classifier and outputs indicating plaque composition likelihood. ARFI D(t), CC(t), and SNR(t) indicate ARFI displacement, cross-correlation coefficient, and signal-to-noise ratio temporal profiles.

9.2.4 ARFI Imaging Acquisitions at Diastole and Systole

ARFI pushes were implemented at 0 (no push, or 'NP') and 70% (push, or 'P') ARFI excitation powers, and acquisitions were gated to diastole (D) and systole (S). These data sets are denoted as DP (diastole with push), DNP (diastole with no push), and SNP (systole with no push). Figure 9.1 shows a schematic of the machine learning classifier, with inputs indicated that combine acquisitions at systole and diastole, with and without push, acquired all for low frequency, high frequency, and

harmonic tracking [128].

9.2.5 Plaque Feature Classification and Analysis

The feature set of the support vector machine (SVM) classifier consisted of DP, DNP, and/or SNP. Four output classes were defined: CAL, COL, LRNC, and IPH. The classifier was trained using data acquired in plaque regions corresponding to each class, as validated by the spatially-matched histology delineated by a pathologist. Classifier performance was evaluated by 5-fold cross-validation using the histological gold-standard. 2D class likelihood maps were calculated as the compounded likelihood per pixel assigned to an RGB value per class, i.e., IPH = [255 0 0] (red), LRNC = [255 255 0] (yellow), COL = [0 255 255] (light blue), and CAL = [0 0 255] (dark blue), with blended colors (i.e. shades of green and orange) indicating predicted likelihoods between two classes.

9.3 Results

Figure 9.2 shows a type V plaque in a symptomatic male, represented in parametric images of normalized log(VoA) acquired using (i) fundamental low frequency, (ii) fundamental high frequency, and (iii) harmonic ARFI imaging. The green arrow shows better differentiation between the COL and LRNC in the harmonic case compared to both log(VoA) images at ARFI fundamental frequencies, which supports better discrimination of the fibrous cap. However, it can be observed that spatial resolution is best when using fundamental high frequency ARFI tracking. Over all examined plaques, all three acquisition methods statistically differentiated all four plaque components from each other (Wilcoxon, $P < 0.01$).

CNR	COL vs. CAL	LRNC vs. IPH	COL vs. LRNC
FL log(VoA)	1.35 ± 0.52	2.01 ± 0.29	1.95 ± 0.34
FH log(VoA)	2.88 ± 0.41	2.79 ± 0.32	1.52 ± 0.38
Harmonic log(VoA)	2.21 ± 0.33	2.58 ± 0.30	2.04 ± 0.38

Table 9.1: SVM-derived CNR results between plaque components for frequency low (FL), frequency high (FH), and harmonic ARFI log(VoA), in 20 patients.

Table 9.1 shows that harmonic log(VoA) achieved the highest CNR between COL and LRNC, consistent with the expectation that clutter reduction near the lumen-plaque boundary would improve harmonic log(VoA) performance in this region. However, away from the lumen-plaque boundary, fundamental high frequency log(VoA) achieved the highest CNR when differentiating between COL and CAL, and between LRNC and IPH.

Table 9.2 shows a comparison of CNR values between plaque components for different classifier

CNR	COL vs. CAL	LRNC vs. IPH	COL vs. LRNC
Diastole w push (DP)	1.38 ± 0.21	1.44 ± 0.18	1.45 ± 0.20
Diastole w/o push (DNP)	1.10 ± 0.19	1.12 ± 0.19	1.02 ± 0.36
Systole w/o push (SNP)	1.50 ± 0.21	1.41 ± 0.31	1.27 ± 0.30
DP + DNP	1.98 ± 0.22	2.01 ± 0.34	2.14 ± 0.32
DP + SNP	2.38 ± 0.18	2.02 ± 0.18	2.03 ± 0.31
DNP + SNP	2.12 ± 0.30	2.13 ± 0.25	2.18 ± 0.29
DP + DNP + SNP	2.96 ± 0.21	3.08 ± 0.20	2.99 ± 0.22

Table 9.2: SVM-derived CNR results between plaque components for different model input combinations in 20 patients. All aquisitions were acquired with tracking at FH (8.89 MHz).

input combinations. Combining DP, DNP, and SNR data acquisitions as the input feature set resulted in the highest CNR for CAL vs COL, IPH vs LRNC, and COL vs LRNC. Figures 9.3 and 9.4 show two type V plaques in symptomatic patients, for the feature set (DP + DNP + SNP) that yielded the highest CNRs. Both examples show high correlation between the automatic SVM segmentation and the spatially matched histology.

Figures 9.3 and 9.4 show example type V plaques in symptomatic patients, predicted likelihood maps for different combinations of gated acquisitions and spatially-matched histology delineated by the pathologist. These results visually show improvement when combining multiple acquisitions as inputs to the classifier algorithm, compared to a single acquisition input. Additionally, Tables 9.3 and 9.4 show performance metrics for detecting plaque components, and fibrous cap thickness measurement, respectively, using different input combinations for feature classification.

9.4 Discussion

These results suggest that harmonic log(VoA) is relevant to detecting fibrous cap, which could support more accurate measurement of fibrous cap thickness. This is a topic of ongoing investigation. Results suggest that for detecting calcium, the combination of harmonic and high frequency tracking at diastole with push achieved the highest AUC (0.921). For detecting diffuse collagen, the combination of harmonic and high frequency tracking at diastole with push achieved the highest AUC (0.909). For detecting fibrous cap, the combination of harmonic and high frequency tracking at diastole with push achieved the highest AUC (0.916). For detecting lipid-rich necrotic core, both harmonic at diastole with push and combination of harmonic and high frequency tracking at diastole with push achieved the highest AUC (0.943). Finally for detecting intraplaque hemorrhage, both the combination of harmonic and high frequency tracking at diastole with push, and the combination of harmonic tracking acquired at diastole with and without push with systole achieved the highest

AUC (0.942).

This study also presents limitations regarding the acquisition time and motion artifacts due to the large addition of information acquired at different tracking frequencies for multiple acquisitions during the cardiac cycle. Regarding the acquisition time, data acquired at systole without push and diastole with and without push took a total time of approximately 2 minutes and 50 seconds. During this time, the sonographer maintained the transducer positioned in a fixed location, however movement could have been possible due to the patient breathing and difficult positioning. This long acquisition time also limits the possibility of implementing this technique on a real time framework, given that the update ratio depends on both acquisitions at systole and diastole. Regarding the motion artifacts, motion due to blood flow and transducer motion generate spatial mismatch between different acquisitions. This mismatch has potential of generating error in the machine learning model because the training data will include neighboring pixels that should not correspond to specific plaque components. This limitation can be mitigated by registration techniques and by reducing the amount of acquisitions.

Future work will investigate if the combination of fundamental and harmonic ARFI imaging improves log(VoA) performance, and combining these data as inputs to our machine learning framework for automated plaque feature discrimination is also ongoing. Finally, this is an ongoing study with active data collection. Additional performance analyses will be performed with a larger number of carotid plaques.

9.5 Conclusion

This chapter shows that discrimination of carotid plaque components is improved by including high frequency and harmonic tracking, in addition to acquisitions at systole and diastole. Over all examined plaques, combining ARFI data acquired at systole and diastole, with and without ARFI excitations, as inputs to an SVM classifier achieved plaque feature CNRs that were statistically higher ($p<0.01$, Wilcoxon) than those achieved using just one of these inputs. Specifically, harmonic tracking improves contrast between COL and LRNC, and provides better AUC delineation of fibrous cap than other tracking frequencies. Further, when both harmonic and high frequency tracking are combined at diastole, the highest AUCs are obtained for differentiating CAL, COL, LRNC, and IPH. These results suggest that combining tracking frequencies and gated acquisitions improve characterization of human carotid plaque structure and composition, *in vivo*, however this approach has tradeoffs of acquisition time and artifact generation to consider for further clinical development.

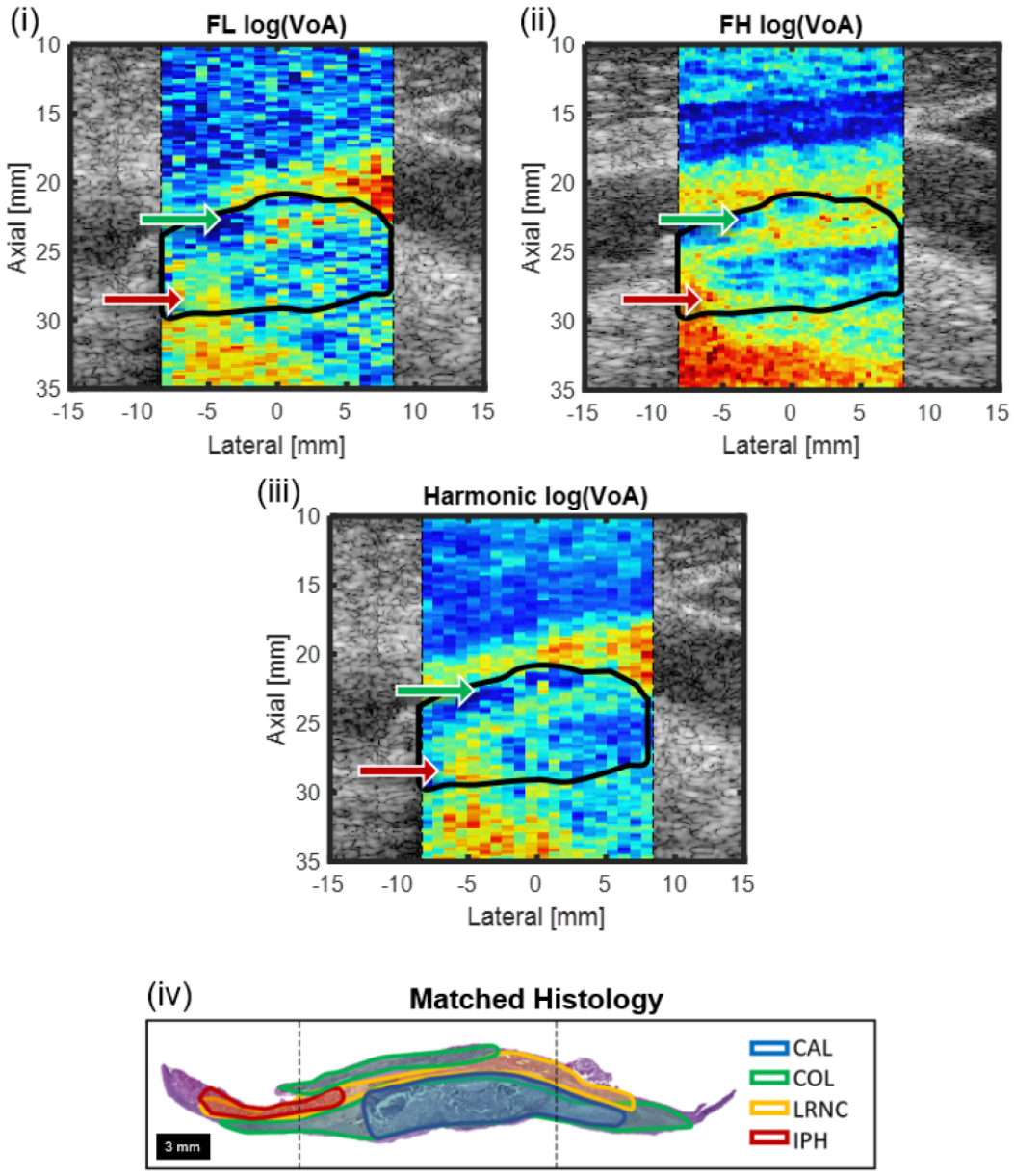

Figure 9.2: Example type V plaque in a symptomatic male, arrows show collagen (green) and intraplaque hemmorhage (red) on normalized log(VoA) images from ARFI acquisitions at (i) fundamental low frequency (FL), (ii) fundamental high frequency (FH), and (iii) harmonic (H) tracking. (iv) Matched histology delineated by the pathologist.

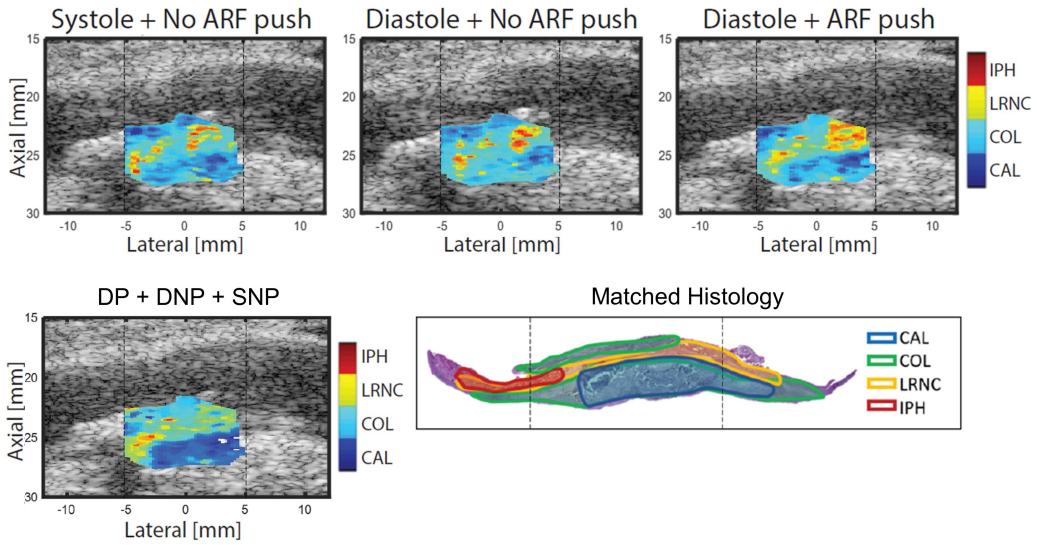

Figure 9.3: Example type V plaque in a symptomatic male, predicted likelihood maps for different combinations of gated acquisitions and spatially-matched histology delineated by the pathologist. The dashed vertical lines indicate the lateral span of ARFI imaging.

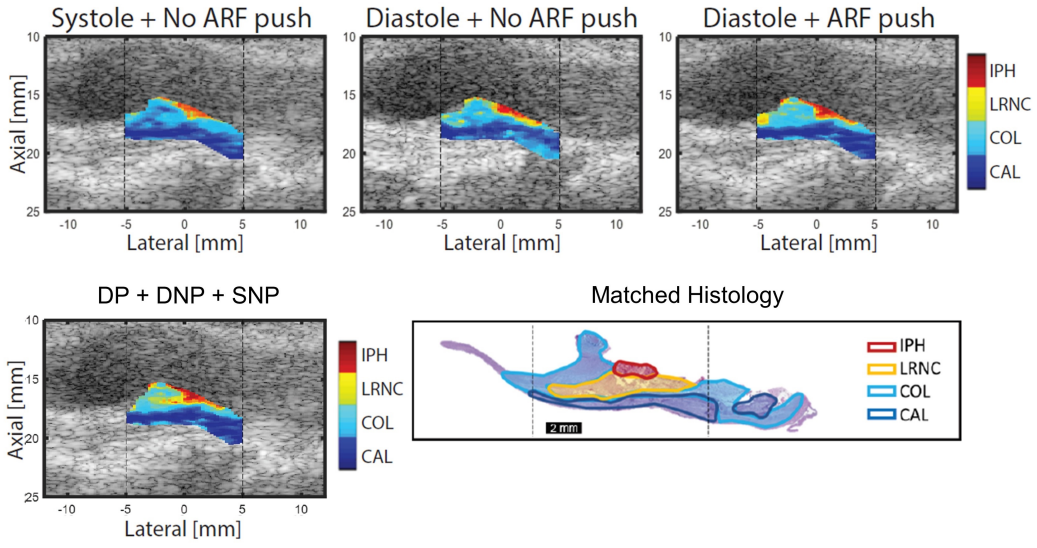

Figure 9.4: Example type V plaque in a symptomatic male, predicted likelihood maps for different combinations of gated acquisitions and spatially-matched histology delineated by the pathologist. The dashed vertical lines indicate the lateral span of ARFI imaging.

Performance	Metric	AUC	Sensitivity	Specificity
Calcium	ARFI log(VoA) BR	0.820	0.740	0.740
	SVM FH DP	0.904	**0.935**	0.941
	SVM FL DP	0.825	0.750	0.750
	SVM Harmonic DP	0.856	0.760	0.780
	SVM (FH + Harmonic) DP	**0.921**	**0.935**	**0.958**
	SVM (FH + Harmonic) DNP	0.888	0.911	0.943
	SVM (FH + Harmonic) SNP	0.859	0.902	0.910
	SVM FH (DP + DNP + SNP)	0.871	0.918	0.949
	SVM FL (DP + DNP + SNP)	0.858	0.904	0.904
	SVM Harmonic (DP + DNP + SNP)	0.862	0.908	0.926
Diffuse Collagen	ARFI log(VoA) BR	0.850	0.710	0.710
	SVM FH DP	0.899	0.857	0.759
	SVM FL DP	0.857	0.740	0.760
	SVM Harmonic DP	0.865	0.752	0.781
	SVM (FH + Harmonic) DP	**0.909**	**0.915**	0.905
	SVM (FH + Harmonic) DNP	0.878	0.870	0.905
	SVM (FH + Harmonic) SNP	0.890	0.871	0.902
	SVM FH (DP + DNP + SNP)	0.891	0.846	0.851
	SVM FL (DP + DNP + SNP)	0.832	0.850	0.901
	SVM Harmonic (DP + DNP + SNP)	0.879	0.889	**0.908**
Fibrous Cap	ARFI log(VoA) BR	0.910	0.880	0.790
	SVM FH DP	0.912	0.853	0.891
	SVM FL DP	0.855	0.802	0.802
	SVM Harmonic DP	0.912	0.880	0.820
	SVM (FH + Harmonic) DP	**0.916**	**0.926**	0.870
	SVM (FH + Harmonic) DNP	0.892	0.818	0.930
	SVM (FH + Harmonic) SNP	0.860	0.849	0.905
	SVM FH (DP + DNP + SNP)	0.902	0.914	0.916
	SVM FL (DP + DNP + SNP)	0.860	0.873	0.878
	SVM Harmonic (DP + DNP + SNP)	0.909	0.907	**0.939**
Lipid-rich Necrotic Core	ARFI log(VoA) BR	0.860	0.810	0.740
	SVM FH DP	0.938	**0.986**	0.937
	SVM FL DP	0.910	0.852	0.855
	SVM Harmonic DP	**0.943**	0.880	0.875
	SVM (FH + Harmonic) DP	**0.943**	0.981	**0.942**
	SVM (FH + Harmonic) DNP	0.905	0.846	0.904
	SVM (FH + Harmonic) SNP	0.903	0.908	0.913
	SVM FH (DP + DNP + SNP)	0.871	0.895	0.915
	SVM FL (DP + DNP + SNP)	0.896	0.908	0.908
	SVM Harmonic (DP + DNP + SNP)	0.899	0.902	0.903
Intraplaque Hemorrhage	ARFI log(VoA) BR	0.920	0.850	0.850
	SVM FH DP	0.930	0.877	0.871
	SVM FL DP	0.905	0.801	0.802
	SVM Harmonic DP	0.925	0.880	0.830
	SVM (FH + Harmonic) DP	**0.942**	0.901	0.900
	SVM (FH + Harmonic) DNP	0.872	0.909	0.905
	SVM (FH + Harmonic) SNP	0.900	0.927	0.883
	SVM FH (DP + DNP + SNP)	0.927	**0.937**	0.912
	SVM FL (DP + DNP + SNP)	0.858	0.880	0.888
	SVM Harmonic (DP + DNP + SNP)	**0.942**	0.923	**0.960**

Table 9.3: Performance metrics for detecting calcium, diffuse collagen, fibrous cap, lipid-rich necrotic core, and intraplaque hemorrhage by Support Vector Machine (SVM) input combinations.

Measurement	Metric	R	RPC	CV	Bias [mm]
Average FC Thickness	ARFI log(VoA) BR	0.94	0.18	25.00	0.64
	SVM FH DP	0.97	**0.11**	7.00	**0**
	SVM FL DP	0.90	0.15	18.41	0.5
	SVM Harmonic DP	**0.98**	**0.10**	10.21	0.22
	SVM (FH + Harmonic) DP	0.91	0.21	10.58	0.26
	SVM (FH + Harmonic) DNP	0.91	0.20	11.02	0.55
	SVM (FH + Harmonic) SNP	0.90	0.20	15.25	0.45
	SVM FH (DP + DNP + SNP)	**0.98**	**0.11**	**7.01**	**0.2**
	SVM FL (DP + DNP + SNP)	0.93	0.23	8.10	0.26
	SVM Harmonic (DP + DNP + SNP)	0.95	0.20	**6.50**	0.44
Minimum FC Thickness	ARFI log(VoA) BR	0.74	0.56	24.00	0.71
	SVM FH DP	**0.94**	0.18	**8.57**	0.41
	SVM FL DP	0.81	0.22	15.40	1.24
	SVM Harmonic DP	**0.95**	0.20	10.11	0.40
	SVM (FH + Harmonic) DP	0.90	0.19	12.54	**0.23**
	SVM (FH + Harmonic) DNP	0.84	0.18	12.60	0.95
	SVM (FH + Harmonic) SNP	0.82	0.18	15.95	1.08
	SVM FH (DP + DNP + SNP)	0.85	**0.17**	10.56	0.36
	SVM FL (DP + DNP + SNP)	0.80	0.20	16.64	0.48
	SVM Harmonic (DP + DNP + SNP)	0.85	**0.16**	**8.50**	**0.32**
Maximum FC Thickness	ARFI log(VoA) BR	0.80	0.27	26.00	0.37
	SVM FH DP	0.91	0.23	17.28	0.15
	SVM FL DP	0.78	0.32	25.90	0.42
	SVM Harmonic DP	**0.93**	**0.22**	18.20	0.16
	SVM (FH + Harmonic) DP	0.82	0.25	15.56	**0.12**
	SVM (FH + Harmonic) DNP	0.80	0.29	18.52	0.14
	SVM (FH + Harmonic) SNP	0.75	0.28	18.60	0.22
	SVM FH (DP + DNP + SNP)	0.88	**0.20**	**14.02**	**0.12**
	SVM FL (DP + DNP + SNP)	0.80	0.28	18.98	0.25
	SVM Harmonic (DP + DNP + SNP)	0.89	**0.20**	**12.80**	**0.11**

Table 9.4: Fibrous cap thickness measurement metrics from regression and Bland Altman analysis by Support Vector Machine (SVM) input combinations. RPC = reproducibility coefficient, CV = coefficient of variation.

CHAPTER 10

CONCLUSIONS AND FUTURE WORK

10.1 Conclusions

The results presented in this dissertation support the hypothesis that enhanced noninvasive ARFI ultrasound methods improve discrimination of CAL, COL, TRFC, LRNC, and IPH in human carotid atherosclerotic plaques *in vivo*, relative to ARFI PD.

First, it was shown that the decadic logarithm of the variance of acceleration, or log(VoA), improved *in vivo* carotid atherosclerotic plaque feature delineation relative to ARFI PD. Although log(VoA) is influenced by both CC and SNR, evaluating CC alone or SNR alone did not differentiate IPH, LRNC, COL, and CAL as well as log(VoA).

Second, it was demonstrated that ARFI log(VoA) improved fibrous cap thickness and component area measurement in comparison to ARFI PD. In twenty human carotid plaques, trained blinded readers achieved better performance when delineating plaque composition when using log(VoA) images than when using ARFI PD. Overall, these results suggest that ARFI-based imaging, in particular the log(VoA) parameter, is relevant to delineating carotid plaque structure and composition for vulnerable carotid plaque detection.

Third, it was shown that machine learning classifiers not only automate, but also improve, the sensitivity and specificity of plaque feature detection over trained blinded readers. Machine learning classifiers enable incorporation of multiple ARFI data forms, which reduced variability and improved sensitivity and specificity for identifying independent plaque components.

Finally, automatic plaque delineation was shown to be improved by including high frequency and harmonic tracking as well as acquisitions at systole and diastole. Over all examined plaques, combinations of different acquisitions as inputs to an SVM classifier achieved plaque feature differentiation performances that were statistically higher than those achieved with one acquisition type.

10.2 Future Work

Future work will include more patients to determine if ARFI-derived carotid plaque structure and composition is related to symptoms such as amaurosis fugax, transient ischemic attack or stroke. Due to the small number of patients enrolled in this study, it was difficult to assess the differences between plaques from symptomatic and asymptomatic patients. Improving the sensitivity of noninvasive imaging to dangerous asymptomatic atherosclerosis is regarded as a relevant challenge in the medical community due to evidence suggesting CEA may not be the best intervention strategy for asymptomatic disease. Therefore, future ARFI studies should assess asymptomatic patients to determine what additional information can be provided by this approach.

Additionally, with more available patient data, further algorithm testing strategies including holdout and k-fold validation could be implemented. Alternative classifier structures, including neural networks, may yield improved performance when training and validation set sizes grow.

Finally, the next step to establishing ARFI as a clinically relevant tool for assessing carotid plaque will likely be prospective clinical trials that correlate ARFI-derived plaque signatures to future ischemic events. While it was necessary to utilize CEA patients in this dissertation to validate ARFI's capability of detecting plaque features, these patients represent an ideal scenario for imaging because plaques in these patients are usually highly advanced and features are large. For ARFI to make a broader impact on clinical care, it must be effective in asymptomatic patients and patients with much lower stenosis levels than were imaged in this CEA study.

While there are still challenges for establishing ARFI imaging as a clinical tool for stroke risk prediction, the research presented in this dissertation suggests that ARFI-based imaging is efficacious for characterizing plaque structure and composition, thereby identifying plaque components that confer risk for stroke. Potential for extension to other peripheral arteries is relevant for future work.

APPENDIX A

CEA PATIENT CHARACTERISTICS

A.1 Summary

The studies reported in this dissertation encompass different patient characteristics that may give rise to differences in the clinical outcome. Therefore, it is paramount to evaluate the inclusion of different patient groups in these studies and the possible effect size variation generated in the outcomes.

Appendix 1 assessed differences in the 2 study cohorts assessed in the present dissertation. CEA Study Part I encompasses 20 carotid samples obtained (after exclusions) from 25 CEA patients scanned between 2012 and 2014. CEA Study Part II encompasses 20 carotid samples obtained (after exclusions) from 21 CEA patients scanned between 2019 and 2021.

Here, plaque component areas measured from histology, considered as the ground truth in this study, are calculated for calcium, lipid-rich necrotic core, fibrous cap, and intraplaque hemorrhage. Differences in age and gender are shown below and do not indicate significant differences (Wilcoxon, $p < 0.05$) between cohorts.

A.2 CEA Study Part I

A.2.1 Age

Patient stratification by age is shown in Figure A.1.

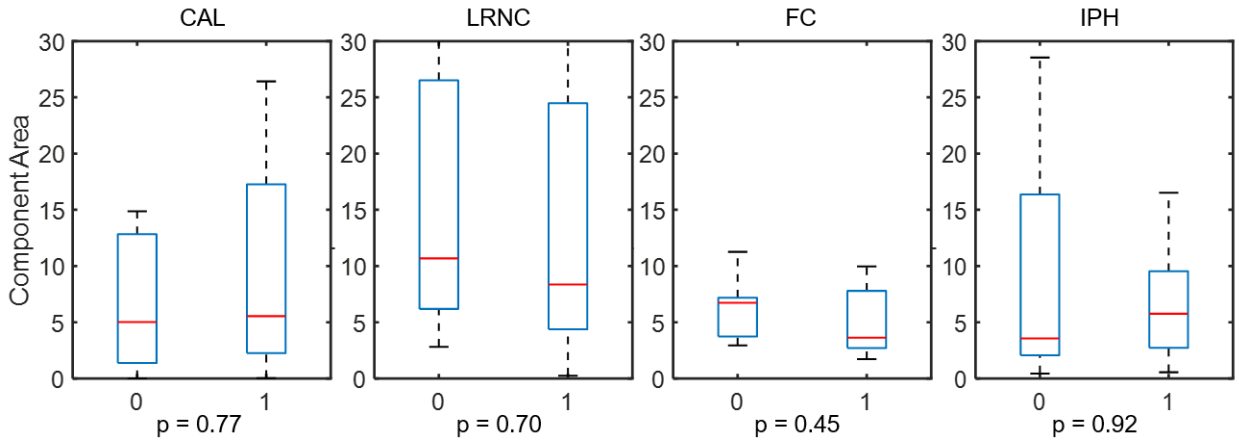

Figure A.1: Component areas for calcium, lipid-rich necrotic core, fibrous cap, and intraplaque hemorrhage. 0 = Age < 60 years old, 1 = Age > 60 years old.

A.2.2 Gender

Patient stratification by gender is shown in Figure A.2.

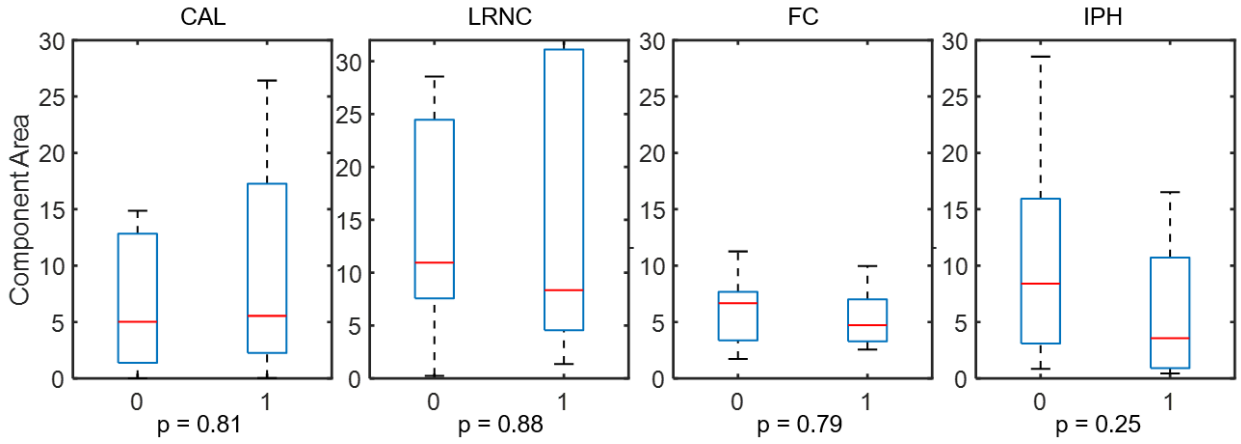

Figure A.2: Component areas for calcium, lipid-rich necrotic core, fibrous cap, and intraplaque hemorrhage. 0 = Male, 1 = Female

A.3 CEA Study Part II

A.3.1 Age

Patient stratification by age is shown in Figure A.3.

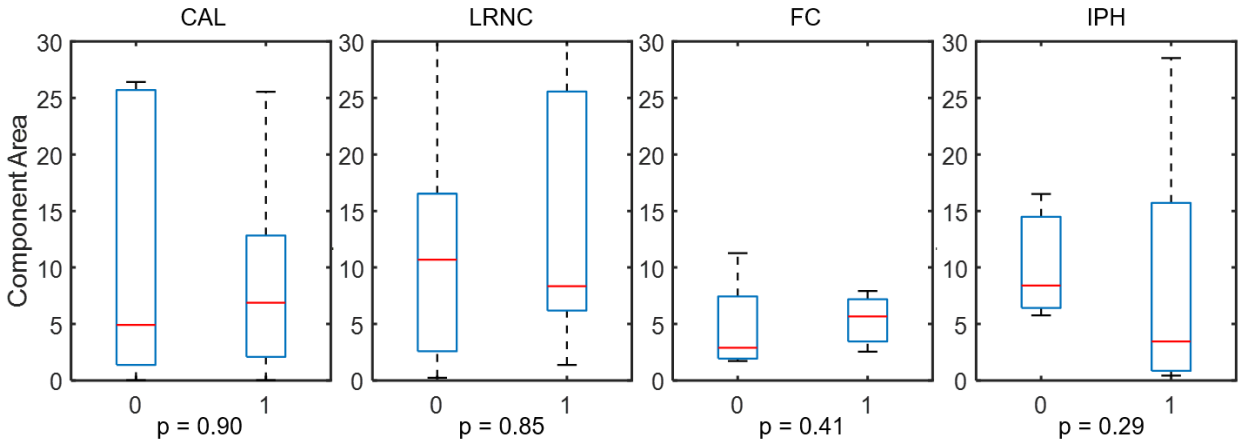

Figure A.3: Component areas for calcium, lipid-rich necrotic core, fibrous cap, and intraplaque hemorrhage. 0 = Age $<$ 60 years old, 1 = Age $>$ 60 years old.

A.3.2 Gender

Patient stratification by gender is shown in Figure A.4.

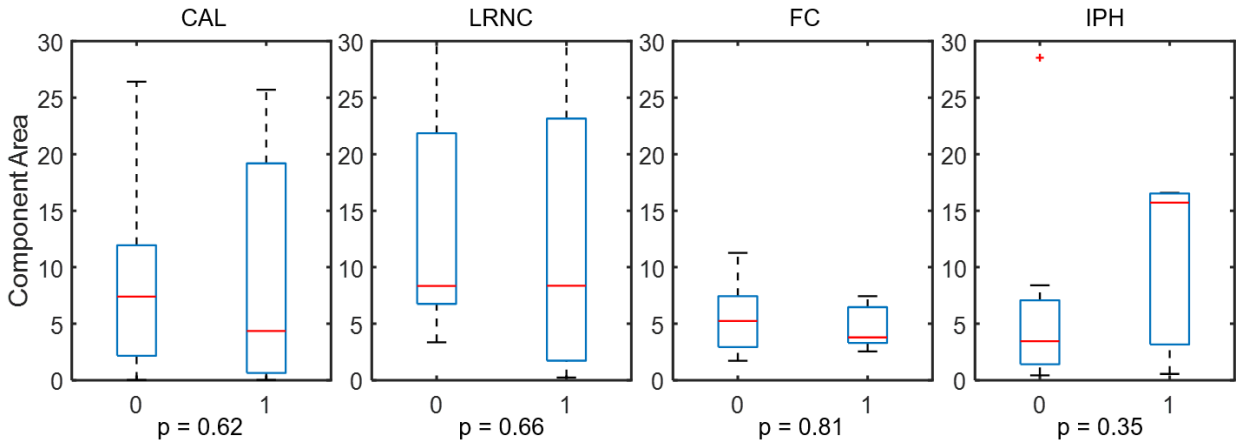

Figure A.4: Component areas for calcium, lipid-rich necrotic core, fibrous cap, and intraplaque hemorrhage. 0 = Male, 1 = Female

APPENDIX B

DIFFERENTIATING MALIGNANT FROM BENIGN BREAST MASSES USING VISR-ASSESSED MECHANICAL ANISOTROPY

B.1 Introduction

In this appendix, *in vivo* Viscoelastic Response (VisR) ultrasound was implemented to assess the diagnostic relevance of mechanical anisotropy compared against biopsy findings. VisR relative elasticity (RE), relative viscosity (RV), and peak displacement (PD) were measured for each transducer orientation, and fit to a sinusoid by least-squares minimization. The ratio of the maximum to the minimum parameter value was calculated to reflect the degree of anisotropy (DoA). DoAs by PD, RE, and RV were statistically significantly greater in background than in lesion for all malignant cases but statistically significantly smaller in background than in lesion for all benign cases (Wilcoxon, $p < 0.05$). Additionally, differences between lesion and background integrated over angle by RE, RV and PD were statistically significantly different (Wilcoxon, $p < 0.05$) for malignant and benign lesions across all examined patients. These results suggest that VisR-derived mechanical anisotropy assessment could be diagnostically relevant for discriminating malignant from benign breast lesions.

B.2 Background

The main objective of breast cancer screening is to detect early-stage cancer, or precancerous lesions, at a time before symptoms emerge and when treatment is likely to be successful. Screening is beneficial when it averts progression of disease, but adverse effects to patients may result downstream from false positives. The current screening standard in the US is digital mammography, with sensitivity reported in the range of 0.40 to 0.85 [129], and a positive predictive value of 0.31 [130]. Sensitivity is improved by augmenting mammography with MRI and B-Mode ultrasound, but false positive rates also increase [131].

In addition to the previous clinical standards, studies have also shown that mechanical properties of breast tissue can be used for cancer detection, with both elasticity [132, 133, 134, 135] [4-7] and viscosity [136, 137, 138] demonstrated for discriminating malignant from benign lesions. Clinical studies have shown that the combination of B-Mode and compression elastography have higher performance (sensitivity: 0.87, specificity: 0.90), than B-Mode alone (sensitivity 0.80, specificity: 0.88) and compression elastography alone (sensitivity: 0.80, specificity: 0.81) [139, 140, 141]. These

methods, however, are affected by the anisotropic behavior of breast tissue that is not captured when only performing a single 2D acquisition.

In particular to this study, tissue anisotropy in breast tumors has been shown to correlate with core biopsy result and tumor grade, with large cancers significantly more anisotropic than small cancers [142]. Previous studies have acquired strain and shear wave speed data at both radial and anti-radial locations relative to the lesion and shown correlation with malignancy [142, 143, 144]. However, a major shortcoming of these studies is the lack of alignment with the tissue's dominant direction of elasticity or viscosity, which may result in anisotropy measures that do not reflect the tissue's true degree of mechanical anisotropy. Further, while both MRI and ultrasound can be used to measure these biomarkers, ultrasound's cost effectiveness and ease of implementation render it an efficient platform to pursue.

Our research group has been developing a new ultrasound-based breast-screening tool to augment mammography, VisR imaging. In our previous study [145] in 9 women with BIRADS-4 or -5 breast lesions, VisR-derived mechanical DoA was greater in the surrounding tissue background than in the lesion for all malignant cases but smaller in the background than in the lesion for all benign cases. These results suggested that lesion-to-background DoA assessment by VisR could be diagnostically relevant to discriminating malignant from benign breast lesions. In this study, we expand our assessment to 37 women and systematically evaluate the diagnostic relevance of VisR anisotropy-derived parameters.

B.3 Methods

B.3.1 Patient Recruitment

This study imaged 37 breast lesions (10 malignant, 27 benign) with BIRADS-4 or -5 ratings after standard screening imaging in vivo in women. Research subjects were recruited and imaging in the Breast Imaging Division of the University of North Carolina Hospitals, with IRB approval and signed consent.

After imaging, the evaluated lesions underwent clinically indicated biopsy with histological evaluation for identification of malignancy status. Exclusion criteria for this study included the following: 1) Incomplete data acquisition (N = 3), 2) No presence of mass (N = 2), 3) inconclusive histological evaluation (N = 2). After exclusions, this study analyzed 30 breast lesions (9 malignant,

21 benign), from these cohort we also further assess lesions identified as fibroadenomas (N = 9) vs carcinomas (N = 9).

B.3.2 Viscoelastic Response (VisR) imaging

Raw RF data were acquired using a Siemens S3000 Helix research system using a 9L4 transducer. To the transducer, a gyroscope was attached to guide manual rotation for data acquisitions at 0°, 30°, 60°, and 90° concentric orientations (Figure B.1).

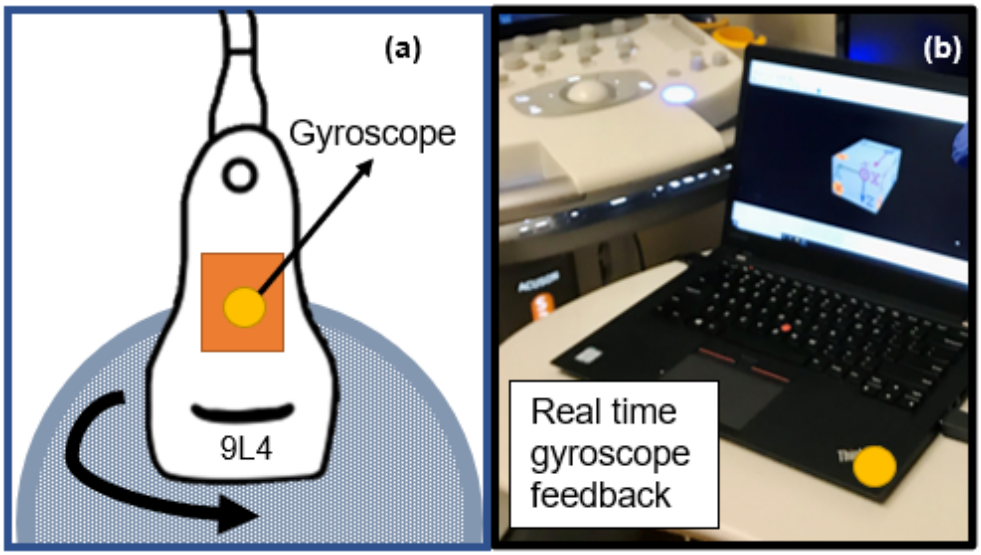

Figure B.1: Schematic of experimental setup: (a) 9L4 transducer attached to a gyroscope that is rotated from an initial 0° position to 30°, 60°, and 90° concentric locations. (b) A real-time gyroscope feedback allows concentric rotation and positioning of the transducer.

VisR ensembles consisted of two reference pulses, two acoustic radiation force (ARF) impulses, and 43 tracking lines. The two ARF impulses were each 300 cycles (71 μs) in duration. The center frequency and focal configuration of the ARF impulses were 4.21 MHz and F/1.5, respectively. The impulses were separated by 8 tracking pulses (tARF = 0.70 ms) and followed by 43 additional tracking pulses (3.74 ms). The tracking and reference pulses were conventional two-cycle A-lines at a center frequency of 6.15 MHz and pulse repetition frequency of 11.5 kHz. An F/1.5 focal configuration on transmit and dynamic focusing and aperture growth on receive were used for the reference and tracking pulses. VisR ensembles (reference + ARF + tracking pulses) were acquired in 40 lateral positions evenly spaced across a 2-cm lateral field of view for 2D imaging.

VisR displacements were measured using one dimensional axial NCC [91]. The obtained displacement profiles were then fit to the mass-spring-damper (MSD) model using a custom C++

implementation of the Nelder-Mead non-linear least-squares minimization [146, 147]. VisR depth correction was applied to VisR relative elasticity and relative viscosity parameters, and VisR elasticity correction was applied to VisR relative viscosity results following the method in [148].

B.3.3 Anisotropy Calculation

Figure B.2 includes a flowchart of the present methodology. B-Mode, VisR peak displacement (PD), relative elasticity (RE), and relative viscosity (RV) were measured in the lesion and also in the background surrounding tissue, for each transducer orientation. These values were assessed for malignancy differentiation through the median values from all acquisition angles (Wilcoxon-Ranksum test). Additionally, these parametric values were fit to a sinusoid by least-squares minimization, with extrapolation to 360°. Degree of anisotropy (DoA) was calculated as the ratio of the interpolated maximum to minimum parameter values. Finally, lesion DoA (LDoA), and surrounding tissue DoA (SDoA) were also assessed and combined as log(LDoA/SDoA) for each parameter and compared between malignant and benign masses.

Assessment was performed first using a statistical Wilcoxon-Ranksum test to identify significancy when differentiating benign vs. malignant masses. When combining LDoA and SDoA into log(LDoA/SDoA), a performance analysis was implemented to assess the sensitivity and specificity of malignancy detection using the Younden's index as the values that maximized the area under the curve (AUC) by calculating the receiver operating characteristic (ROC) curves, using the pathology outcomes as the validation standard.

B.4 Results

For a representative invasive ductal carcinoma from an 80-year-old female, B-Mode images are shown in Figure B.3(a), acquired at 0°, 30°, 60°, and 90° concentric transducer rotations. Regions of interest are indicated for the lesion (blue) and its background surrounding tissue (yellow) for each position. VisR peak displacement values derived from the segmented regions are shown in Figure B.3(b), where a sinusoid by least-squares minimization, with extrapolation to 360° is also shown in black for both regions. Table B.1 depicts the median and standard deviation values calculated from all four concentric transducer rotations for all patients. P-values indicate that B-Mode and VisR PD, RE, and RV independent parametric amplitudes don't provide statistically significant differentiation between benign vs. malignant masses, and fibroadenomas vs. carcinomas.

Figure B.4 shows two breast mass examples from an 80-year-old female with an invasive ductal

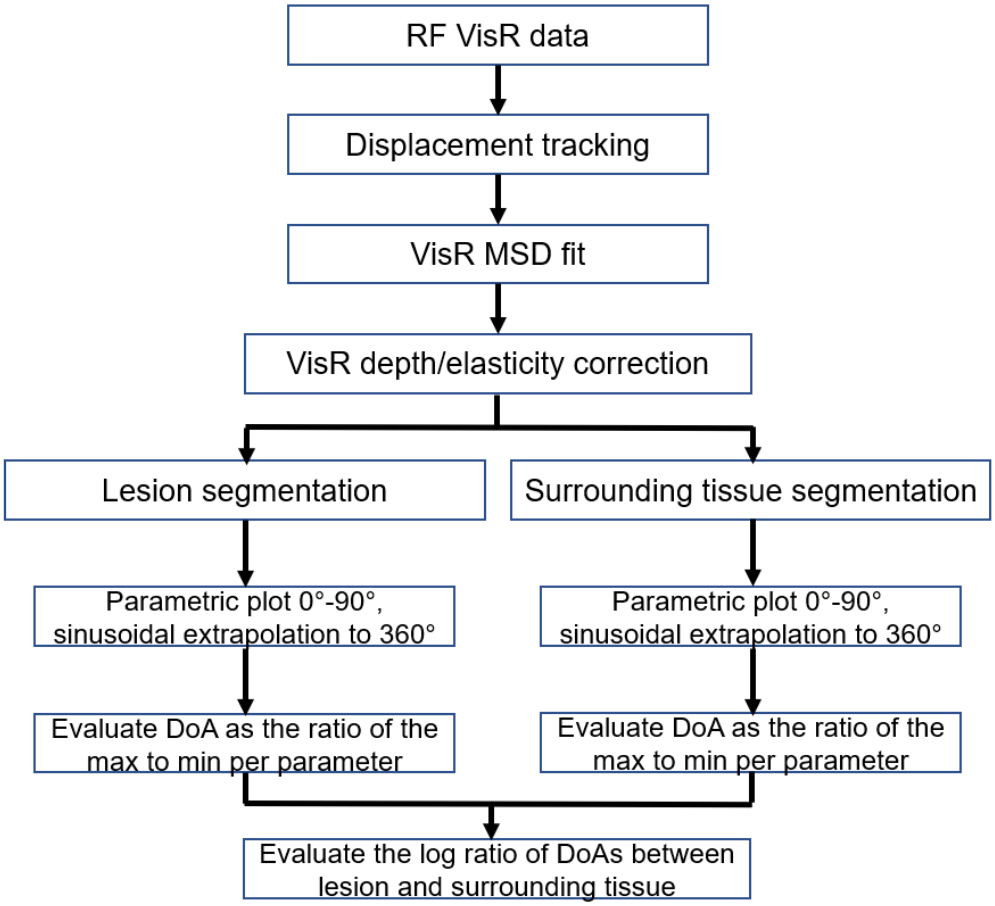

Figure B.2: Flow chart of the parameter evaluation, starting with RF VisR data acquisition and finishing on the evaluation of log(LDoa/SDoA).

carcinoma, and a 50-year-old female with a fibroadenoma. From top row to bottom row, B-Mode, VisR PD, RE, and RV are calculated for the lesion and its surrounding tissue. DoA is also calculated per parameter for the lesion (LDoA) and its surrounding tissue (SDoA), as the ratio of the maximum to minimum parametric sinusoidal fitted values. DoAs calculated from the segmented regions in B-Mode indicated isotropic behavior for both carcinoma (LDoA = 1.02, SDoA = 1.02), and fibroadenoma (LDoA = 1.04, SDoA = 1.08). DoA values derived from all VisR parameters indicate anisotropic behavior in both lesion and surrounding media. For VisR PD, in the carcinoma the lesion has a lower DoA than the surrounding tissue (LDoA = 1.20, SDoA = 1.95), whereas in the fibroadenoma, the lesion has a higher DoA than the surrounding tissue (LDoA = 1.71, SDoA = 1.54). For VisR RE, in the carcinoma the lesion also has a lower DoA than the surrounding tissue (LDoA = 1.23, SDoA = 1.67), whereas in the fibroadenoma, the lesion has a higher DoA than the

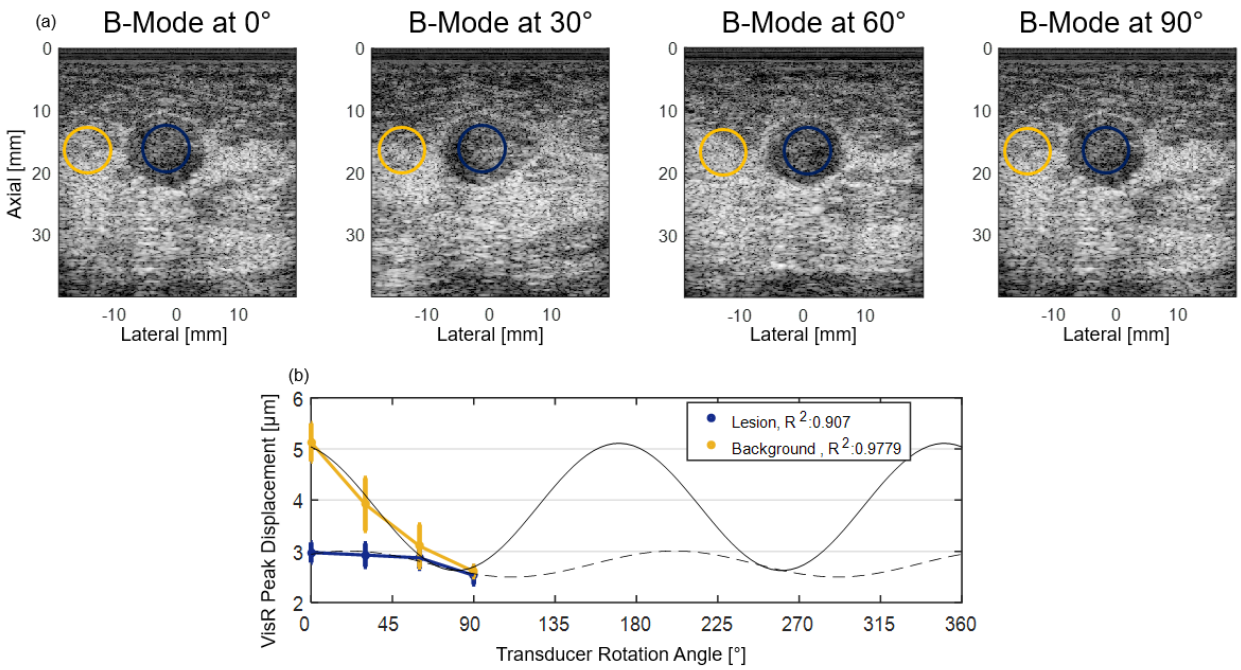

Figure B.3: (a) B-Mode images acquired at 0°, 30°, 60°, and 90° concentric rotations indicating mass (blue) and surrounding tissue (yellow). (b) VisR peak displacement calculated on each location with a sinusoidal fit extrapolated to 360°.

	Benign (N = 21)		Malignant (N = 9)		p-value	Fibroadenoma (N = 9)		Carcinoma (N= 9)		p-value
B-Mode	3.706	(0.255)	3.284	(0.237)	0.556	3.843	(0.235)	3.363	(0.225)	0.601
VisR PD	3.184	(1.67)	2.879	(0.713)	0.186	3.993	(2.246)	2.577	(0.522)	0.164
VisR RE	53.191	(8.923)	78.45	(35.975)	0.113	64.574	(12.009)	82.693	(34.584)	0.199
VisR RV	78.416	(17.426)	91.719	(37.522)	0.208	76.005	(16.625)	86.477	(35.037)	0.193

Table B.1: B-Mode, VisR peak displacement, relative elasticity, and relative viscosity amplitudes for both lesion and its surrounding tissue from (a) benign vs. malignant masses, and (b) fibroadenomas vs. carcinomas, p-value from Wilcoxon-Ranksum test.

surrounding tissue (LDoA = 2.96, SDoA = 2.91). Finally for VisR RV, the previous trend repeats where in the carcinoma the lesion has a lower DoA than the surrounding tissue (LDoA = 1.68, SDoA = 1.94), whereas in the fibroadenoma, the lesion has a higher DoA than the surrounding tissue (LDoA = 2.91, SDoA = 1.76).

Figure B.5 illustrates the median LDoA (blue) and SDoA (yellow) values per mass for all patients (N = 30), from top row to bottom row, derived from B-Mode, VisR PD, RE, and RV. It can be observed that B-Mode results are on average 1, indicating isotropy in B-Mode property. Additionally, for all VisR derived parameters, in malignant cases LDoA is lower than SDoA, whereas in benign cases LDoA is higher than SDoA. Figure 6 combines LDoA and SDoA in a logarithmic ratio to further

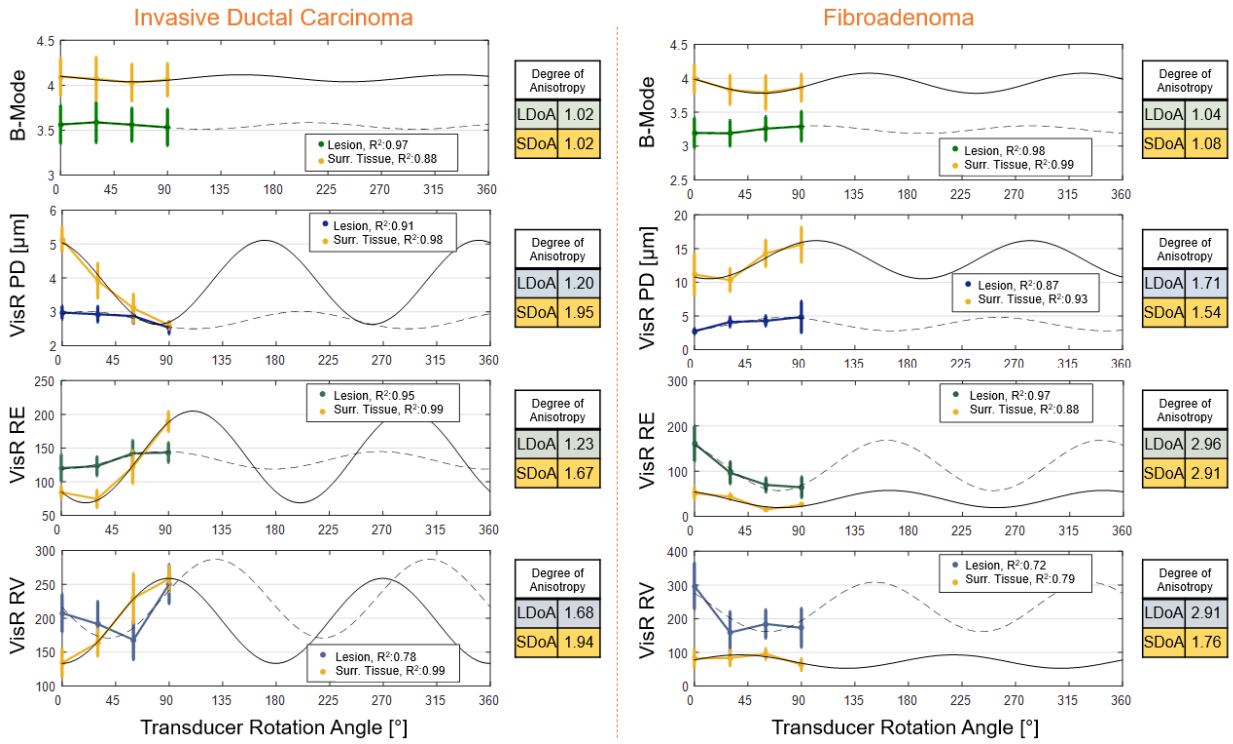

Figure B.4: Example invasive ductal carcinoma (left) and fibroadenoma (right) BIRADS-5 masses. Lesion and surrounding tissue parameters are calculated from B-Mode, VisR peak displacement, relative elasticity, and relative viscosity. Degree of Anisotropy is calculated from both lesion and surrounding tissue as the ratio of the interpolated maximum to minimum parameter values.

merge mechanical anisotropy behaviors in both lesion and its surrounding tissue. Figure B.6(a) illustrates malignant vs. benign values for B-Mode, VisR PD, RE, and RV-derived log(LDoA/SDoA), with statistical significance (Wilcoxon, $p < 0.01$) achieved only for VisR PD, RE, and RV. Figure B.6(b) illustrates carcinoma vs. fibroadenoma values for B-Mode, VisR PD, RE, and RV-derived log(LDoA/SDoA), with statistical significance (Wilcoxon, $p < 0.01$) achieved also only for VisR PD, RE, and RV.

	Malignant vs. Benign				Carcinoma vs. Fibroadenoma			
	B-Mode	VisR PD	VisR RE	VisR RV	B-Mode	VisR PD	VisR RE	VisR RV
AUC	0.6	0.93	0.96	0.97	0.54	0.92	0.98	0.96
Sensitivity	0.33	1	0.95	0.95	0.33	1	0.89	1
Specificity	0.89	0.78	0.89	0.89	0.88	0.75	1	0.88

Table B.2: Performance metrics of log(LDoA/SDoA) calculated from B-Mode, VisR peak displacement (PD), relative elasticity (RE), and relative viscosity (RV), comparing malignant vs. benign masses, and carcinomas vs. fibroadenomas.

Table B.2 reports ROC curve results for detecting (a) malignant vs. benign masses, and (b)

carcinomas vs. fibroadenomas, with performance outcomes of AUC, sensitivity and specificity. For differentiating malignant vs. benign masses, VisR RE and RV achieved the highest AUCs of 0.96 and 0.97, respectively, followed by VisR PD (0.93), and finally B-Mode (0.60). For differentiating carcinomas vs. fibroadenomas, VisR RE and RV achieved the highest AUCs of 0.98 and 0.96, respectively, followed by VisR PD (0.92), and B-Mode (0.54).

B.5 Discussion

The in vivo breast lesion and surrounding tissue images shown in Figures B.3 and B.4 quantitatively demonstrate that breast tissue presents a mechanically anisotropic behavior that can be characterized by the proposed method of concentric transducer rotations with a sinusoidal fit. Quantitative evaluations of parameter amplitudes without considering angle effects, shown in Table B.1, and AUC analyses of sensitivity and specificity of log(LDoA/SDoA), shown in Table B.2, further support the superior performance of the combination of lesion and surrounding tissue DoA relative to angle-independent B-Mode and VisR amplitudes.

Of interest is that using two regions of interest in tissue, i.e., lesion and its surrounding tissue, yielded higher performance than using the lesion region independently, where no statistically significant difference was found between malignant and benign masses. These results suggest that mechanical anisotropy both in the lesions and its surrounding tissue are complementary for identifying malignancy. The complementarity of the lesion and surrounding tissue behavior is consistent with prior MRI work showing that biological malignancy changes in structure and composition are not only present in the mass but also in the neighboring tissue.

Using VisR-derived log(LDoA/SDoA) ratios of PD, RE, and RV for parametric differentiation between malignant vs. benign masses generally perform comparably to each other via AUC analysis. In the case of comparing carcinomas vs. fibroadenomas, VisR-derived log(LDoA/SDoA) ratios maintain a similar performance, with AUC > 0.91, sensitivity > 0.88, and specificity > 0.74. This suggests that elasticity and viscosity-derived anisotropy from lesion and surrounding tissue is relevant for identifying carcinomas in particular to fibroadenomas, but a bigger cohort study is needed to confirm this suggestion.

In addition to improving detection of malignant vs. benign breast masses, the present methodology offers the important advantage of characterizing anisotropic behavior. While previous studies characterized anisotropy by acquiring images at two perpendicular locations, being radial and

anti-radial planes, or long/short axis, our methodology relies on four concentric data acquisitions guided by a gyroscope, followed by a sinusoidal fit extrapolated to 360. This approach allows identify the true degree of mechanical anisotropy, reducing bias from transducer positioning and tissue heterogeneities.

A limitation of this pilot study is the cohort size that disabled further data comparison between malignant and benign mass subtypes, and only enabled comparison between fibroadenomas and carcinomas. Future work involving larger data sets will consider benign subcategories such as necrosis, galactocele, and sclerosing adenosis, and malignant subcategories such as ductal carcinoma in situ and lobular carcinoma in situ, inflammatory, and triple negative breast cancer.

An additional factor influencing outcomes is the method of implementing the concentric acquisitions. While the sonographer was trained in breast ultrasound imaging, rotation of the transducer in a non-planar surface increased difficulty when maintaining a concentric rotation. Bias was reduced by using a real-time gyroscope feedback, but positioning error was still present. In the future, application of this technique using a 2D matrix array transducer for 3D volume acquisitions will minimize positioning bias.

B.6 Conclusion

This work demonstrates the potential of the VisR-derived degree of anisotropy to improve in vivo breast mass differentiation relative to conventional imaging. These results suggest that VisR-derived lesion-to-background mechanical anisotropy assessment is relevant to differentiating malignant from benign lesions in women with BIRADS-4 or -5 masses, *in vivo*.

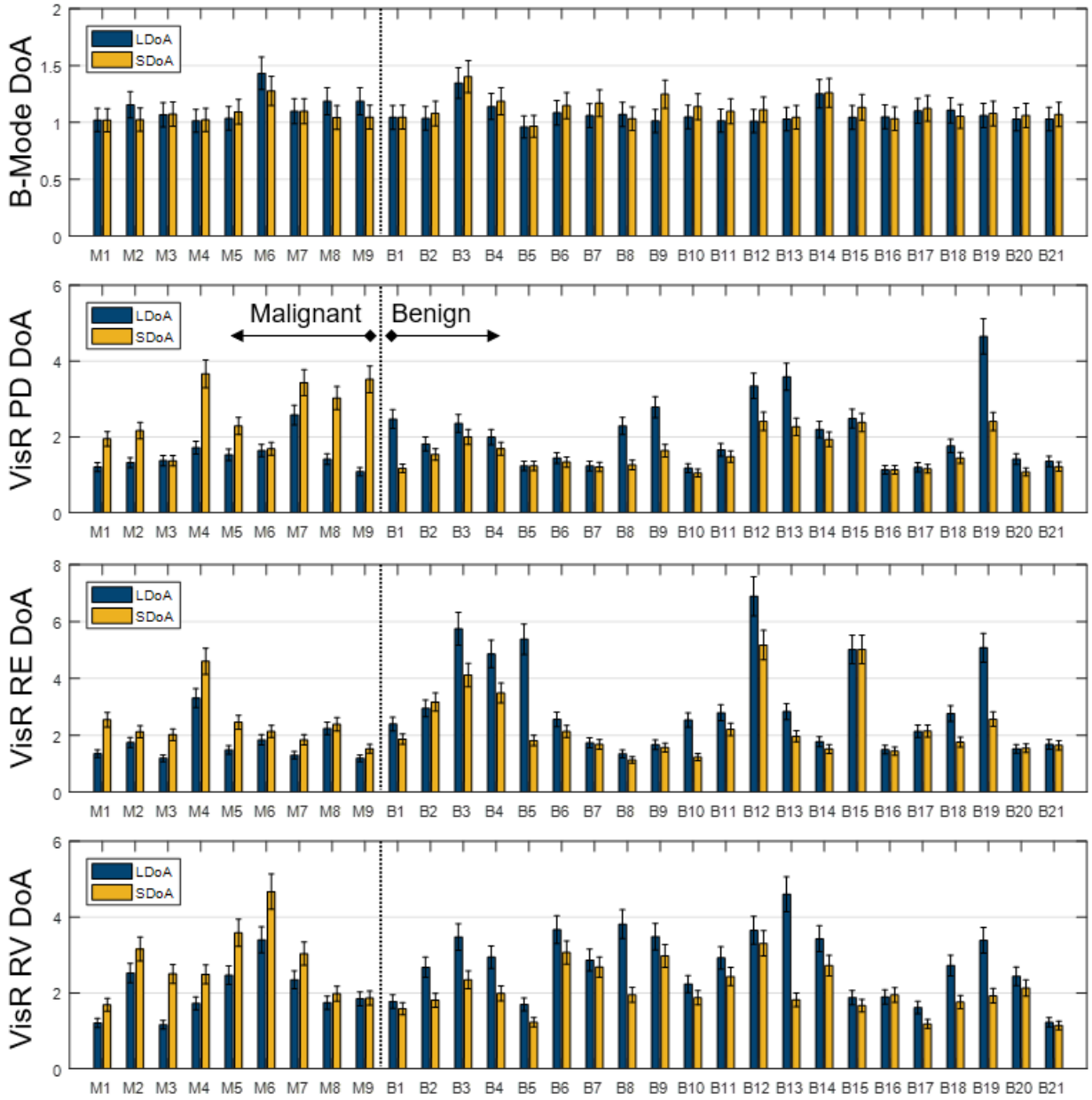

Figure B.5: Degree of anisotropy values (DoA) for both lesion (LDoA) and surrounding tissue (SDoA) for B-Mode, VisR peak displacement, relative elasticity, and relative viscosity for all malignant and benign masses (N = 30).

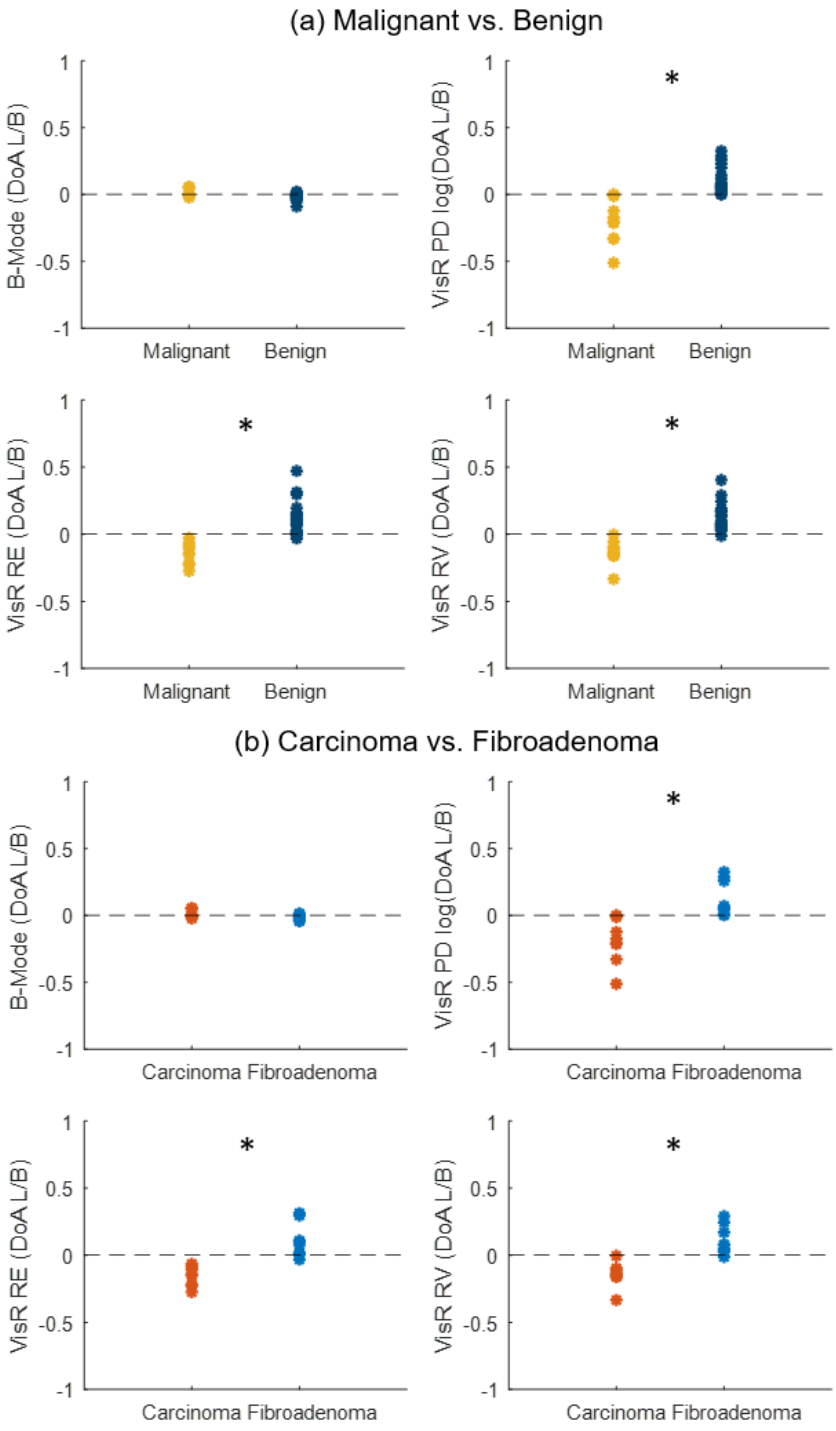

Figure B.6: (a) Malignant vs. benign mass comparison of log(LDoa/SDoA) calculated from B-Mode VisR peak displacement, relative elasticity, and relative viscosity. (b) Carcinoma vs. fibroadenoma mass comparison of log(LDoa/SDoA) calculated from B-Mode VisR peak displacement, relative elasticity, and relative viscosity.

REFERENCES

[1] P. M. Rothwell, M. Eliasziw, S. Gutnikov, A. J. Fox, D. W. Taylor, M. Mayberg, C. P. Warlow, and H. Barnett, "Analysis of pooled data from the randomised controlled trials of endarterectomy for symptomatic carotid stenosis," *The Lancet*, vol. 361, no. 9352, pp. 107–116, 2003.

[2] A. Halliday, M. Harrison, E. Hayter, X. Kong, A. Mansfield, J. Marro, H. Pan, R. Peto, J. Potter, K. Rahimi, *et al.*, "10-year stroke prevention after successful carotid endarterectomy for asymptomatic stenosis (acst-1): a multicentre randomised trial," *The Lancet*, vol. 376, no. 9746, pp. 1074–1084, 2010.

[3] P. R. Moreno, "Vulnerable plaque: definition, diagnosis, and treatment," *Cardiology clinics*, vol. 28, no. 1, pp. 1–30, 2010.

[4] H. C. Stary, A. B. Chandler, R. E. Dinsmore, V. Fuster, S. Glagov, W. Insull Jr, M. E. Rosenfeld, C. J. Schwartz, W. D. Wagner, and R. W. Wissler, "A definition of advanced types of atherosclerotic lesions and a histological classification of atherosclerosis: a report from the committee on vascular lesions of the council on arteriosclerosis, american heart association," *Circulation*, vol. 92, no. 5, pp. 1355–1374, 1995.

[5] C. Pislaru, B. Kantor, R. R. Kinnick, J. L. Anderson, M.-C. Aubry, M. W. Urban, M. Fatemi, and J. F. Greenleaf, "In vivo vibroacoustography of large peripheral arteries," *Investigative radiology*, vol. 43, no. 4, p. 243, 2008.

[6] K. V. Ramnarine, J. W. Garrard, B. Kanber, S. Nduwayo, T. C. Hartshorne, and T. G. Robinson, "Shear wave elastography imaging of carotid plaques: feasible, reproducible and of clinical potential," *Cardiovascular ultrasound*, vol. 12, no. 1, pp. 1–9, 2014.

[7] M. Bernal, M. W. Urban, and J. F. Greenleaf, "Estimation of mechanical properties of arteries and soft tubes using shear wave speeds," in *2009 IEEE International Ultrasonics Symposium*, pp. 177–180, IEEE, 2009.

[8] T. J. Czernuszewicz, J. W. Homeister, M. C. Caughey, Y. Wang, H. Zhu, B. Y. Huang, E. R. Lee, C. A. Zamora, M. A. Farber, J. J. Fulton, *et al.*, "Performance of acoustic radiation force impulse ultrasound imaging for carotid plaque characterization with histologic validation," *Journal of vascular surgery*, vol. 66, no. 6, pp. 1749–1757, 2017.

[9] E. J. Benjamin, P. Muntner, A. Alonso, M. S. Bittencourt, C. W. Callaway, A. P. Carson, A. M. Chamberlain, A. R. Chang, S. Cheng, S. R. Das, *et al.*, "Heart disease and stroke statistics-2019 update: a report from the american heart association," *Circulation*, vol. 139, no. 10, pp. e56–e528, 2019.

[10] S. Keyhani, E. Madden, E. M. Cheng, D. M. Bravata, E. Halm, P. C. Austin, M. Ghasemiesfe, A. S. Abraham, A. J. Zhang, and J. M. Johanning, "Risk prediction tools to improve patient selection for carotid endarterectomy among patients with asymptomatic carotid stenosis," *JAMA surgery*, vol. 154, no. 4, pp. 336–344, 2019.

[11] R. Virmani, F. D. Kolodgie, A. P. Burke, A. Farb, and S. M. Schwartz, "Lessons from sudden coronary death: a comprehensive morphological classification scheme for atherosclerotic lesions," *Arteriosclerosis, thrombosis, and vascular biology*, vol. 20, no. 5, pp. 1262–1275, 2000.

[12] J. N. Redgrave, P. Gallagher, J. K. Lovett, and P. M. Rothwell, "Critical cap thickness and rupture in symptomatic carotid plaques: the oxford plaque study," *Stroke*, vol. 39, no. 6, pp. 1722–1729, 2008.

[13] A. Gupta, H. Baradaran, A. D. Schweitzer, H. Kamel, A. Pandya, D. Delgado, A. Dunning, A. I. Mushlin, and P. C. Sanelli, "Carotid plaque mri and stroke risk: a systematic review and meta-analysis," *Stroke*, vol. 44, no. 11, pp. 3071–3077, 2013.

[14] A. Gupta, H. Baradaran, H. Kamel, A. Mangla, A. Pandya, V. Fodera, A. Dunning, and P. Sanelli, "Intraplaque high-intensity signal on 3d time-of-flight mr angiography is strongly associated with symptomatic carotid artery stenosis," *American Journal of Neuroradiology*, vol. 35, no. 3, pp. 557–561, 2014.

[15] M. Kassem, A. Florea, F. M. Mottaghy, R. van Oostenbrugge, and M. E. Kooi, "Magnetic resonance imaging of carotid plaques: current status and clinical perspectives," *Annals of Translational Medicine*, vol. 8, no. 19, 2020.

[16] A. Gupta and R. S. Marshall, "Moving beyond luminal stenosis: imaging strategies for stroke prevention in asymptomatic carotid stenosis," *Cerebrovascular Diseases*, vol. 39, no. 5-6, pp. 253–261, 2015.

[17] C. Caussin, A. Ohanessian, S. Ghostine, L. Jacq, B. Lancelin, G. Dambrin, A. Sigal-Cinqualbre, C.-Y. Angel, and J.-F. Paul, "Characterization of vulnerable nonstenotic plaque with 16-slice computed tomography compared with intravascular ultrasound," *The American journal of cardiology*, vol. 94, no. 1, pp. 99–104, 2004.

[18] M. Wintermark, S. S. Jawadi, J. H. Rapp, T. Tihan, E. Tong, D. Glidden, S. Abedin, S. Schaeffer, G. Acevedo-Bolton, B. Boudignon, *et al.*, "High-resolution ct imaging of carotid artery atherosclerotic plaques," *American Journal of Neuroradiology*, vol. 29, no. 5, pp. 875–882, 2008.

[19] J. Chen, A. J. Einstein, R. Fazel, H. M. Krumholz, Y. Wang, J. S. Ross, H. H. Ting, N. D. Shah, K. Nasir, and B. K. Nallamothu, "Cumulative exposure to ionizing radiation from diagnostic and therapeutic cardiac imaging procedures: a population-based analysis," *Journal of the American College of Cardiology*, vol. 56, no. 9, pp. 702–711, 2010.

[20] D. Kardoulas, A. Katsamouris, P. T. Gallis, T. P. Philippides, N. Anagnostakos, D. Gorgoyannis, and N. Gourtsoyannis, "Ultrasonographic and histologic characteristics of symptom-free and symptomatic carotid plaque," *Cardiovascular surgery*, vol. 4, no. 5, pp. 580–590, 1996.

[21] L. Gerrit, E. J. Sijbrands, D. Staub, B. Coll, J. Folkert, S. B. Feinstein, and A. F. Schinkel, "Noninvasive imaging of the vulnerable atherosclerotic plaque," *Current problems in cardiology*, vol. 35, no. 11, pp. 556–591, 2010.

[22] A. Nair, B. D. Kuban, E. M. Tuzcu, P. Schoenhagen, S. E. Nissen, and D. G. Vince, "Coronary plaque classification with intravascular ultrasound radiofrequency data analysis," *Circulation*, vol. 106, no. 17, pp. 2200–2206, 2002.

[23] M. Chiocchi, A. Chiaravalloti, D. Morosetti, G. Loreni, R. Gandini, S. Mancino, S. Fabiano, and G. Simonetti, "Virtual histology-intravascular ultrasound as a diagnostic alternative for morphological characterization of carotid plaque: comparison with histology and high-resolution magnetic resonance findings," *Journal of Cardiovascular Medicine*, vol. 20, no. 5, pp. 335–342, 2019.

[24] X. Wu, A. Maehara, G. S. Mintz, T. Kubo, K. Xu, S.-Y. Choi, Y. He, N. Guo, J. W. Moses, M. B. Leon, *et al.*, "Virtual histology intravascular ultrasound analysis of non-culprit attenuated plaques detected by grayscale intravascular ultrasound in patients with acute coronary syndromes," *The American journal of cardiology*, vol. 105, no. 1, pp. 48–53, 2010.

[25] J. J. Rico-Jimenez, D. U. Campos-Delgado, M. Villiger, K. Otsuka, B. E. Bouma, and J. A. Jo, "Automatic classification of atherosclerotic plaques imaged with intravascular oct," *Biomedical optics express*, vol. 7, no. 10, pp. 4069–4085, 2016.

[26] S. Partovi, B. B. Ghoshhajra, and T. G. Walker, "Beyond stenotic degree assessment in carotid atherosclerotic lesions: single catheter near-infrared spectroscopy and intravascular ultrasound," *The international journal of cardiovascular imaging*, vol. 32, no. 1, pp. 201–203, 2016.

[27] Z. Xie, C. Shu, X. Gong, and L. Song, "Carotid atherosclerosis detection using photoacoustic imaging system," in *Optics in Health Care and Biomedical Optics IX*, vol. 11190, p. 111902T, International Society for Optics and Photonics, 2019.

[28] P. Libby, P. M. Ridker, and G. K. Hansson, "Progress and challenges in translating the biology of atherosclerosis," *Nature*, vol. 473, no. 7347, pp. 317–325, 2011.

[29] K. Theodorou and R. A. Boon, "Endothelial cell metabolism in atherosclerosis," *Frontiers in Cell and Developmental Biology*, vol. 6, p. 82, 2018.

[30] L. M. Buja, T. Kita, J. L. Goldstein, Y. Watanabe, and M. S. Brown, "Cellular pathology of progressive atherosclerosis in the whhl rabbit. an animal model of familial hypercholesterolemia.," *Arteriosclerosis: An Official Journal of the American Heart Association, Inc.*, vol. 3, no. 1, pp. 87–101, 1983.

[31] H. C. Stary, A. B. Chandler, S. Glagov, J. R. Guyton, W. Insull Jr, M. E. Rosenfeld, S. A. Schaffer, C. J. Schwartz, W. D. Wagner, and R. W. Wissler, "A definition of initial, fatty streak, and intermediate lesions of atherosclerosis. a report from the committee on vascular lesions of the council on arteriosclerosis, american heart association.," *Circulation*, vol. 89, no. 5, pp. 2462–2478, 1994.

[32] G. Helft, S. G. Worthley, V. Fuster, Z. A. Fayad, A. G. Zaman, R. Corti, J. T. Fallon, and J. J. Badimon, "Progression and regression of atherosclerotic lesions: monitoring with serial noninvasive magnetic resonance imaging," *Circulation*, vol. 105, no. 8, pp. 993–998, 2002.

[33] H. C. Stary, "Natural history and histological classification of atherosclerotic lesions: an update," *Arteriosclerosis, thrombosis, and vascular biology*, vol. 20, no. 5, pp. 1177–1178, 2000.

[34] A. V. Finn, M. Nakano, J. Narula, F. D. Kolodgie, and R. Virmani, "Concept of vulnerable/unstable plaque," *Arteriosclerosis, thrombosis, and vascular biology*, vol. 30, no. 7, pp. 1282–1292, 2010.

[35] A. P. Burke, A. Farb, G. T. Malcom, Y.-h. Liang, J. Smialek, and R. Virmani, "Coronary risk factors and plaque morphology in men with coronary disease who died suddenly," *New England Journal of Medicine*, vol. 336, no. 18, pp. 1276–1282, 1997.

[36] H. M. Loree, R. Kamm, R. Stringfellow, and R. T. Lee, "Effects of fibrous cap thickness on peak circumferential stress in model atherosclerotic vessels.," *Circulation research*, vol. 71, no. 4, pp. 850–858, 1992.

[37] Z.-Y. Li, S. P. Howarth, T. Tang, and J. H. Gillard, "How critical is fibrous cap thickness to carotid plaque stability? a flow–plaque interaction model," *Stroke*, vol. 37, no. 5, pp. 1195–1199, 2006.

[38] P. K. Shah, E. Falk, J. J. Badimon, A. Fernandez-Ortiz, A. Mailhac, G. Villareal-Levy, J. T. Fallon, J. Regnstrom, and V. Fuster, "Human monocyte-derived macrophages induce collagen breakdown in fibrous caps of atherosclerotic plaques. potential role of matrix-degrading metalloproteinases and implications for plaque rupture.," *Circulation*, vol. 92, no. 6, pp. 1565–1569, 1995.

[39] W. Olejarz, D. Łacheta, and G. Kubiak-Tomaszewska, "Matrix metalloproteinases as biomarkers of atherosclerotic plaque instability," *International Journal of Molecular Sciences*, vol. 21, no. 11, p. 3946, 2020.

[40] L. Cardoso and S. Weinbaum, "Changing views of the biomechanics of vulnerable plaque rupture: a review," *Annals of biomedical engineering*, vol. 42, no. 2, pp. 415–431, 2014.

[41] A. Fernández-Ortiz, J. J. Badimon, E. Falk, V. Fuster, B. Meyer, A. Mailhac, D. Weng, P. K. Shah, and L. Badimon, "Characterization of the relative thrombogenicity of atherosclerotic plaque components: implications for consequences of plaque rupture," *Journal of the American College of Cardiology*, vol. 23, no. 7, pp. 1562–1569, 1994.

[42] R. Virmani, A. P. Burke, A. Farb, and F. D. Kolodgie, "Pathology of the vulnerable plaque," *Journal of the American College of Cardiology*, vol. 47, no. 8S, pp. C13–C18, 2006.

[43] J. Xia, A. Yin, Z. Li, X. Liu, X. Peng, and N. Xie, "Quantitative analysis of lipid-rich necrotic core in carotid atherosclerotic plaques by in vivo magnetic resonance imaging and clinical outcomes," *Medical science monitor: international medical journal of experimental and clinical research*, vol. 23, p. 2745, 2017.

[44] J. Ohayon, G. Finet, A. M. Gharib, D. A. Herzka, P. Tracqui, J. Heroux, G. Rioufol, M. S. Kotys, A. Elagha, and R. I. Pettigrew, "Necrotic core thickness and positive arterial remodeling index: emergent biomechanical factors for evaluating the risk of plaque rupture," *American journal of physiology-heart and circulatory physiology*, vol. 295, no. 2, pp. H717–H727, 2008.

[45] P. R. Moreno, K.-R. Purushothaman, E. Zias, J. Sanz, and V. Fuster, "Neovascularization in human atherosclerosis," *Current molecular medicine*, vol. 6, no. 5, pp. 457–477, 2006.

[46] F. Demeure, C. Bouzin, V. Roelants, A. Bol, R. Verhelst, P. Astarci, B. L. Gerber, A.-C. Pouleur, A. Pasquet, C. de Meester, *et al.*, "Head-to-head comparison of inflammation and neovascularization in human carotid plaques: implications for the imaging of vulnerable plaques," *Circulation: Cardiovascular Imaging*, vol. 10, no. 5, p. e005846, 2017.

[47] L. Parma, F. Baganha, P. H. Quax, and M. R. de Vries, "Plaque angiogenesis and intraplaque hemorrhage in atherosclerosis," *European journal of pharmacology*, vol. 816, pp. 107–115, 2017.

[48] J.-B. Michel and J. L. Martin-Ventura, "Red blood cells and hemoglobin in human atherosclerosis and related arterial diseases," *International Journal of Molecular Sciences*, vol. 21, no. 18, p. 6756, 2020.

[49] T. Thim, M. Hagensen, J. Bentzon, and E. Falk, "From vulnerable plaque to atherothrombosis," *Journal of internal medicine*, vol. 263, no. 5, pp. 506–516, 2008.

[50] J. T. Pruijssen, C. L. de Korte, I. Voss, and H. H. Hansen, "Vascular shear wave elastography in atherosclerotic arteries: A systematic review," *Ultrasound in Medicine & Biology*, 2020.

[51] R. A. Trivedi, U. Jean-Marie, M. J. Graves, J. Horsley, M. Goddard, P. J. Kirkpatrick, J. H. Gillard, *et al.*, "Mri-derived measurements of fibrous-cap and lipid-core thickness: the potential for identifying vulnerable carotid plaques in vivo," *Neuroradiology*, vol. 46, no. 9, pp. 738–743, 2004.

[52] J. Morrisett, W. Vick, R. Sharma, G. Lawrie, M. Reardon, E. Ezell, J. Schwartz, G. Hunter, and D. Gorenstein, "Discrimination of components in atherosclerotic plaques from human carotid endarterectomy specimens by magnetic resonance imaging ex vivo," *Magnetic resonance imaging*, vol. 21, no. 5, pp. 465–474, 2003.

[53] K. Murata, N. Murata, B. Chu, H. Watase, D. S. Hippe, N. Balu, J. Sun, X. Zhao, T. S. Hatsukami, C. Yuan, *et al.*, "Characterization of carotid atherosclerotic plaques using 3-dimensional merge magnetic resonance imaging and correlation with stroke risk factors," *Stroke*, vol. 51, no. 2, pp. 475–480, 2020.

[54] A. Nair, M. P. Margolis, B. D. Kuban, and D. G. Vince, "Automated coronary plaque characterisation with intravascular ultrasound backscatter: ex vivo validation.," *EuroIntervention: journal of EuroPCR in collaboration with the Working Group on Interventional Cardiology of the European Society of Cardiology*, vol. 3, no. 1, pp. 113–120, 2007.

[55] H. M. Garcia-Garcia, I.-K. Jang, P. W. Serruys, J. C. Kovacic, J. Narula, and Z. A. Fayad, "Imaging plaques to predict and better manage patients with acute coronary events," *Circulation research*, vol. 114, no. 12, pp. 1904–1917, 2014.

[56] C. Schmitt, G. Soulez, R. L. Maurice, M.-F. Giroux, and G. Cloutier, "Noninvasive vascular elastography: toward a complementary characterization tool of atherosclerosis in carotid arteries," *Ultrasound in medicine & biology*, vol. 33, no. 12, pp. 1841–1858, 2007.

[57] M.-H. R. Cardinal, M. Durand, C. Chartrand-Lefebvre, C. Fortin, J.-G. Baril, B. Trottier, J.-P. Routy, G. Soulez, C. Tremblay, and G. Cloutier, "Increased carotid artery wall stiffness and plaque prevalence in hiv infected patients measured with ultrasound elastography," *European radiology*, pp. 1–10, 2020.

[58] R. El Jalbout, G. Cloutier, M.-H. Roy-Cardinal, M. Henderson, E. Levy, C. Lapierre, G. Soulez, and J. Dubois, "The value of non-invasive vascular elastography (nive) in detecting early vascular changes in overweight and obese children," *European radiology*, vol. 29, no. 7, pp. 3854–3861, 2019.

[59] M.-H. Roy Cardinal, M. H. Heusinkveld, Z. Qin, R. G. Lopata, C. Naim, G. Soulez, and G. Cloutier, "Carotid artery plaque vulnerability assessment using noninvasive ultrasound elastography: validation with mri," *American journal of Roentgenology*, vol. 209, no. 1, pp. 142–151, 2017.

[60] R. X. Li, I. Z. Apostolakis, P. Kemper, M. D. McGarry, A. Ip, E. S. Connolly, J. F. McKinsey, and E. E. Konofagou, "Pulse wave imaging in carotid artery stenosis human patients in vivo," *Ultrasound in medicine & biology*, vol. 45, no. 2, pp. 353–366, 2019.

[61] J. Shang, W. Wang, J. Feng, G.-g. Luo, Y. Dang, J. Sun, Y.-q. Yang, and L.-t. Ruan, "Carotid plaque stiffness measured with supersonic shear imaging and its correlation with

serum homocysteine level in ischemic stroke patients," *Korean journal of radiology*, vol. 19, no. 1, p. 15, 2018.

[62] A. Sarvazyan, A. Skovoroda, S. Emelianov, J. Fowlkes, J. Pipe, R. Adler, R. Buxton, and P. Carson, "Biophysical bases of elasticity imaging," in *Acoustical imaging*, pp. 223–240, Springer, 1995.

[63] L. Rayleigh, "Xxxiv. on the pressure of vibrations," *The London, Edinburgh, and Dublin Philosophical Magazine and Journal of Science*, vol. 3, no. 15, pp. 338–346, 1902.

[64] T. Sugimoto, S. Ueha, and K. Itoh, "Tissue hardness measurement using the radiation force of focused ultrasound," in *IEEE Symposium on Ultrasonics*, pp. 1377–1380, IEEE, 1990.

[65] M. L. Palmeri, A. C. Sharma, R. R. Bouchard, R. W. Nightingale, and K. R. Nightingale, "A finite-element method model of soft tissue response to impulsive acoustic radiation force," *IEEE transactions on ultrasonics, ferroelectrics, and frequency control*, vol. 52, no. 10, pp. 1699–1712, 2005.

[66] E. V. Dontsov and B. B. Guzina, "Acoustic radiation force in tissue-like solids due to modulated sound field," *Journal of the Mechanics and Physics of Solids*, vol. 60, no. 10, pp. 1791–1813, 2012.

[67] B. B. Guzina, E. V. Dontsov, M. W. Urban, and M. Fatemi, "The sixth sense of ultrasound: probing nonlinear elasticity with acoustic radiation force," *Physics in Medicine & Biology*, vol. 60, no. 9, p. 3775, 2015.

[68] M. L. Palmeri and K. R. Nightingale, "On the thermal effects associated with radiation force imaging of soft tissue," *IEEE transactions on ultrasonics, ferroelectrics, and frequency control*, vol. 51, no. 5, pp. 551–565, 2004.

[69] M. L. Palmeri, K. D. Frinkley, and K. R. Nightingale, "Experimental studies of the thermal effects associated with radiation force imaging of soft tissue," *Ultrasonic Imaging*, vol. 26, no. 2, pp. 100–114, 2004.

[70] K. Nightingale, M. S. Soo, R. Nightingale, and G. Trahey, "Acoustic radiation force impulse imaging: in vivo demonstration of clinical feasibility," *Ultrasound in medicine & biology*, vol. 28, no. 2, pp. 227–235, 2002.

[71] M. Fatemi and J. F. Greenleaf, "Ultrasound-stimulated vibro-acoustic spectrography," *Science*, vol. 280, no. 5360, pp. 82–85, 1998.

[72] M. Fatemi and J. F. Greenleaf, "Vibro-acoustography: An imaging modality based on ultrasound-stimulated acoustic emission," *Proceedings of the National Academy of Sciences*, vol. 96, no. 12, pp. 6603–6608, 1999.

[73] A. Alizad, M. Fatemi, L. E. Wold, and J. F. Greenleaf, "Performance of vibro-acoustography in detecting microcalcifications in excised human breast tissue: A study of 74 tissue samples," *IEEE transactions on medical imaging*, vol. 23, no. 3, pp. 307–312, 2004.

[74] M. W. Urban, C. Chalek, R. R. Kinnick, T. M. Kinter, B. Haider, J. F. Greenleaf, K. E. Thomenius, and M. Fatemi, "Implementation of vibro-acoustography on a clinical ultrasound system," *IEEE transactions on ultrasonics, ferroelectrics, and frequency control*, vol. 58, no. 6, pp. 1169–1181, 2011.

[75] M. W Urban, A. Alizad, W. Aquino, J. F Greenleaf, and M. Fatemi, "A review of vibro-acoustography and its applications in medicine," *Current Medical Imaging*, vol. 7, no. 4, pp. 350–359, 2011.

[76] A. P. Sarvazyan, O. V. Rudenko, S. D. Swanson, J. B. Fowlkes, and S. Y. Emelianov, "Shear wave elasticity imaging: a new ultrasonic technology of medical diagnostics," *Ultrasound in medicine & biology*, vol. 24, no. 9, pp. 1419–1435, 1998.

[77] K. Nightingale, S. McAleavey, and G. Trahey, "Shear-wave generation using acoustic radiation force: in vivo and ex vivo results," *Ultrasound in medicine & biology*, vol. 29, no. 12, pp. 1715–1723, 2003.

[78] M. L. Palmeri, M. H. Wang, N. C. Rouze, M. F. Abdelmalek, C. D. Guy, B. Moser, A. M. Diehl, and K. R. Nightingale, "Noninvasive evaluation of hepatic fibrosis using acoustic radiation force-based shear stiffness in patients with nonalcoholic fatty liver disease," *Journal of hepatology*, vol. 55, no. 3, pp. 666–672, 2011.

[79] A. Giannoula and R. S. Cobbold, "Narrowband shear wave generation by a finite-amplitude radiation force: The fundamental component," *IEEE transactions on ultrasonics, ferroelectrics, and frequency control*, vol. 55, no. 2, pp. 343–358, 2008.

[80] S. A. McAleavey, M. Menon, and J. Orszulak, "Shear-modulus estimation by application of spatially-modulated impulsive acoustic radiation force," *Ultrasonic imaging*, vol. 29, no. 2, pp. 87–104, 2007.

[81] D. Marlevi, S. L. Mulvagh, R. Huang, J. K. DeMarco, H. Ota, J. Huston, R. Winter, T. A. Macedo, S. S. Abdelmoneim, M. Larsson, *et al.*, "Combined spatiotemporal and frequency-dependent shear wave elastography enables detection of vulnerable carotid plaques as validated by mri," *Scientific reports*, vol. 10, no. 1, pp. 1–13, 2020.

[82] Z. Lei, Y. Qiang, P. Tianning, and L. Jie, "Quantitative assessment of carotid atherosclerotic plaque: Initial clinical results using shearwave elastography," *Int J Clin Exp Med*, vol. 9, no. 6, pp. 9347–9355, 2016.

[83] Z. Lou, J. Yang, L. Tang, Y. Jin, J. Zhang, C. Liu, and Q. Li, "Shear wave elastography imaging for the features of symptomatic carotid plaques: a feasibility study," *Journal of Ultrasound in Medicine*, vol. 36, no. 6, pp. 1213–1223, 2017.

[84] B. Kanber, T. C. Hartshorne, M. A. Horsfield, A. R. Naylor, T. G. Robinson, and K. V. Ramnarine, "Dynamic variations in the ultrasound greyscale median of carotid artery plaques," *Cardiovascular ultrasound*, vol. 11, no. 1, pp. 1–12, 2013.

[85] Q. He, G.-Y. Li, F.-F. Lee, Q. Zhang, Y. Cao, and J. Luo, "Novel method for vessel cross-sectional shear wave imaging," *Ultrasound in medicine & biology*, vol. 43, no. 7, pp. 1520–1532, 2017.

[86] M. W Urban, S. Chen, and M. Fatemi, "A review of shearwave dispersion ultrasound vibrometry (sduv) and its applications," *Current Medical Imaging*, vol. 8, no. 1, pp. 27–36, 2012.

[87] I. Z. Nenadic, M. W. Urban, S. A. Mitchell, and J. F. Greenleaf, "Lamb wave dispersion ultrasound vibrometry (lduv) method for quantifying mechanical properties of viscoelastic solids," *Physics in Medicine & Biology*, vol. 56, no. 7, p. 2245, 2011.

[88] S. Chen, M. W. Urban, C. Pislaru, R. Kinnick, Y. Zheng, A. Yao, and J. F. Greenleaf, "Shearwave dispersion ultrasound vibrometry (sduv) for measuring tissue elasticity and viscosity," *IEEE transactions on ultrasonics, ferroelectrics, and frequency control*, vol. 56, no. 1, pp. 55–62, 2009.

[89] X. Zhang, R. R. Kinnick, M. Fatemi, and J. F. Greenleaf, "Noninvasive method for estimation of complex elastic modulus of arterial vessels," *IEEE transactions on ultrasonics, ferroelectrics, and frequency control*, vol. 52, no. 4, pp. 642–652, 2005.

[90] J. R. Doherty, J. J. Dahl, P. G. Kranz, N. El Husseini, H.-C. Chang, N.-k. Chen, J. D. Allen, K. L. Ham, and G. E. Trahey, "Comparison of acoustic radiation force impulse imaging derived carotid plaque stiffness with spatially registered mri determined composition," *IEEE transactions on medical imaging*, vol. 34, no. 11, pp. 2354–2365, 2015.

[91] G. F. Pinton, J. J. Dahl, and G. E. Trahey, "Rapid tracking of small displacements with ultrasound," *IEEE transactions on ultrasonics, ferroelectrics, and frequency control*, vol. 53, no. 6, pp. 1103–1117, 2006.

[92] T. Loupas, R. Peterson, and R. W. Gill, "Experimental evaluation of velocity and power estimation for ultrasound blood flow imaging, by means of a two-dimensional autocorrelation approach," *IEEE transactions on ultrasonics, ferroelectrics, and frequency control*, vol. 42, no. 4, pp. 689–699, 1995.

[93] C. Kasai, K. Namekawa, A. Koyano, and R. Omoto, "Real-time two-dimensional blood flow imaging using an autocorrelation technique," *IEEE Transactions on sonics and ultrasonics*, vol. 32, no. 3, pp. 458–464, 1985.

[94] B. Byram, G. E. Trahey, and M. Palmeri, "Bayesian speckle tracking. part ii: biased ultrasound displacement estimation," *IEEE transactions on ultrasonics, ferroelectrics, and frequency control*, vol. 60, no. 1, pp. 144–157, 2012.

[95] G. E. Trahey, M. L. Palmeri, R. C. Bentley, and K. R. Nightingale, "Acoustic radiation force impulse imaging of the mechanical properties of arteries: in vivo and ex vivo results," *Ultrasound in medicine & biology*, vol. 30, no. 9, pp. 1163–1171, 2004.

[96] D. Dumont, R. H. Behler, T. C. Nichols, E. P. Merricks, and C. M. Gallippi, "Arfi imaging for noninvasive material characterization of atherosclerosis," *Ultrasound in medicine & biology*, vol. 32, no. 11, pp. 1703–1711, 2006.

[97] R. H. Behler, T. C. Nichols, H. Zhu, E. P. Merricks, and C. M. Gallippi, "Arfi imaging for noninvasive material characterization of atherosclerosis part ii: toward in vivo characterization," *Ultrasound in medicine & biology*, vol. 35, no. 2, pp. 278–295, 2009.

[98] R. H. Behler, T. J. Czernuszewicz, T. C. Nichols, H. Zhu, J. W. Homeister, E. P. Merricks, C. M. Gallippi, *et al.*, "Acoustic radiation force beam sequence performance for detection and material characterization of atherosclerotic plaques: preclinical, ex vivo results," *IEEE transactions on ultrasonics, ferroelectrics, and frequency control*, vol. 60, no. 12, pp. 2471–2487, 2013.

[99] J. J. Dahl, D. M. Dumont, J. D. Allen, E. M. Miller, and G. E. Trahey, "Acoustic radiation force impulse imaging for noninvasive characterization of carotid artery atherosclerotic plaques: a feasibility study," *Ultrasound in medicine & biology*, vol. 35, no. 5, pp. 707–716, 2009.

[100] T. J. Czernuszewicz, J. W. Homeister, M. C. Caughey, M. A. Farber, J. J. Fulton, P. F. Ford, W. A. Marston, R. Vallabhaneni, T. C. Nichols, and C. M. Gallippi, "Non-invasive in vivo characterization of human carotid plaques with acoustic radiation force impulse ultrasound: comparison with histology after endarterectomy," *Ultrasound in medicine & biology*, vol. 41, no. 3, pp. 685–697, 2015.

[101] A. Gupta, H. Baradaran, and A. Schweitzer, "Carotid plaque mri and stroke risk: A systematic review and meta-analysis," *Journal of Vascular Surgery*, vol. 59, no. 4, p. 1175, 2014.

[102] W. F. Walker and G. E. Trahey, "A fundamental limit on delay estimation using partially correlated speckle signals," *IEEE transactions on ultrasonics, ferroelectrics, and frequency control*, vol. 42, no. 2, pp. 301–308, 1995.

[103] S. Lloyd, "Least squares quantization in pcm," *IEEE transactions on information theory*, vol. 28, no. 2, pp. 129–137, 1982.

[104] G. C. Cheng, H. M. Loree, R. D. Kamm, M. C. Fishbein, and R. T. Lee, "Distribution of circumferential stress in ruptured and stable atherosclerotic lesions. a structural analysis with histopathological correlation.," *Circulation*, vol. 87, no. 4, pp. 1179–1187, 1993.

[105] Z.-Y. Li, S. Howarth, R. A. Trivedi, J. M. U-King-Im, M. J. Graves, A. Brown, L. Wang, and J. H. Gillard, "Stress analysis of carotid plaque rupture based on in vivo high resolution mri," *Journal of biomechanics*, vol. 39, no. 14, pp. 2611–2622, 2006.

[106] J. R. Doherty, D. M. Dumont, G. E. Trahey, and M. L. Palmeri, "Acoustic radiation force impulse imaging of vulnerable plaques: a finite element method parametric analysis," *Journal of biomechanics*, vol. 46, no. 1, pp. 83–90, 2013.

[107] H. H. Hansen, G. J. de Borst, M. L. Bots, F. L. Moll, G. Pasterkamp, and C. L. de Korte, "Compound ultrasound strain imaging for noninvasive detection of (fibro) atheromatous plaques: Histopathological validation in human carotid arteries," *JACC: Cardiovascular Imaging*, vol. 9, no. 12, pp. 1466–1467, 2016.

[108] H. H. Hansen, G. J. de Borst, M. L. Bots, F. L. Moll, G. Pasterkamp, and C. L. de Korte, "Validation of noninvasive in vivo compound ultrasound strain imaging using histologic plaque vulnerability features," *Stroke*, vol. 47, no. 11, pp. 2770–2775, 2016.

[109] T. J. Czernuszewicz, J. E. Streeter, P. A. Dayton, and C. M. Gallippi, "Experimental validation of displacement underestimation in arfi ultrasound," *Ultrasonic imaging*, vol. 35, no. 3, pp. 196–213, 2013.

[110] T. J. Czernuszewicz and C. M. Gallippi, "On the feasibility of quantifying fibrous cap thickness with acoustic radiation force impulse (arfi) ultrasound," *IEEE transactions on ultrasonics, ferroelectrics, and frequency control*, vol. 63, no. 9, pp. 1262–1275, 2016.

[111] G. Torres, T. J. Czernuszewicz, J. W. Homeister, M. C. Caughey, B. Y. Huang, E. R. Lee, C. A. Zamora, M. A. Farber, W. A. Marston, D. Y. Huang, *et al.*, "Delineation of human carotid plaque features in vivo by exploiting displacement variance," *IEEE transactions on ultrasonics, ferroelectrics, and frequency control*, vol. 66, no. 3, pp. 481–492, 2019.

[112] L. Lin and L. D. Torbeck, "Coefficient of accuracy and concordance correlation coefficient: new statistics for methods comparison," *PDA Journal of Pharmaceutical Science and Technology*, vol. 52, no. 2, pp. 55–59, 1998.

[113] M. L. Palmeri, S. A. McAleavey, G. E. Trahey, and K. R. Nightingale, "Ultrasonic tracking of acoustic radiation force-induced displacements in homogeneous media," *IEEE transactions on ultrasonics, ferroelectrics, and frequency control*, vol. 53, no. 7, pp. 1300–1313, 2006.

[114] J. T. Salonen and R. Salonen, "Ultrasound b-mode imaging in observational studies of atherosclerotic progression.," *Circulation*, vol. 87, no. 3 Suppl, pp. II56–65, 1993.

[115] A. A. Khan, J. C. Hecker, T. Hatsukami, S. Sikdar, and B. K. Lal, "Carotid plaque strain characterization in clinical b-mode ultrasound image sequences," *Journal of Vascular Surgery*, vol. 64, no. 3, pp. 846–847, 2016.

[116] L. Urbak, B. V. Sandholt, M. Graebe, L. E. Bang, H. Bundgaard, and H. Sillesen, "Patients with unstable atherosclerosis have more echolucent carotid plaques compared with stable atherosclerotic patients: A 3-d ultrasound study," *Ultrasound in Medicine & Biology*, vol. 46, no. 9, pp. 2164–2172, 2020.

[117] M.-H. Roy-Cardinal, F. Destrempes, G. Soulez, and G. Cloutier, "Assessment of carotid artery plaque components with machine learning classification using homodyned-k parametric maps and elastograms," *IEEE transactions on ultrasonics, ferroelectrics, and frequency control*, vol. 66, no. 3, pp. 493–504, 2018.

[118] C. L. de Korte, S. Fekkes, A. J. Nederveen, R. Manniesing, and H. R. H. Hansen, "Mechanical characterization of carotid arteries and atherosclerotic plaques," *IEEE transactions on ultrasonics, ferroelectrics, and frequency control*, vol. 63, no. 10, pp. 1613–1623, 2016.

[119] L. J. Brattain, B. A. Telfer, M. Dhyani, J. R. Grajo, and A. E. Samir, "Machine learning for medical ultrasound: status, methods, and future opportunities," *Abdominal radiology*, vol. 43, no. 4, pp. 786–799, 2018.

[120] M. E. Olszewski, A. Wahle, S. C. Mitchell, and M. Sonka, "Segmentation of intravascular ultrasound images: a machine learning approach mimicking human vision," in *International congress series*, vol. 1268, pp. 1045–1049, Elsevier, 2004.

[121] Y. Xu, Y. Wang, J. Yuan, Q. Cheng, X. Wang, and P. L. Carson, "Medical breast ultrasound image segmentation by machine learning," *Ultrasonics*, vol. 91, pp. 1–9, 2019.

[122] S. Latha, D. Samiappan, and R. Kumar, "Carotid artery ultrasound image analysis: A review of the literature," *Proceedings of the institution of mechanical engineers, Part H: journal of engineering in medicine*, vol. 234, no. 5, pp. 417–443, 2020.

[123] R.-M. Menchón-Lara, J.-L. Sancho-Gómez, and A. Bueno-Crespo, "Early-stage atherosclerosis detection using deep learning over carotid ultrasound images," *Applied Soft Computing*, vol. 49, pp. 616–628, 2016.

[124] A. M. Sharma, A. Gupta, P. K. Kumar, J. Rajan, L. Saba, I. Nobutaka, J. R. Laird, A. Nicolades, and J. S. Suri, "A review on carotid ultrasound atherosclerotic tissue characterization and stroke risk stratification in machine learning framework," *Current atherosclerosis reports*, vol. 17, no. 9, pp. 1–13, 2015.

[125] M.-H. Roy-Cardinal, F. Destrempes, G. Soulez, and G. Cloutier, "Homodyned k-distribution parametric maps combined with elastograms for carotid artery plaque assessment," in *2016 IEEE International Ultrasonics Symposium (IUS)*, pp. 1–4, IEEE, 2016.

[126] P. K. Shah, "Mechanisms of plaque vulnerability and rupture," *Journal of the American college of cardiology*, vol. 41, no. 4S, pp. S15–S22, 2003.

[127] M. A. Lediju, M. J. Pihl, J. J. Dahl, and G. E. Trahey, "Quantitative assessment of the magnitude, impact and spatial extent of ultrasonic clutter," *Ultrasonic imaging*, vol. 30, no. 3, pp. 151–168, 2008.

[128] G. Torres, T. J. Czemuszewicz, J. W. Homeister, M. A. Farber, and C. M. Gallippi, "A machine learning approach to delineating carotid atherosclerotic plaque structure and composition by arfi ultrasound, in vivo," in *2018 IEEE International Ultrasonics Symposium (IUS)*, pp. 1–4, IEEE, 2018.

[129] E. B. Cole, Z. Zhang, H. S. Marques, R. M. Nishikawa, R. E. Hendrick, M. J. Yaffe, W. Padungchaichote, C. Kuzmiak, J. Chayakulkheeree, E. F. Conant, *et al.*, "Assessing the stand-alone sensitivity of computer-aided detection with cancer cases from the digital mammographic imaging screening trial," *American Journal of Roentgenology*, vol. 199, no. 3, pp. W392–W401, 2012.

[130] C. M. Kuzmiak, "Breast cancer survivors: Does the screening mri debate continue?," *Academic radiology*, vol. 22, no. 11, pp. 1329–1330, 2015.

[131] W. A. Berg, Z. Zhang, D. Lehrer, R. A. Jong, E. D. Pisano, R. G. Barr, M. Böhm-Vélez, M. C. Mahoney, W. P. Evans, L. H. Larsen, *et al.*, "Detection of breast cancer with addition of annual screening ultrasound or a single screening mri to mammography in women with elevated breast cancer risk," *Jama*, vol. 307, no. 13, pp. 1394–1404, 2012.

[132] R. G. Barr and Z. Zhang, "Shear-wave elastography of the breast: value of a quality measure and comparison with strain elastography," *Radiology*, vol. 275, no. 1, pp. 45–53, 2015.

[133] J. R. Grajo and R. G. Barr, "Strain elastography for prediction of breast cancer tumor grades," *Journal of Ultrasound in Medicine*, vol. 33, no. 1, pp. 129–134, 2014.

[134] J. H. Youk, H. M. Gweon, and E. J. Son, "Shear-wave elastography in breast ultrasonography: the state of the art," *Ultrasonography*, vol. 36, no. 4, p. 300, 2017.

[135] E. Giannotti, S. Vinnicombe, K. Thomson, D. McLean, C. Purdie, L. Jordan, and A. Evans, "Shear-wave elastography and greyscale assessment of palpable probably benign masses: is biopsy always required?," *The British journal of radiology*, vol. 89, no. 1062, p. 20150865, 2016.

[136] Y. Qiu, M. Sridhar, J. K. Tsou, K. K. Lindfors, and M. F. Insana, "Ultrasonic viscoelasticity imaging of nonpalpable breast tumors: preliminary results," *Academic radiology*, vol. 15, no. 12, pp. 1526–1533, 2008.

[137] A. Nabavizadeh, M. Bayat, V. Kumar, A. Gregory, J. Webb, A. Alizad, and M. Fatemi, "Viscoelastic biomarker for differentiation of benign and malignant breast lesion in ultra-low frequency range," *Scientific reports*, vol. 9, no. 1, pp. 1–12, 2019.

[138] H. Zhang, Y. Guo, Y. Zhou, H. Zhu, P. Wu, K. Wang, L. Ruan, M. Wan, and M. F. Insana, "Fluidity and elasticity form a concise set of viscoelastic biomarkers for breast cancer diagnosis based on kelvin–voigt fractional derivative modeling," *Biomechanics and modeling in mechanobiology*, vol. 19, no. 6, pp. 2163–2177, 2020.

[139] R. Sood, A. F. Rositch, D. Shakoor, E. Ambinder, K.-L. Pool, E. Pollack, D. J. Mollura, L. A. Mullen, and S. C. Harvey, "Ultrasound for breast cancer detection globally: a systematic review and meta-analysis," *Journal of global oncology*, vol. 5, pp. 1–17, 2019.

[140] M. H. Zahran, M. M. El-Shafei, D. M. Emara, and S. M. Eshiba, "Ultrasound elastography: How can it help in differentiating breast lesions?," *The Egyptian Journal of Radiology and Nuclear Medicine*, vol. 49, no. 1, pp. 249–258, 2018.

[141] Y. You, Y. Song, S. Li, Z. Ma, and H. Bo, "Quantitative and qualitative evaluation of breast cancer prognosis: a sonographic elastography study," *Medical science monitor: international medical journal of experimental and clinical research*, vol. 25, p. 9272, 2019.

[142] R. Sinkus, M. Tanter, S. Catheline, J. Lorenzen, C. Kuhl, E. Sondermann, and M. Fink, "Imaging anisotropic and viscous properties of breast tissue by magnetic resonance-elastography," *Magnetic Resonance in Medicine: An Official Journal of the International Society for Magnetic Resonance in Medicine*, vol. 53, no. 2, pp. 372–387, 2005.

[143] K. Skerl, S. Vinnicombe, K. Thomson, D. McLean, E. Giannotti, and A. Evans, "Anisotropy of solid breast lesions in 2d shear wave elastography is an indicator of malignancy," *Academic radiology*, vol. 23, no. 1, pp. 53–61, 2016.

[144] Y.-l. Chen, Y. Gao, C. Chang, F. Wang, W. Zeng, and J.-j. Chen, "Ultrasound shear wave elastography of breast lesions: correlation of anisotropy with clinical and histopathological findings," *Cancer Imaging*, vol. 18, no. 1, pp. 1–11, 2018.

[145] G. Torres, C. J. Moore, D. Steed, J. Merhout, M. Caughey, S. R. Kirk, T. S. Hartman, C. M. Kuzmiak, and C. M. Gallippi, "Differentiating malignant from benign breast masses in women, in vivo, using visr-assessed mechanical anisotropy," in *2020 IEEE International Ultrasonics Symposium (IUS)*, pp. 1–3, IEEE, 2020.

[146] M. R. Selzo and C. M. Gallippi, "Viscoelastic response (visr) imaging for assessment of viscoelasticity in voigt materials," *IEEE transactions on ultrasonics, ferroelectrics, and frequency control*, vol. 60, no. 12, pp. 2488–2500, 2013.

[147] M. R. Selzo, C. J. Moore, M. M. Hossain, M. L. Palmeri, and C. M. Gallippi, "On the quantitative potential of viscoelastic response (visr) ultrasound using the one-dimensional mass-spring-damper model," *IEEE transactions on ultrasonics, ferroelectrics, and frequency control*, vol. 63, no. 9, pp. 1276–1287, 2016.

[148] M. Hossain, C. Moore, and C. Gallippi, "On the quantitative potential of viscoelastic response (visr) ultrasound using matrix array transducers: In silico demonstration," in *2016 IEEE International Ultrasonics Symposium (IUS)*, pp. 1–4, IEEE, 2016.